Nonequilibrium carrier dynamics in self-assembled quantum dots

Cite as: Appl. Phys. Rev. **6**, 031306 (2019); https://doi.org/10.1063/1.5091742
Submitted: 05 February 2019 . Accepted: 14 August 2019 . Published Online: 25 September 2019

M. Geller

Applied Physics Reviews REVIEW scitation.org/journal/are

Nonequilibrium carrier dynamics in self-assembled quantum dots

Cite as: Appl. Phys. Rev. 6, 031306 (2019); doi: 10.1063/1.5091742
Submitted: 5 February 2019 · Accepted: 14 August 2019 ·
Published Online: 25 September 2019

M. Geller[a)]

AFFILIATIONS

Faculty of Physics and CENIDE, University of Duisburg-Essen, Lotharstr. 1, 47057 Duisburg, Germany

[a)]martin.geller@uni-due.de

ABSTRACT

Self-assembled quantum dots are still one of the best model systems for artificial atoms in a solid-state environment, where the electronic states can be accessed by electrical and optical means. This article focuses on nonequilibrium carrier dynamics in these quantum dots, using the ability of recent developments in electrical and optical spectroscopy techniques. All-electrical transconductance spectroscopy is introduced, where a two-dimensional electron gas serves as a fast and sensitive detector for the electron/hole dynamics and charge/spin state preparation and relaxation in an ensemble of dots. Latest results on single electron tunneling and nonequilibrium Auger recombination in a single quantum dot using a high-resolution optical experiment (the time-resolved resonance fluorescence) are summarized. This article concludes with a perspective view on a future combination of both techniques toward an electro-optical measurement toolbox to link the coherent control of quantum states by optical means with an electrical preparation of electron charge and spin states.

TABLE OF CONTENTS

I. INTRODUCTION

Quantum dots (QDs) are the physical realization of a zero-dimensional structure in a solid state environment. They are "artificial atoms," and like real atoms, quantum dots exhibit a discrete density of states (DOS)[1] since they confine charge carriers within their de Broglie wavelength in all dimensions. Quantum dots are highly interesting for applications in optoelectronics: Possible applications include quantum dot lasers,[2–4] amplifiers,[5–7] photodetectors,[8,9] and memories.[10–13] Even more, quantum dots could be important building blocks[14] in quantum information processing[15–17] or devices that emit single or entangled photons.[18,19]

There are different types of quantum dots: (i) Colloidal semiconductor nanoparticles[20,21] (or colloidal quantum dots), (ii) lithography-defined (or gate-defined) dots[22,23] in a two-dimensional electron gas

(2DEG), and (iii) self-assembled semiconductor dots.[24,25] Colloidal quantum dots are small nanostructures without a surrounding matrix material. They can be produced with narrow size distribution using different techniques, for instance, laser ablation[26,27] or synthesis from the gas[28,29] or liquid phase.[30] Large quantities can be obtained, and these nanostructures are optically active; however, it is difficult to contact them by electrical means. From an application point of view, an electrical access to the optical and electrical properties of these nanostrucutres is a very convenient and interesting way to control the physical properties and, hence, the device characteristics. Such an electrical access is especially realized for lithography-defined dots in a two-dimensional electron gas by gate contacts[31,32] that allow coherent electrical manipulation of quantum states[33,34] and spins[35,36] for applications in quantum information processing. Such quantum dots are fabricated in a "top-down"-approach, where local oxidation with an atomic force microscope (AFM)[37–39] or electron-beam lithography on top of a two-dimensional electron gas[40,41] is used to produce the dots and the control gates.

Another possibility to produce a confinement in all spatial directions is a "bottom-up" approach, where two different material combinations with different lattice constants are deposited on top of each other. For instance, indium arsenide (InAs) can be grown with submonolayer precision on top of a gallium arsenide (GaAs) substrate. This forms small islands with a lateral size of 15–30 nm and a typical height between 3 and 8 nm. These self-assembled quantum dots[24,42] can be addressed by optical and electrical means, and like an atom, they show energy quantization, direct and indirect (exchange) Coulomb interactions, and angular momentum and spin-dependent optical[43–50] and electrical properties.[51–54] The combination of electrical and optical control makes self-assembled dots an ideal model system to test the interaction between electrically addressable charge states and a quantized light field in quantum optics.[55–57] Even more, transport in combination with optics enables us to measure here the nonequilibrium electron dynamics and understand the interaction phenomena between the quantum dots and their environment.

The following article will review the latest results on nonequilibrium charge carrier dynamics in self-assembled quantum dots. In this sense, it will describe recent developments of the electron/hole dynamics in time-resolved transconductance spectroscopy on an ensemble of quantum dots and the nonequilibrium electron dynamics of single dots studied by an optical detection scheme, i.e., resonance fluorescence (RF).[58–61] It is important to mention here that this article is not a representative review. It rather focuses on measurements done at the University of Duisburg-Essen, however, describing and referencing to many important results of other groups working in the area of optics and transport on self-assembled quantum dots.

This review is organized as follows: It will start in Sec. II with a basic overview on semiconductor nanostructures, followed by the description on the electronic properties of self-assembled quantum dots in Sec. III and their optical properties in Sec. IV. Afterward, this review will present the latest results on the nonequilibrium charge carrier dynamics in the time-resolved electrical measurement scheme in Sec. V and the optical resonance fluorescence measurements in Sec. VI. It will end with a conclusion and outlook in Sec. VII.

II. LOW-DIMENSIONAL HETEROSTRUCTURES

Using low-dimensional heterostructures[62] in combination with the so-called "band structure engineering" can tune precisely the electronic[63–65] and optical properties[56,66] of semiconductor devices. It alters the Bloch functions of the electrons in the crystal and, as a consequence, changes the most important ingredient: the density of states (DOS). "Low-dimensional" means a reduction of the dimensionality in at least one dimension, where one-dimensional reduction gives a two-dimensional electron gas (2DEG), and a confinement in all three spatial directions results in a quantum dot.[24,67]

For compound semiconductors, every material combination has its own lattice constant and energy gap. Starting, for instance, with III–V materials, already the pure binary compounds of AlP or InSb exhibit a huge difference in the energy gap, ranging from 2.5 eV to 0.17 eV. Moreover, the energy gap can be widely (and continuously) tuned by using different ternary (like InGaAs) or quaternary alloys (like InGaAsN). This opens up numerous possibilities to build electro-optical devices that can operate with different bandgaps and emit light from the near UV down to the infrared.[68]

Epitaxial growth techniques[69] are nowadays able to deposit different materials with submonolayer precision on top of each other. Starting with a substrate material, in a metal organic chemical vapor deposition (MOCVD)[70] or molecular beam epitaxy (MBE),[71] a semiconductor heterostructure can be obtained by such a bottom-up growth technique. One of the first and most common heterostructures is the interface between the two binary III–V compounds aluminum arsenide (AlAs) and gallium arsenide (GaAs), where AlAs has a larger bandgap at the Γ-point than GaAs. Both materials have almost the same lattice constant,[68] i.e., they can be grown on top of each other without any lattice mismatch and resulting strain. The material combination Al(Ga)As/GaAs with its interface is an important starting point to achieve a confinement for charge carriers in one direction. The result is a low low-dimensional quantum structure[63,72] with new electronic and optical properties: A so-called two-dimensional electron (2DEG)[73] or hole gas (2DHG).[74]

A. Two-dimensional electron gases

The strong confinement in one direction leads to a situation where the confinement direction can be ignored in most physical properties (hence, higher sub-bands are neglected) and the electrons (or holes) can move freely in the other directions. Such a two-dimensional nanostructure can be produced in different ways. It is found in transistor structures (the mentioned MOSFET), where it is formed below the gate oxide. In such a device, the Quantum-Hall effect was discovered.[75] Graphene as a monolayer (ML) of carbon atoms in a honeycomb lattice structure is also a two-dimensional electron system;[76] depending on doping or gate voltage, it can even be tuned from an electron to a hole gas.

Another possibility to form a two-dimensional electron gas is the epitaxial growth of an AlGaAs/GaAs interface. This method has the advantage of a very smooth interface with low disorder potential. Electron scattering is reduced, and charge carrier mobilities of more than 3×10^7 cm^2/V s have been reported.[77] The band structure at an AlGaAs/GaAs interface is shown in Fig. 1, where AlGaAs has a layer with n-doping, while GaAs is undoped (the so-called "modulation doping"). The electrons in the n-doped AlGaAs layer diffuse to the GaAs layer, where they form the 2DEG in the triangular potential. The triangular potential is a result of the electric field of the ionized donor in the doped AlGaAs and the potential step between the AlGaAs and GaAs layers. The spacer between the n-doped AlGaAs

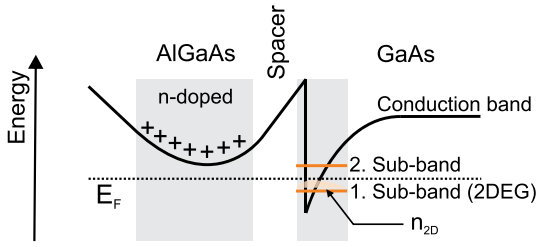

FIG. 1. Basic principle of a two-dimensional electron gas at an AlGaAs/GaAs interface. The electrons from the n-doped AlGaAs layer diffuse to the AlGaAs/GaAs interface, where the two-dimensional electron gas is formed in a triangular well. The spacer layer separates the ionized donor atoms from the electrons, suppressing Coulomb scattering with the positively charged donors.

and the AlGaAs/GaAs interface protects the charge carriers in the electron gas from Coulomb scattering with ionized donator atoms in the doping layer.

The density of states is constant in every sublevel of the two-dimensional electron gas. The energy difference between two sublevels can be calculated for an AlGaAs/GaAs interface by solving the Schrödinger equation,[73] where many-body Coulomb interaction reduces the sublevel spacing to experimental values of about 20 meV.[78] At temperatures below 50 K ($k_B T(50\text{K}) \approx 4$ meV) in the following experiments, the sublevel spacing ensures that the two-dimensional electron gas remains 2D, as the thermal energy is smaller than the energy spacing in the remaining third dimension.

B. Quantum dots

Self-assembled quantum dots can be produced by epitaxial growth using molecular beam epitaxy (MBE)[79] or metal-organic vapor deposition (MOCVD).[80] As an example, the growth of InAs/GaAs quantum dots starts on top of a GaAs substrate with a GaAs buffer layer. InAs has a larger lattice constant of approximately 7% compared to the GaAs substrate. A highly strained thin film of InAs is formed on GaAs as the InAs lattice constant adjusts to the GaAs substrate, up to a film thickness of about 1.5 monolayers (ML), see Fig. 2 (left). If the growth proceeds, the strained InAs layer relaxes into coherent (without dislocations and defects) tiny little islands after deposition of 2–4 monolayers during a growth interruption period, see Fig. 2 (middle). This is the Stranski-Krastanov growth mode.[81] Further deposition of InAs of more than 4 monolayers leads to bigger islands with dislocations and defects.

Depending on the growth parameters, these self-assembled quantum dots have a typical height of a few nanometers and diameter of a few tens of nanometers. With an area density of more than $1 \times 10^{11}\,\text{cm}^{-2}$, they exhibit a high homogeneity in their size distribution with a variation of only ~10%. Figure 3 shows an atomic force microscopy (AFM) image of two quantum dots on the sample surface. For optical experiments, the growth parameter can be changed

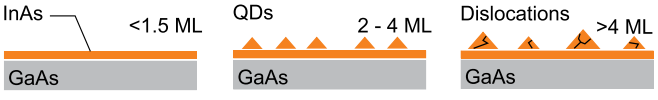

FIG. 2. Schematic illustration of the quantum dot growth procedure. On a GaAs substrate, InAs is deposited in a MBE or MOCVD growth process.

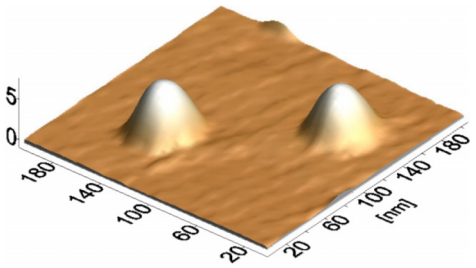

FIG. 3. Atomic force microscopy image of two self-assembled quantum dots. The dots are uncapped visible on the sample surface with an average height of 5 nm and a diameter of approximately 20 nm. Reproduced with permission from O. Wibbelhoff, "Ladungsträgerquantisierung in selbstorganisierten Nanostrukturen," Ph.D. thesis (University of Duisburg-Essen, 2006).[82]

accordingly to obtain the area density below $1 \times 10^8\,\text{cm}^{-2}$, i.e., less than one dot per μm^2.

C. Heterostructure devices

For active devices, the InAs dots are commonly integrated into a heterostructure of undoped/doped GaAs and AlGaAs layers, which allows controlled charging of the quantum states with electrons or holes (depending on the doping). One of the simplest structures is a p-i-n diode-like device, shown schematically in Fig. 4(a), where the InAs quantum dots are embedded in an undoped region of GaAs. The layer below the dots serves as the tunneling barrier [see Fig. 4(b)]. It separates the dot states from a doped region that is contacted by an Ohmic contact. The Ohmic contact to the n-doped layer (or the 2DEG in Fig. 5) can be achieved by evaporation of Ni/AuGe/Au on top of the sample surface and subsequent annealing at about 400 °C. The germanium atom produces a highly n-doped area (gray-shaded

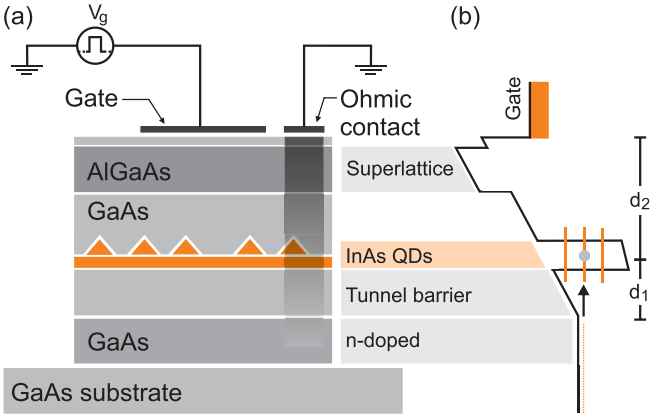

FIG. 4. Schematic picture of a diode structure with embedded quantum dots. (a) On top of a GaAs substrate, an n-doped layer serves as Ohmic back contact. The dots are sandwiched between the two layers of undoped GaAs, where the lower one serves as the tunneling barrier that separates the quantum states from the charge reservoir. A gate and an Ohmic contact allow controlled charging of the dot states by tunneling from the reservoir. The gray-shaded gradient area of the Ohmic contact should visualize that an electric contact to the n-doped layer can be achieved by evaporation and subsequent annealing of Ni/AuGe/Au on top of the sample surface. (b) Schematic conduction band structure of the device.

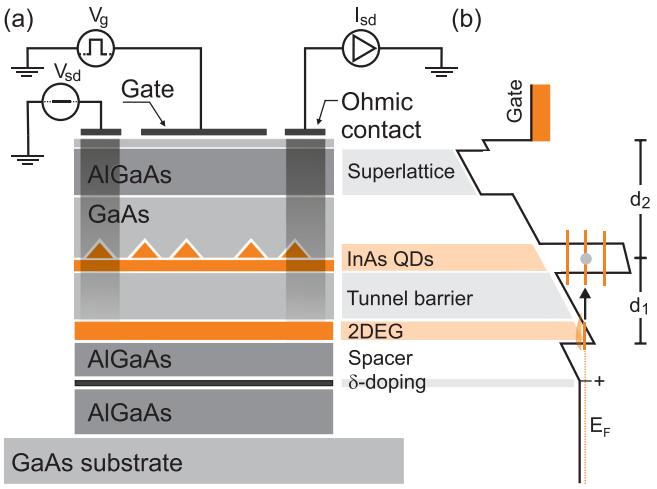

FIG. 5. Illustration of a high-mobility-electron-transistor (HEMT) structure with embedded quantum dots. (a) Below the tunneling barrier, the n-doped region of GaAs is replaced by a two-dimensional electron gas that is formed at an AlGaAs interface. The Ohmic contacts to the 2DEG can be achieved by evaporation and subsequent annealing of Ni/AuGe/Au on top of the sample surface (gray-shaded areas with gradients). (b) Schematic conduction band structure of the device.

area with a gradient in Fig. 4) by diffusion to the n-doped layer. A second contact is a metal gate on top of the AlGaAs/GaAs heterostructure.

An applied voltage V_g tilts the band structure in Fig. 4 such that the Fermi energy E_F in the doped back contact (the charge reservoir) can be tuned in resonance with the energy levels in the dots. This can be used to precisely control the number of electrons (or holes) inside the dots in optical experiments[83] or measure the quantum capacitance in capacitance-voltage (C-V) spectroscopy[51] (also in a magnetic field: The Fock-Darwin spectrum[84–86]).

A second device structure that is relevant within this review is a high-electron-mobility transistor (HEMT) structure. In such a device, the highly n-doped region of the diode structure in Fig. 4 is replaced by a two-dimensional electron gas.[87,88] The advantage is a feedback mechanism of the charged quantum dots on the conductance of the electron gas G_{sd}, determined by measuring the current I_{sd} between the source and drain contacts [see Fig. 5(a)]. Charging the quantum dots with electrons leads to a reduction of the charge carrier concentration in the 2DEG.[89,90] Time-resolved measurements of this conductance enables us to investigate the nonequilibrium tunneling dynamics from the reservoir into the dot states.

Figure 5 depicts schematically the layer sequence and the conduction band structure of the device. To be more precise, it is an "inverted" high-electron-mobility transistor since the doped layer is below (with respect to the growth direction) the two-dimensional electron gas. Moreover, in comparison to the electron gas described in Sec. II A, the n-doped layer is replaced by δ-doping, a highly doped thin layer. The δ-doping is separated from the two-dimensional electron gas by an AlGaAs spacer layer, while the quantum dots are again coupled by a tunneling barrier to the electron gas as the charge reservoir. The thickness and the material of the tunneling barrier determine the tunnel coupling strength, i.e., the average tunneling time between the dot states and the reservoir. It can be easily tuned from below nanoseconds up to more than seconds. The charge carrier mobility of the electron gas in the vicinity of a layer of quantum dots is often quite small, as the strain field induced by the dots acts as scattering potential. Typical values for the mobility are on the order of 1×10^4 cm^2/V s (Refs. 91–93) for a charge carrier density of $\sim 10^{11}$ cm^{-2}.

An important parameter for both device structures is the so-called lever arm.[94–96] With the tunneling barrier of thickness d_1 and a thickness of the layer sequence on top of the quantum dots (the so-called "blocking layer") of d_2 [see Figs. 4(b) and 5(b)], a change in gate voltage ΔV_g applied between gate- and Ohmic-(back)-contacts translates into an energy shift of

$$\Delta E = e\Delta V_g \frac{d_1}{d_1 + d_2}. \quad (1)$$

The ratio between the distance $d_1 + d_2$ (surface to reservoir) and d_1 (dot layer to reservoir) is called the lever arm $L = (d_1 + d_2)/d_1 = e\Delta V_g/\Delta E$ and relates the applied gate voltage to the energy shift at the quantum dot position. The lever arm varies in different samples slightly; however, it is typically in the range between 6 and 10.

III. QUANTUM DOTS: ELECTRONIC PROPERTIES

In Sec. III, the basics of the electronic structure of self-assembled dots will be briefly summarized. The small structural size of the dots (in comparison to the de Broglie wavelength) gives the strong confinement in all three spacial directions. However, in more detail, the electron structure of these nanostructures can be quite complicated, as we have to keep in mind that the electrons live in a crystal structure. They are quantum mechanical Bloch waves[97,98] that interact with the crystal structure. Therefore, besides the shape of the dots, the lattice, strain, piezoelectric effects, and the chemical composition have to be taken into account to determine the wavefunctions and energy levels. This can be done in a numerical calculation, for instance, starting from the bulk material (and using its parameters) in 8-band-$\mathbf{k}\cdot\mathbf{p}$ calculations[1,99,100] or from the atomic levels in atomistic pseudopotential theory.[101,102]

A. Two-dimensional harmonic oscillator

A much more simple approach is to squeeze the influence of the underlying crystal mostly in one parameter: the effective mass m^*. A single-band effective mass approximation[103] will neglect every mixing of the orbital states and is especially questionable for the hole states, where this mixing plays an important role in the eigenstates and energies.[99] However, to interpret the following experiments, using the effective mass is a reasonable approximation. The crystal lattice is, hence, neglected, and one has to be aware that in the following, only the envelope of the Bloch wavefunctions is shown in the schematic pictures.

To further simplify the situation, the confinement of a quantum dot can be separated into two parts, see Fig. 6, where the smaller height of the dots in the growth direction (z-axis) leads to a stronger confinement than in the lateral extension in the x-y-plane. This means that the energy spacing between the ground state ($n_z = 1$) and the first excited state ($n_z = 2$) in the z-direction is much larger than the level spacing in the x-y-plane. At temperatures below T = 10 K and for every gate voltage applied, the system is always in the ground state with respect to the confinement in the z-direction. This confinement in the z-direction can be described approximately by a finite potential

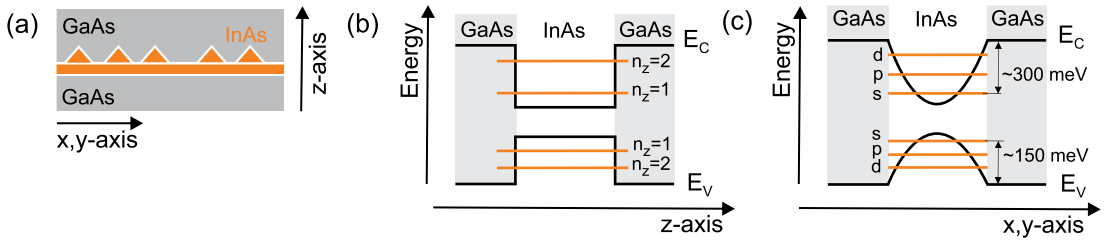

FIG. 6. Simplified description of the potential profile in a self-assembled quantum dot. (a) For InAs dots embedded in a GaAs matrix material, the potential can be separated into a part in the x-y-(lateral)-direction and another the in z-(growth)-direction. (b) The potential into the growth direction can assumed to be a finite square well with quantum numbers $n_z = 1, 2, 3,\ldots$. (c) The more important part is the potential in the x-y-direction which can be approximated by a two-dimensional harmonic oscillator. The labeling with s-, p-, and d-shells is imitated from atomic physics.

well with a quantum number $n_z = 1,2,\ldots$, as schematically depicted in Fig. 6(b), where the ground state $n_z = 1$ would have an s-like and the first excited state $n_z = 2$ have a p-like symmetry of the wavefunction. As we can separate this z-component of the wavefunction (where the system is in the ground state), we are left with two-dimensional confinement in the direction of the x,y-axis, depicted in Fig. 6(c).

As a further simplification, the confining potential in the x-y-plane can be described by a two-dimensional harmonic oscillator[104–106] since the "lens-like" shape (A lens-like shape of the quantum dots is a further approximation, as dots with a pyramidal shape have also been reported in the literature.[107,108]) (cf. Fig. 3) produces an adiabatically varying potential with strong confinement (corresponding to large bandgap) at the edges and weak confinement in the middle of the dot.[109] Figure 6(c) schematically depicts the harmonic potential for the valence and conduction bands as solid black lines. The Schrödinger equation of a two-dimensional harmonic oscillator in Cartesian coordinates

$$\left(\frac{\hbar^2}{2m^*}\Delta + \frac{1}{2}m^*\omega_0^2\left(x^2+y^2\right)\right)\psi(x,y) = E\psi(x,y) \tag{2}$$

is "text-book knowledge" and can be easily solved with the effective mass m^* and the characteristic frequency ω_0 of the harmonic potential. The eigenstate is the well-known product of the wave function of the harmonic oscillator with the Hermite polynomial for the x- and y-directions (see, for instance, Refs. 110 and 111). The eigenenergies in Cartesian coordinates are therefore given as

$$E_{n_x,n_y} = (n_x + n_y + 1)\hbar\omega_0, \tag{3}$$

with the two quantum numbers for the x- and y-coordinates: $n_x, n_y = 0, 1, 2, \ldots$. The quantum numbers n_x and n_y give also the number of nodes of the (envelope) wave function in the x- or the y-direction, respectively. The ground state with quantum numbers n_x, $n_y = 0$ is an s-like state with no nodes.

A more suitable way for a lens-shaped quantum dot with rotational symmetry is to solve the Schrödinger equation in cylindrical coordinates, where the radius from the origin r and the angle ϕ are used as coordinates. The eigenfunctions have now rotational symmetry (see Fock[112] and Darwin[113] for more details), and two quantum numbers n and l are needed again to characterize the system and get the same energies in a different (and more convenient) notation

$$E_{n,l} = (2n + |l| + 1)\hbar\omega_0, \tag{4}$$

where $n = 0, 1, 2,\ldots$ is the radial quantum number and $l = \ldots -2, -1, 0, 1, 2\ldots$ is the quantum number for the angular momentum (Note here that the absolute value of the angular momentum $|l|$ has to be used to get the eigenenergies.). A linear combination of the wave functions in Cartesian coordinates $\psi_{1,0}(x,y)$ and $\psi_{0,1}(x,y)$ (one node in x- and y-directions) gives clockwise and anticlockwise rotating wavefunctions

$$\psi_{0,1}(r,\phi) = a\,\psi_{1,0}(x,y) + i\,b\,\psi_{0,1}(x,y), \tag{5}$$

$$\psi_{0,-1}(r,\phi) = a\,\psi_{1,0}(x,y) - i\,b\,\psi_{0,1}(x,y). \tag{6}$$

As an example for the two first excited states, these rotating waves have angular momenta of $l = -1, 1$. This means that we can translate the quantum numbers in Cartesian coordinates with quanta for x- and y-directions (n_x, n_y) into quantum numbers that describe clockwise (right n_r) or counterclockwise (left n_l) rotation wave functions, i.e., $E = (n_x + n_y + 1)\hbar\omega_0 = (n_l + n_r + 1)\hbar\omega_0$. Whenever the number of clockwise- (n_r) and counterclockwise-rotating (n_l) quanta differ, one gets an angular momentum, where the direction of the net circulating quanta yields a plus or a minus sign for l.

With this, we can label our single particle quantum states in a two-dimensional harmonic oscillator that describes sufficiently our quantum dot for the following experiments: We use the Dirac notation $|n,l\rangle$ in Fig. 7, with n as the radial quantum number and l as the quantum number for the angular momentum. Taken from atomic physics, the quantum states are sorted in shells that are labeled with s, p, or d, depending on the angular momentum. However, there are some strong differences between the $1/r$-potential for an atom and a two-dimensional harmonic oscillator: The quantum states are not degenerate with respect to the main (radial) quantum number n for a

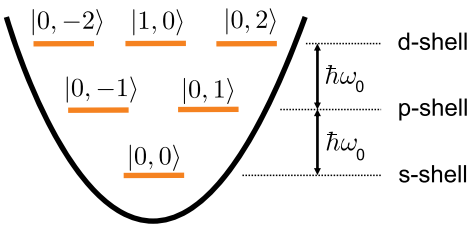

FIG. 7. The quantum numbers in a two-dimensional harmonic oscillator. In Dirac notation $|n,l\rangle$, n is the quantum number for the radial component (the main quantum number in atomic physics) and l is the quantum number for the angular momentum.

two-dimensional harmonic oscillator, i.e., states exist for the same n with different angular momenta, such as $|0,-1\rangle$, $|0,1\rangle$, $|0,-2\rangle$ and $|0,2\rangle$. Moreover, the state $|1,0\rangle$ in the d-shell is not a d-like state as in a hydrogen atom, as it has no angular momentum. In atomic physics, it would be an s-like state (as it has $l=0$) with one node of the wave function in the radial direction. Here, for a harmonic oscillator, this state is degenerate with the $l=2$-states and, hence, sorted into the d-shell.[114]

B. Electronic shell structure

The electronic structure of the two-dimensional harmonic oscillator can be seen in capacitance-voltage (C-V) measurements, where the quantum dots are embedded in a Schottky-diode structure.[86] The layer structure of such a device is shown in Fig. 4. The quantum dots are embedded in an undoped (intrinsic) region of GaAs between the n-doped back contact and the metallic Schottky gate on top of the structure. The capacitance is measured with respect to the applied gate voltage V_g in Fig. 8. The measured capacitance can be separated into three parts: (i) the geometric capacitance, (ii) the depletion capacitance, and (iii) the quantum capacitance.

The geometric capacitance of such a p-i-n diode structure is the same as for a plate capacitor $C_{geo}=\frac{\epsilon_0\epsilon_r A}{d}$, with the dielectric constant of GaAs and AlGaAs. It is responsible for the constant capacitance background of about 220 pF in Fig. 8(a). On top of this constant background is the slope of the depletion capacitance, visible as slightly rising capacitance between $V_g=-1.5$ and -0.9 V. This depletion capacitance is well known from p-n-junctions[115] and used in time-resolved capacitance spectroscopy measurements on defects (deep level transient spectroscopy—DLTS)[116,117] and quantum dots.[10,118–121] The depletion capacitance is proportional to the square root of the doping concentration N_d and inversely proportional to the applied gate bias (with the built-in voltage V_{bi} of the p-n diode) for an abrupt junction[115]

$$C_{depl}=\sqrt{\frac{q\epsilon_0\epsilon_r N_d}{2(V_{bi}-V_g)}}. \tag{7}$$

Therefore, for the constant doping concentration, the capacitance increases quadratically with the applied gate voltage and has a constant curvature. Weak curvature means a high doping concentration, as it can be seen in the slightly increasing capacitance in Fig. 8 up to $V_g=-0.9$ V.

The quantum capacitance[87] is the important part which leads to the observation of the shell structure of the dots in the capacitance-voltage measurement. It is proportional to the density of states and can be seen as six pronounced maxima between $V_g=-0.75$ V and 0.3 V in Fig. 8(a). As schematically depicted in Fig. 8(b), if the gate voltage is set to $V_g=-0.75$ V, the Fermi energy in the n-doped back contact gets in resonance with the first energy level (the s_1-state). In a capacitance measurement with an applied ac-voltage, the electrons can tunnel now back and forth between the reservoir and the dot states. This resonance effect is visible in a maximum in the spectrum due to the additional quantum capacitance of the dot states (see Russ *et al.*[87] for more details). The twofold spin degenerate is lifted in a static capacitance measurement by Coulomb repulsion of the electrons, and the second dot state in the s-shell (the s_2-state) is visible separately at $V_g=-0.55$ V. The Coulomb repulsion energy of ~20 meV can be

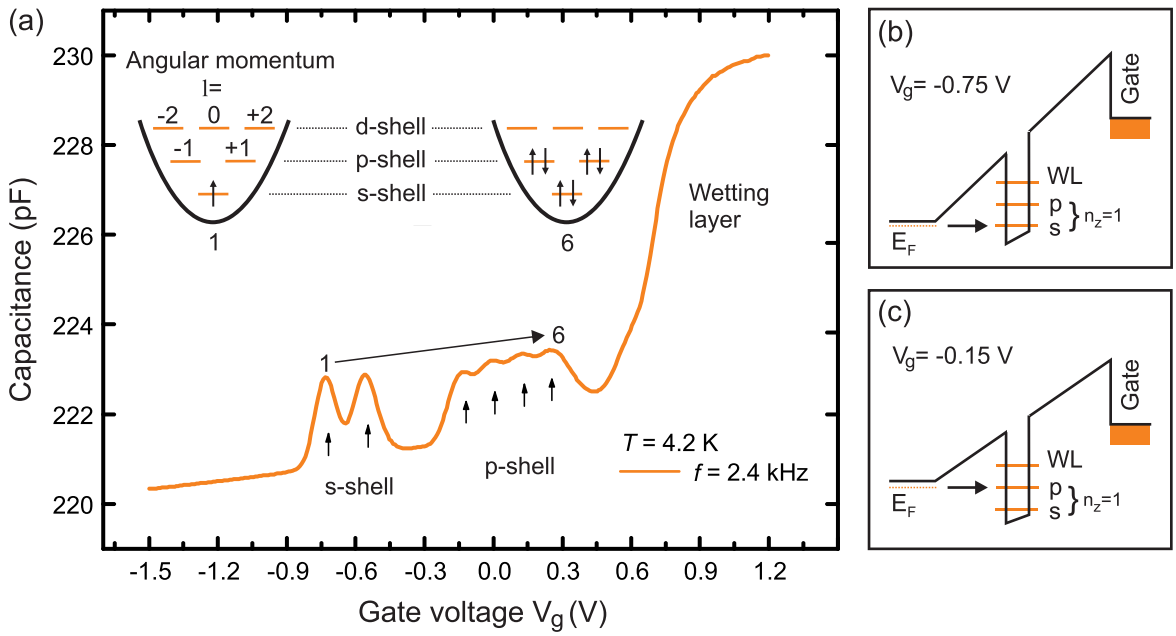

FIG. 8. Static capacitance-voltage (C-V) measurement of a layer of InAs/GaAs quantum dots. (a) The six charging maxima (1.6) resemble the shell structure of a two-dimensional harmonic oscillator with s-, p-, and d-shells (see the schematic insets). (b) At a gate voltage of $V_g=-0.75$ V, the Fermi energy in the doped back contact is in resonance with the first *s*-state (s_1) in the quantum dots, (c) whereas at -0.15 V, the Fermi energy gets in resonance with the first state of the *p*-shell (p_1). The degeneracy of all states is lifted in a static C-V measurement due to Coulomb interaction. The figure is adapted with permission from Wibbelhoff.[82]

determined by the voltage separation between the s_1- and s_2-states and using Eq. (1) for the lever arm. At a gate voltage of $V_g = -0.15$ V, the Fermi energy gets in resonance with the p-shell (see schematic picture in Fig. 8). The energy difference between the s- and the p-shell is mainly due to the quantization energy (~50 meV); however, Coulomb and exchange interactions have also a significant influence. An approximate value for the Coulomb and exchange interactions can be calculated in a first order perturbation theory between two particles by using single particle wavefunctions of a two-dimensional harmonic oscillator (see Warburton *et al.*[85]).

The capacitance spectrum in Fig. 8 is recorded on an ensemble ($>10^7$) of quantum dots in a near-equilibrium situation, where the electron tunneling into and out of the quantum dot states is balanced. The capacitance of a single self-assembled quantum dot is very small, on the order of ~attofarad, so that single-dot measurements are very challenging.[86,122] In this "static" capacitance measurement, the degeneracy of the states is lifted by Coulomb interaction, and the maxima in the spectra are homogeneously broadened by the statistical variation of size, shape, and composition of the dots.

IV. QUANTUM DOTS: OPTICAL PROPERTIES

One of the big advantages of self-assembled quantum dots is the possibility to combine both transport and optics for measurements on the electron dynamics. The basics about the optical properties of quantum dots and the main experimental methods, including photoluminescence (PL) and resonance fluorescence (RF), will be summarized briefly in this section.

A. Photoluminescence spectroscopy

One of the most important optical spectroscopy methods is photoluminescence (PL) spectroscopy.[123,124] A laser with a photon energy greater than the bandgap of the matrix material (here: GaAs with 1.52 eV) is used to generate high-energy excitons in the area surrounding the dots (blue transition in the upper-right inset of Fig. 9). These electron-hole pairs can relax into the dot states by electron-electron and/or phonon scattering.[125–128] The confined excitons recombine inside the quantum dots with an energy relaxation T_1-time on the order of nanoseconds and a wavelength between ~900 and 1300 nm, depending on their size (and shape and composition).

The photoluminescence measurement on an ensemble of InAs/GaAs quantum dots is shown in Fig. 9, where the exciton transition between the s-shell in the conduction band and the s-shell of the heavy holes in the valence band is visible at 1150 nm. The p-p transition can be observed at 1125 nm. These transitions have a strong overlap of the envelope functions of the s-like electron and hole wave functions in real space, and the atomic part of the Bloch wave functions gives in addition a strong matrix dipole element (transition between s-like symmetry in the conduction band to p-like symmetry in the valence band). The inhomogeneous linewidth is on the order of 50 meV in such an ensemble measurement on millions of self-assembled dots. As a consequence, the energy separation between s-s and p-p transitions (see Fig. 9) is purely due to the quantization between s- and p-shells, and every influence of Coulomb or exchange interaction (<20 meV) on the exciton transitions is hidden within the inhomogeneous broadening.

In order to reveal the emission spectrum from an individual dot with its few-particle interactions, the number of dots within the excitation spot has to be reduced strongly. In principle, there are two approaches that are used together to obtain the luminescence spectrum of single quantum dots (as shown in Fig. 10): (i) First, in a microphotoluminescence (μ-PL) setup,[48,83,103,129–131] the excitation spot size will be reduced to the diffraction limit, which is approximately 1 μm for the typical wavelength range of InAs/GaAs dots (900–1300 nm). (ii) Second, the number of dots per area can be reduced to approximately one per square micrometer. Etching of small mesa structures[48]

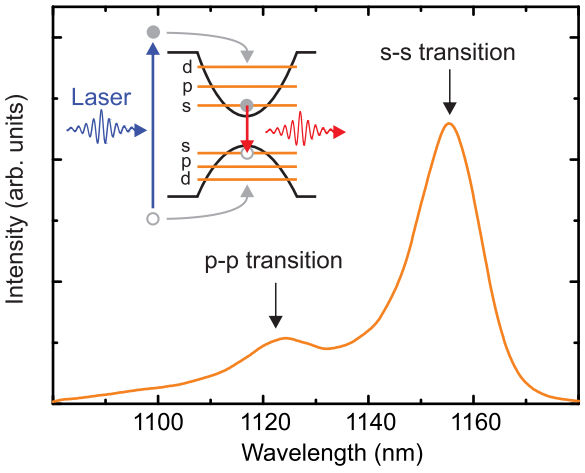

FIG. 9. Photoluminescence on an ensemble of InAs/GaAs quantum dots. Electron-hole pairs are generated by laser excitation in the matrix material that surrounds the quantum dots. These charge carriers can relax into the dot states and recombine as s-s- and p-p-shell transitions.

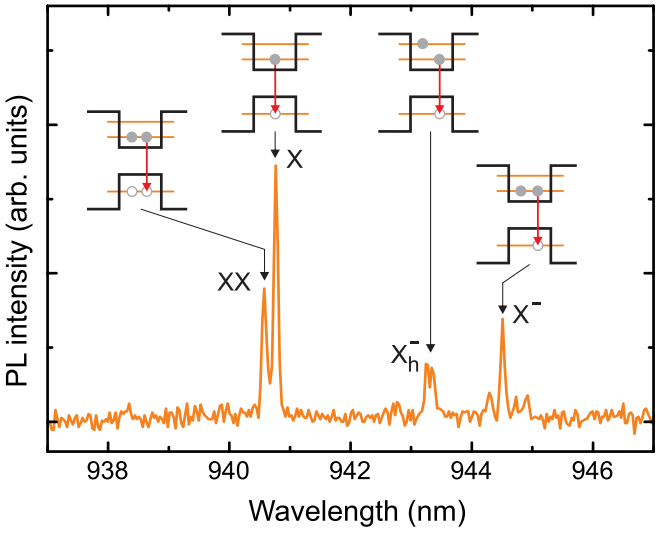

FIG. 10. Microphotoluminescence (μ-PL) spectrum of a single self-assembled InAs/GaAs quantum dot. Different maxima originate from different recombination configurations within the s-s-shell transition (X: exciton; XX: biexciton; X^-: negatively charged exciton (trion); and X_h^-: "hot trion"). Coulomb and exchange interactions alter the transition energy from the excitonic transition in the presence of additional electrons/holes in the dot.

or processing of small metal apertures,[132,133] using prepatterning before the quantum dot growth[134–139] or selective growth on buried stressor layers,[140,141] is just some of the possibilities to achieve the second goal.[139,142]

Another possibility that is used without prepatterning (that could harm the optical properties) is reduction of the InAs film thickness to a critical point where just a few dots per micrometer square nucleate.[143] This can be achieved in MBE and MOCVD growth by stopping the wafer rotation and growing a thickness gradient of InAs on the sample, leading to areas with high dot density, areas with no dots, and areas with the desired density of approximately one dot per square micrometer. Moreover, the emission wavelength can be blue shifted by rapid thermal annealing[144–146] or indium flushing after the dots were covered with a thin layer of GaAs.[147,148] Annealing or indium flushing leads to a diffusion of InAs to the surrounding GaAs matrix and reduction of the dot height, thus blue-shifting the wavelength below 1000 nm to a range where Si-based detectors (charge-coupled devices—CCDs and avalanche photodiodes—APDs) are working with high quantum efficiency.

Figure 10 shows such a μ-photoluminescence spectrum of a single self-assembled quantum dot, measured at 4 K in a Helium bath cryostat. The wavelength of different charge configurations of the exciton transitions was blue shifted to about 940 nm. Every maximum corresponds to an "exciton transition" between the s-shell in the conduction and the s-shell in the valence band. The different transition energies are due to the Coulomb interactions between electrons and holes (see schematic insets in Fig. 10).[85,149] The exciton transition is labeled with X and consists of one electron-hole pair.[150,151] Two electrons and two holes form the biexciton (XX—an exciton transition in the presence of another exciton), an exciton with an additional electron in the s-shell is called a negatively charged trion (X^-) or "hot-trion" (X_h^-), if the additional electron is in an excited state.[152]

In combination with an electrical diode structure (as depicted in Fig. 4), an electric field can be applied which changes the electrostatic energy of the electrons/holes in the quantum dot. Changing the electric field at the position of the quantum dot has two effects that can be seen in Fig. 11, where the photoluminescence intensity is shown as a function of the wavelength and applied gate voltage V_g: (i) It changes the probability for electrons to tunnel into the dot. (ii) The transition energies are shifted as a result of the quantum-confined Stark effect.[153–155] The transition lines decrease in the wavelength as the gate voltage is increased in Fig. 11.

Changing the probability for electron tunneling into the dot by the applied gate voltage changes the average occupation of the dot with electrons. If the tunneling rate between the dot and the charge reservoir is higher than the recombination rate (that means, the tunneling rate is above gigahertz), the quantum dot will be always in an equilibrium situation with the charge reservoir. In this situation, increasing the gate bias increases the average occupation in the quantum dot with electrons. Starting from an empty to a quantum dot with one or two electrons, sharp transitions between the exciton (empty dot) and charged trions (one or two electrons in addition to the exciton) are visible (demonstrated before in Warburton *et al.*[83]). If the tunneling rate between the dot and the charge reservoir is much smaller than the recombination rate (as in Fig. 11), different exciton transitions overlap strongly in gate voltage (without sharp transition between different exciton complexes). The number of electrons inside

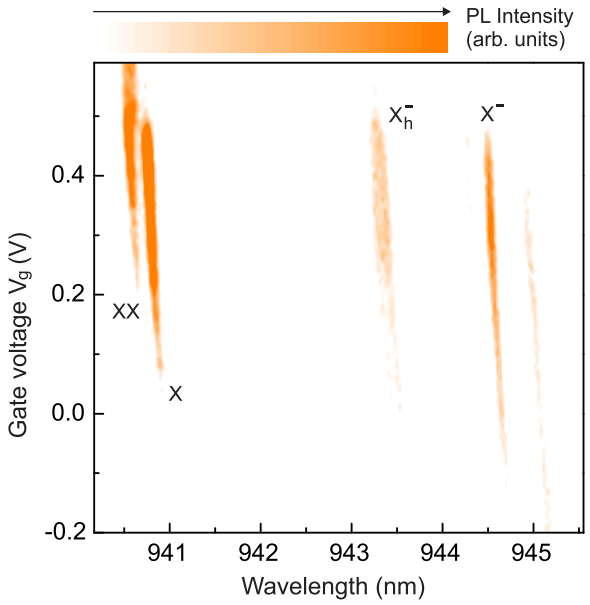

FIG. 11. Microphotoluminescence 2D-(μ-PL) map of a single self-assembled InAs/GaAs quantum dot. Different bright orange lines correspond to different excitonic transitions. Changing the gate voltage changes the probability of the number of electrons present in the dot during the photon emission. The small decrease in the wavelength of every transition line for the increasing gate voltage is due to the quantum-confined Stark effect.

the dot for a specific gate voltage depends now strongly on the capture rates of the electrons and holes into the dot states in the photoluminescence measurement.

The excitonic transitions of the quantum dot can be described as a two-level system, where the empty dot is the ground state $|0\rangle$ and the exciton configuration is the excited state $|1\rangle$. A two-level system will always have single-photon character. This single photon emission makes self-assembled dots promising building blocks for future applications in quantum information technologies.[156–158] Many groups have investigated and optimized the single-photon emission from a single self-assembled quantum dot[159–162] to get, for instance, highly indistinguishable photons[50,163–167] or address single electron (or hole) spins. The electron or hole spin can be used as a stationary spin-qubit, where it can be detected[168–171] and manipulated[172–174] by optical means, and the information of the spin state can be transferred to single photons as flying qubits by a spin-photon interface.[175–178] The orientation of the electron spin in the quantum dots is then encoded in the polarization of (at best) the single and indistinguishable photon.

Extracting these single photons into one direction is the next major challenge. For instance, the quantum dots can be coupled to a waveguide[179] in a photonic crystal.[180] The waveguide guides the photons into the right direction (a fiber of fiber coupler), while the photonic crystal shortens the lifetime[181] by the Purcell-effect,[182] giving a higher number of photons per second in the so-called weak coupling regime. The same effect has a microcavity in the weak coupling regime, experimentally explored by a number of groups.[183–186] In the strong coupling regime,[187–190] the light-matter interaction between the excitons in the quantum dot and the cavity modes gets so strong that

the photon is reabsorbed, emitted, and reabsorbed, giving rise to Rabi oscillations.

B. Resonant excitation and resonance fluorescence

Another optimization of the single photon generation is to use resonant excitation. In the photoluminescence measurements before, the excitons are generated in the surrounding matrix material of the quantum dot in a photoluminescence measurement. The charge carriers relax into the dot states randomly, and the charge state is not always perfectly controllable, as visible in the two-dimensional photoluminescence map in Fig. 11. Moreover, the spectral resolution in PL measurements is mostly limited by the resolution of the spectrometer (about 30 μeV). A much higher spectral resolution can be achieved by using resonant excitation methods,[191] where the laser excitation energy equals the transition energies. No charge carriers are generated in the vicinity of the dot, and the light-matter coupling of a two-level system (as a text-book system in quantum optics[192–194]) can be studied directly.

The spectral resolution is no longer limited by the spectrometer; it is given by the uncertainty of the applied gate voltage (as the Stark effect shifts the transition energy) and the spectral bandwidth of the laser light. As a consequence, the resonant light scattering has a much higher spectral resolution of up to 0.05 μeV. However, the challenge is now to separate the resonantly scattered photons from the excitation laser light. One possibility is to interfere the coherently scattered quantum dot photons with the excitation laser again in a so-called differential transmission (or reflection) measurement.[195–199] Another experimental method is the resonance fluorescence, which will be briefly discussed in the following.[200]

In the first experiments of resonance fluorescence on a semiconductor quantum dot,[58,201,202] the photon emission from the dot was detected at normal incidence to the sample surface, while the laser excites the dot from the side. Muller *et al.*[58] used in addition a planar mirror cavity to further reduce the light scattering into the detection optics. With the same intention, Melet *et al.*[59] excited the dots in a ridge waveguide structure.

A different geometry for the resonance fluorescence experiments is excitation and detection along the same axis,[49,203–205] as schematically depicted in Fig. 12. The sample is placed on a piezostage that can move in all three dimensions. Together with a high-numerical aperture (NA) microscope objective and a solid immersion lens (SIL) on top of the sample, these parts are placed in a Helium cryostat, operating at $T = 4.2$ K. The microscope objective focuses the excitation laser to a spot size of about 1 μm, while the zirconium SIL enhances the coupling efficiency back into the detection path.[198]

The resonance fluorescence setup works now as follows: A tunable and frequency-stabilized laser that is coupled into a single-mode excitation fiber (see Fig. 12) is collimated in free space and passes a high-quality polarizer (extinction ratio $>10^7$) before reflected into the direction of the quantum dot sample by a 90/10 beam splitter. 90% of the laser light is transmitted onto a photodiode that is used to monitor the laser light excitation power; the other 10% is used for the resonant excitation. After dot excitation, the scattered quantum dot photons are collected by the microscope objective again and pass the same 90/10-beam splitter before directed through a second polarizer. The CCD camera gives an image of the sample surface with the focused laser spot for alignment.

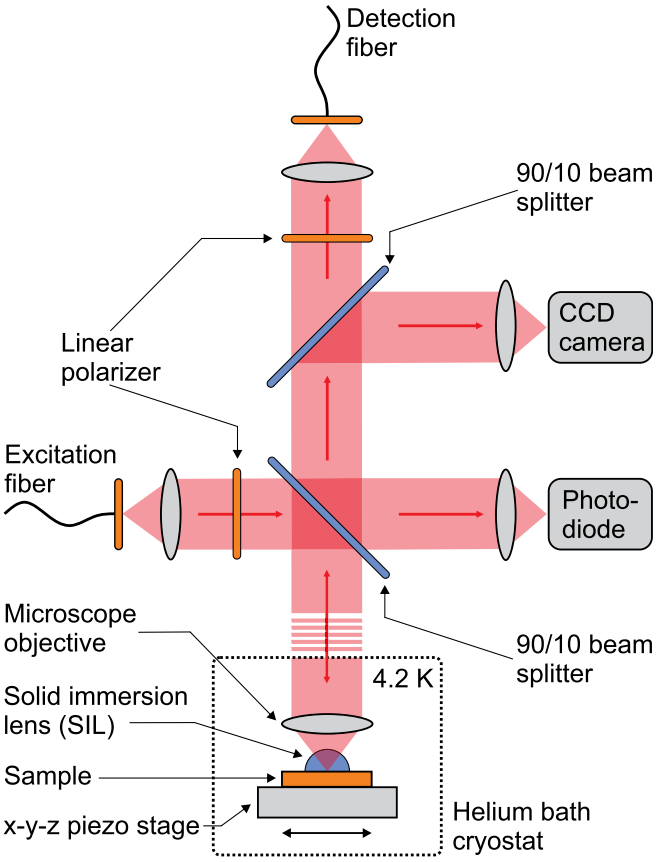

FIG. 12. Schematic picture of a resonance fluorescence setup. The laser light from the excitation fiber is collimated, passing a linear polarizer and a 90/10 beam splitter before focused onto the sample by a microscope objective through a solid immersion lens (SIL). The sample with a layer of self-assembled quantum dots is mounted on a piezostage that can be moved in all directions. The quantum-dot photons are collected by the objective again, passing two beam-splitters and a second linear polarizer before being focused onto the detection fiber. The photo-diode is used to monitor the laser power, while the CCD camera provides an image of the laser spot on the sample surface.

The second polarizer is set to cross-polarization. The laser light is scattered on the sample surface, conserving mostly the polarization angle, while the self-assembled quantum dot rotates the polarization angle. As a consequence, the directly scattered laser light photons are blocked, while parts of the quantum dot photons can pass the second polarizer and will be directed into the detection fiber. By adjusting both polarizers precisely, the laser background can be suppressed by a factor of more than 10^7, and the ratio of the laser to dot photons reaches the values of more than 1:1000, i.e., counting single photons on an avalanche photon diode (APD) gives just one "wrong" laser photon on 1000 "correct" dot photons.

Resonant excitation (including resonance fluorescence and differential transmission) is perfectly suitable to study the text-book quantum optics of resonant interaction between a two-level system and the light field[193,194,206] and realize the optical manipulation of quantum states.[207] Moreover, in combination with single photon detection, strong light-matter coupling in Rabi-oscillations,[208,209] the observation

of the Mollow-triplet,[49,202,210] photon entanglement,[211,212] and photon light squeezing[213] have been demonstrated in resonance measurements. This review shows in this chapter another possibility to use the resonance fluorescence: As a fast detector for nonequilibrium electron dynamics of a single self-assembled quantum dot.

Coming back to the light-matter interaction, the two levels of ground (empty dot) and excited (exciton) states are separated by an energy difference of $E = \hbar\omega_0$. In a semiclassical approach (the light field is treated by a monochromatic electromagnetic wave), the time-dependent Schrödinger equation has to be solved for a laser energy that is close to the transition energy. The light field is treated as a perturbation to the system. Without any damping or dephasing, the probability $n_1(t)$ for finding the system in the upper state $|1\rangle$ is then

$$n_1(t) = \cos^2(\Omega_R t/2), \tag{8}$$

with the Rabi frequency $\Omega_R = \mu_{01}\mathcal{E}_0/\hbar$, where μ_{01} is the dipole matrix element and $\mathcal{E}_0$ the amplitude of the electric field. This equation is slightly modified, if the laser energy is not exactly in resonance with the transition

$$n_1(t) = \frac{\Omega_R^2}{\Omega}\cos^2(\Omega t/2), \tag{9}$$

where

$$\Omega^2 = \Omega_R^2 + \delta\omega^2, \tag{10}$$

with $\delta\omega$ as the detuning.[193,194] The frequency of the Rabi oscillations increases, while the amplitude decreases as the laser light is more detuned to the resonance.

The probability of finding the system in the upper level $n_1(t)$ (the same is true for the lower level) oscillates back and forth between the two levels with the Rabi angular frequency Ω (or Ω_R without detuning). Increasing the laser excitation power decreases the transition time from an empty dot to a dot containing one exciton. This creates a coherent superposition between the ground $|0\rangle$ and excited $|1\rangle$ states: $|\psi(t)\rangle = \alpha(t)|0\rangle + \beta(t)|1\rangle$, where the probability $n_1(t)$ is the square of the complex amplitudes: $n_0(t) = |\alpha(t)|^2$ and $n_1(t) = |\beta(t)|^2$.

However, in an experiment, it is not easy to observe the Rabi flopping as coherent oscillations. The experimental observation needs strong laser beams, and the laser has to be pulsed, so that the pulse energy can be varied and the final superposition state can be determined by changing the pulse duration or the laser intensity.[58,59,214] Moreover, every quantum mechanical system is subject to decoherence (damping) that changes the amplitude and phase of the quantum state. At low laser powers, the Rabi oscillation period would be longer than the decoherence time. Therefore, high powers are needed to shorten the Rabi period time, at least as sufficiently high that the period is shorter than the radiative lifetime (i.e., the spontaneous emission time).

The decoherence is characterized by two time constants T_1 and T_2^*. In the derivation from Bloch *et al.*[215] for nuclear magnetic resonance, T_1 corresponds to inelastic scattering events, whereas T_2^* corresponds to elastic, energy-conserving, scattering events. The inelastic events (T_1) change the amplitude of the state. For instance, for a spontaneous emission event, the decay to the ground state occurs spontaneously and destroys in this moment completely the coherence of the wave function. The T_2^*-time is related to an elastic scattering process that destroys just the phase of the wave function (for instance by electron-electron scattering). In most situations, both dephasing processes (elastic and inelastic) are present, and the total dephasing rate is given by

$$\frac{1}{T_2} = \frac{1}{2T_1} + \frac{1}{T_2^*}, \tag{11}$$

where T_1 is still the above-mentioned time constant for the dephasing by population decay. However, T_2 gets here (as in most of the literature studies, too) a different meaning. It is now the sum of the dephasing by population decay T_1 and the so-called "pure dephasing" time T_2^*.

The environment is a strong source of different dephasing processes for quantum dots, where mainly the spin noise and charge noise dominate the T_2^*-time. Charge noise shifts the quantum dot transition energies via the quantum-confined Stark effect.[61,216,217] Charge carrier fluctuations in the environment dominate in nonresonant excitation experiments and samples with high defect densities. The spin noise originates from the small fluctuations in the spin bath of about 10^5 nuclear spins in the dot.[61,218–220] The orientations of the nuclear spins are randomly distributed and are not equalized to zero.[221] The hyperfine contact interaction couples the effective Overhauser field of the fluctuation nuclear spins to the electron spin in the dot.

A system with dephasing mechanisms cannot be described by the Schrödinger equation, as it is only valid for pure quantum states. Using the density matrix for incoherent statistical mixtures[194] gives the average occupation probability in equilibrium of the upper level with the dephasing time constants T_1 and T_2 (Ref. 58)

$$n_1 = \frac{1}{2}\frac{T_1/T_2\Omega^2}{\Delta\omega^2 + 1/T_2^2 + T_1/T_2\Omega^2}. \tag{12}$$

This equation describes the resonance fluorescence signal as a function of the excitation power. As the number of photons emitted by the dot is directly proportional to the occupation probability of the upper level n_1 (in a steady-state situation) and the laser excitation power P is linked to the Rabi frequency $\Omega^2 \propto P$, Eq. (12) describes also the fluorescence intensity as a function of the laser power (shown as a solid line in Fig. 13 for a trion transition). The fluorescence intensity is calculated by $I(P) = I_0 n(P)$ at constant detuning $\delta\omega$ by using Eq. (12) and can be fitted to the data in Fig. 13. The resonance fluorescence intensity starts to saturate above $P = 0.1\ \mu\text{W}/\mu\text{m}^2$, where the average occupation n_1 approaches $n = 0.5$ (i.e., the dot is half of the time occupied with an exciton or a trion) and the recombination rate equals the absorption rate. This will be of importance later.

The intensity of exciton and trion transitions for different laser excitation energies and gate voltages is shown in Fig. 14(a). The applied gate voltage induces the quantum-confined Stark effect[153] that shifts the resonance frequency. The exciton transition energy shifts from 1.30885 eV at $V_g = 0$ V to 1.3093 eV at $V_g = 0.26$ V. At this gate voltage, an electron tunnels into the quantum dot and the exciton transition is quenched. The trion transition is located at lower energy due to the stronger attractive electron-hole Coulomb interaction than the repulsive electron-electron interaction.

The fluorescence signal from the exciton and trion transitions is shown independently in Figs. 14(b) and 14(c), respectively, for a fixed laser excitation energy. Clearly visible in Fig. 14(b) are the two

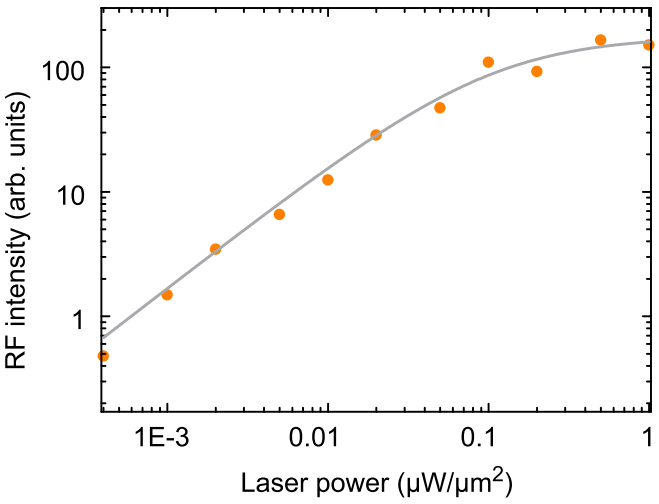

FIG. 13. Intensity of the resonance fluorescence as a function of the laser excitation power. The orange data point shows the resonance fluorescence counts of the quantum dot for the increasing laser power. The number of counts increases linearly until it saturates for an excitation power of more than 0.1 μW/μm^2. The solid line is a fit to the data, using Eq. (12) for the average occupation probability of the upper level in equilibrium.

resonances that are the two bright exciton transitions, separated by the fine-structure splitting.[131,222–224] The single resonance in Fig. 14 corresponds to the trion transition. The fine-structure splitting can be tuned by piezoelectric-induced biaxial stress to zero to obtain entangled photon pairs,[225,226] another important ingredient for quantum information technologies, for instance, in quantum repeaters in a visionary quantum internet (see Wehner *et al.*[227] and references therein).

V. TIME-RESOLVED ELECTRICAL TRANSCONDUCTANCE SPECTROSCOPY

Section V will review the recent progress on time-resolved (non-equilibrium) transconductance spectroscopy on an ensemble of dots. The InAs/GaAs quantum dots are embedded in a high-mobility electron transistor structure (as shown in Fig. 5). A two-dimensional electron gas (2DEG) is used, on the one hand, as a charge reservoir for electrons that can tunnel through a tunneling barrier into the dot states. On the other hand, the 2DEG is a very sensitive charge detector. The measurement techniques of a conduction channel (the 2DEG here) has lots of similarities with the readout process in a Flash memory.[228] The quantum dots are the storage unit, and the electron gas is the readout channel in a quantum dot memory device.[13,229–231]

A. Experimental method

To understand the measurement principle of the time-resolved electrical transconductance spectroscopy, I would like to

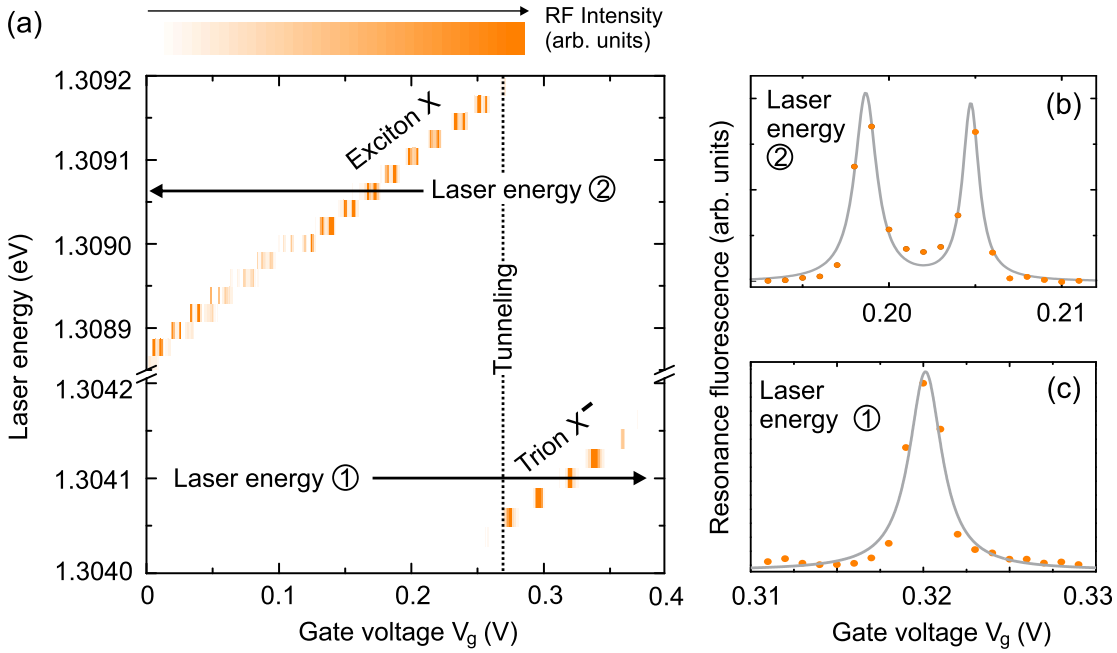

FIG. 14. Resonance fluorescence (RF) of a single self-assembled InAs/GaAs quantum dot. (a) A two-dimensional RF scan of an exciton (X) and trion (X^-) transition for different excitation laser energies and gate voltages. The exciton transition is shifted to higher energy as the gate voltage is increased from $V_g = 0$ V up to 0.26 V. At a gate voltage of $V_g = 0.26$ V, an electron can tunnel into the dot from the reservoir. The fluorescence signal of the exciton is quenched, and the trion transition can be observed at lower energies between $V_g = 0.26$ V and 0.36 V. (b) A line-cut at a constant energy of 1.3096 eV for the exciton transition with its fine-structure splitting. (c) A line-cut at a constant energy of 1.3041 eV which shows the trion transition.

add first some remarks to the capacitance-voltage spectroscopy (C-V), already explained in Sec. III B. This should help us to understand the ingredients of time-resolved measurements on nonequilibrium dynamics.

In the "C-V spectroscopy," the applied gate voltage V_g sets the Fermi energy in the back contact with respect to the confined states in the quantum dots (cf. Fig. 8). Starting at high negative gate voltages ($V_g < -0.9$ V), the quantum dots are completely empty. Increasing the gate voltage successively fills the dots with electrons until they are completely charged with six electrons at $V_g = 0.3$ V. In this sense, the static gate voltage defines the initial charge state of the dots. In the C-V measurement, this static gate voltage is superimposed by a small ac voltage (~5–10 mV) that is the "excitation source." It excites the system "quantum dot–charge reservoir" slightly into a nonequilibrium situation, so that the electrons tunnel into and out of the quantum dots to reach the equilibrium condition again. The ac tunnel current (plus phase) between the dot and the reservoir is finally measured as a capacitance signal. To summarize, for a dynamical measurement, we need the following: (i) an initial state preparation, (ii) excitation to drive the system into a nonequilibrium situation, and (iii) time-resolved detection of the signal (capacitance in the C-V spectroscopy).

In the same manner, we can now understand the time-resolved electrical transconductance spectroscopy, which I will explain in more detail by using Fig. 15. An initial gate voltage V_{ini} is applied between drain and gate contacts [red line in Fig. 15(a)], which sets the initial equilibrium occupation of the quantum dots with electrons [step (i)]. As an example, displayed in Fig. 15(b), the dots are completely empty for a certain high negative gate voltage V_{ini}, as the Fermi energy E_F in the reservoir is below the lowest level in the dots. Increasing this initial gate V_{ini} voltage will increase the initial average occupation with electrons.

Besides the average occupation with electrons in the dots, the gate voltage determines the charge carrier density in the two-dimensional electron gas n_{2D}, see Fig. 15(b). The electron gas is depleted for the initial (negative) gate voltage V_g, and hence, the conductance $G(t) \propto \sigma = e\, n_{2D}(t)\mu(n)$ is reduced [orange line of the source-drain current I_{sd} in Fig. 15(a)]. The relation between conductance G_{2D} and conductivity σ in 2D is given by the aspect

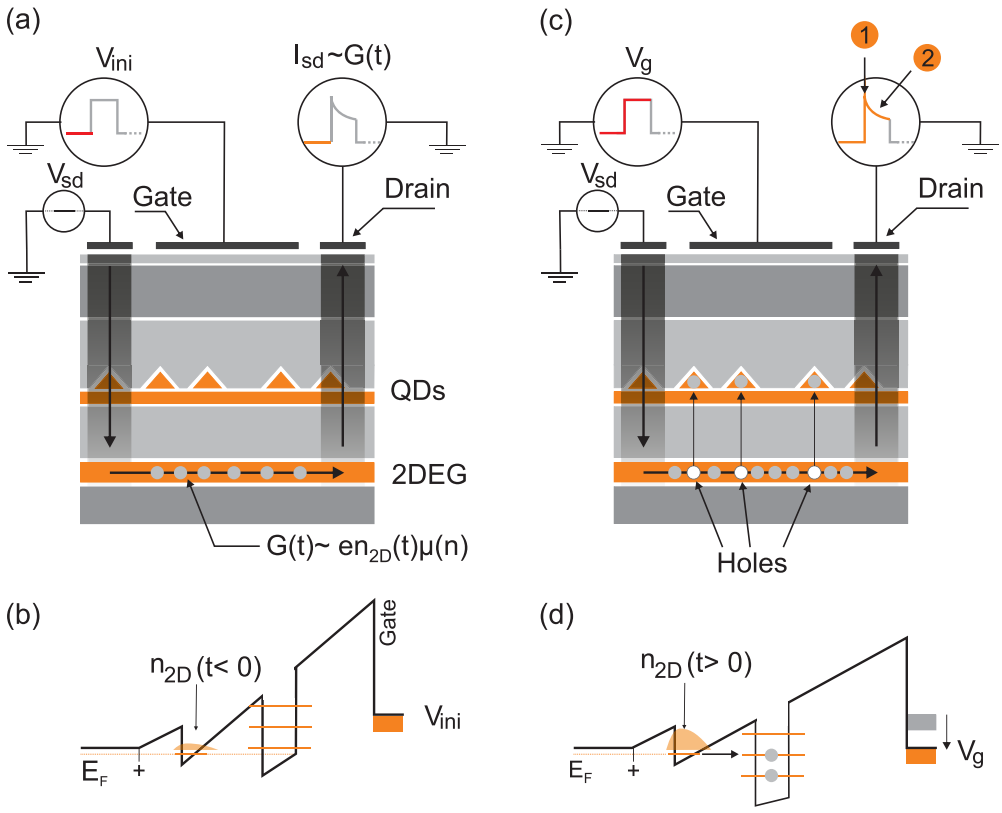

FIG. 15. Schematic principle of the time-resolved transconductance measurement. (a) An applied source-drain voltage V_{sd} gives a certain source-drain current I_{sd} that is directly related to the conductance $G(t)$ of the two-dimensional electron gas (2DEG). (b) Schematic band structure for an initial gate voltage V_{ini}, where the quantum dots are completely empty before the gate pulse V_g. The electron density n_{2D} is reduced in the 2DEG before the gate pulse is applied ($t < 0$). (c) At $t = 0$, the gate pulse is applied so that the Fermi level is shifted higher in energy with respect to the quantum dot states. The response of the conductance $G(t)$ of the 2DEG is ① a fast increase in the conductance due to charging of the 2DEG and ② a slower transient, which is due to the tunneling of electrons into the dot states (cf. Fig. 16). These "missing electrons" are labeled as holes. (d) Schematic band structure after the applied gate pulse V_g at $t > 0$. The electron density in the 2DEG is increased, and the tunneling of electrons into the quantum dot states takes place.

ratio of the length l to width w of the two-dimensional channel: $\sigma = G_{2D}\frac{l}{w}$. This relation can be easily understood by comparison to the 3D case: In three dimensions, the conductivity (as an universal material property) can be derived from the absolute (measured) value of the conductance, multiplied by the length l and divided by the cross-section A of a wire: $\sigma = G_{3D}\frac{l}{A}$. In 2D, the cross section is just a width w, giving the formula for the 2D case.

Now follows step (ii): The excitation into a nonequilibrium situation by an applied gate pulse V_g [upper red line in Fig. 15(c)]. The reaction of the system is twofold: ①: On a time scale of the RC time constant of the device, the two-dimensional electron gas will be filled with electrons, visible as a sharp increase in the source-drain current [or conductance $G(t)$] at point ① in Fig. 15(c). ②: Electrons tunnel through the tunneling barrier into the quantum dots on a longer time scale, leaving "missing electrons" (holes) in the two-dimensional electron gas.

In a very simplified picture, the holes in the 2DEG reduce the conductance $G(t)$ by reducing the charge carrier density n_{2D}. However, I have to explain this effect a little bit more precisely in terms of "How is the conductance in the 2DEG changed by electrons stored in the quantum dots?" Electrons that tunnel through the tunneling barrier reduce the conductance in the electron gas in principle in two ways: First, a charged layer of dots depletes a proportional number of electrons in the 2DEG, given by a relation to the lever arm L [see Eq. (1)].[96] In this sense, the missing electrons (called holes before) are actually given by an depletion of the 2DEG by the charged quantum dots. On the other hand, the conductance G is determined by its conductivity σ, which is given by the charge carrier density "as well as" its mobility: $G \propto \sigma = en_{2D}\mu(n)$. However, detailed investigations have shown that the influence of the charge dots as Coulomb scatters can be neglected,[90,232] and the charge carrier mobility $\mu(n)$ changes mainly by the depletion of the electron gas.

This allows us to assume that the conductance change ΔG is mainly proportional to the number of charge carriers Δn_{QD} transferred into the quantum dots

$$\Delta G \propto \Delta n_{QD}. \tag{13}$$

For small excitation voltages ΔV_g, the density of states $D(E)$ can be derived from the total change in conductivity $\Delta\sigma$ (with $\Delta\sigma \propto \Delta G$)

$$\frac{\Delta\sigma}{\Delta V_g} = \frac{\Delta n_{2D} e\mu}{\frac{\Delta E}{e\lambda}} = \lambda e^2 \mu \frac{\Delta n_{QD}}{\Delta E} = \lambda e^2 \mu D(E). \tag{14}$$

The change in conductance ΔG can be easily measured by a change in the current I_{sd} using a current amplifier for a constant applied voltage between the source and the drain contact (cf. Fig. 15). These transconductance measurements are carried out in a liquid helium bath cryostat at $T = 4.2$ K for a constant source-drain voltage of typically $V_{sd} \approx 10$ mV. The measurement is triggered by a function generator that sets the gate voltage V_g with respect to the source contact.

A typical measurement of a conductance transient $G(t)$—that is directly related to the electron tunneling into the dot states—is shown in Fig. 16. After the abrupt change in the gate voltage at t = 0, the fast increase in the conductance ($t_{2D} \approx \mu$s) at point ① is visible. This fast increase in the charge carrier density in the electron gas is limited by the RC time constant, given by the RC characteristics of the device and the experimental setup. Here, the response time of the electron gas is on the order of $t_{2D} \approx 1$ μs. The RC constant has to be significantly faster than the tunneling time because this difference in time constants enables us to evaluate the charging of the quantum dots independently from the charging of the 2DEG.

After this short RC time constant, the dot states are in a nonequilibrium situation with the electrons in the 2DEG. As a consequence, tunneling of electrons into the dot states decreases the conductance on a time scale of the average electron tunneling time [point ② in Figs. 15(c) and 16], on the order of a few milliseconds in Fig. 16. The change in conductance $\Delta G(t) = G_0 - G(t)$ is proportional to the number of transferred electrons n_{QD}.

B. Near-equilibrium measurements

After the introduction of the measurement principle to obtain a transconductance transient, the next step is to explain the procedure to derive a spectrum from these transients of the electron dynamics. This time-resolved transconductance spectroscopy can be divided into two different measurement schemes: the "near-equilibrium measurements," explained in Secs. V B and V C and the "nonequilibrium measurements," described in Sec. V D later on.

In the near-equilibrium measurements, a set of transients for different gate voltages and "fixed small pulse amplitude" ΔV probe the electrical density of states (DOS) of the many-particle ground states in a near-equilibrium situation. The wording "near-equilibrium" can be understood in the sense that the system "dot-2DEG" is only slightly driven out of equilibrium by the small additional voltage pulse amplitude ΔV. The observed transient is the relaxation process into equilibrium again by electron tunneling into (or out of) the quantum dot states. The electron system "inside" the dots is always in equilibrium during this measurement scheme.

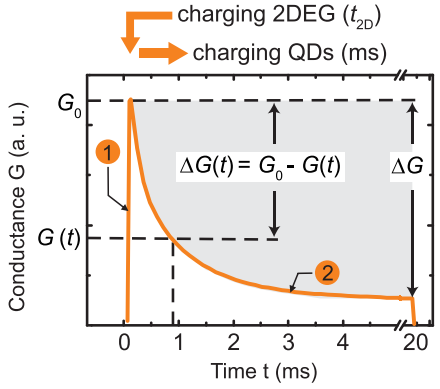

FIG. 16. Time-resolved transconductance measurement of the electron tunneling. At t = 0, the gate pulse is applied and the conductance G of the 2DEG is measured. The response of the conductance $G(t)$ of the 2DEG is ① the fast increase in the conductance due to charging of the 2DEG (here: rise time $t_{2D} \approx \mu$s) and ② a slower transient (here: $t_{QD} \approx$ ms), which is due to the tunneling of electrons into the dot states, as described before in Fig. 15. Adapted with permission from Beckel *et al.*, Phys. Rev. B **89**, 155430 (2014). Copyright 2014 the American Physical Society.[233]

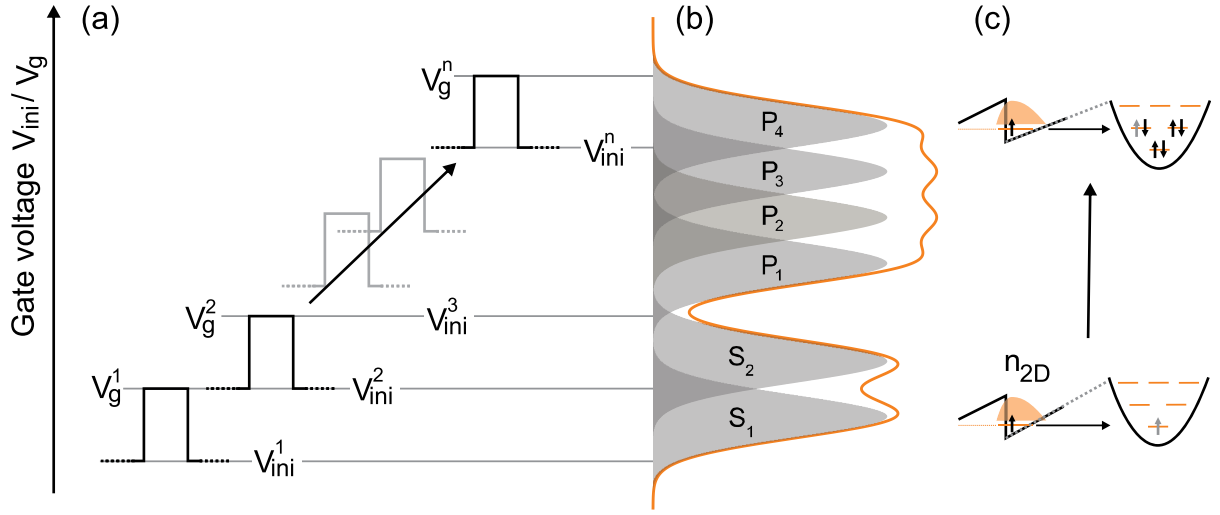

FIG. 17. Operation principle for the near-equilibrium transconductance spectrum. (a) The initial gate voltage V^n_{ini} sets the initial charge state of the quantum dots from $n = 0 \ldots 6$ electrons. The pulse voltage V^2_g is slightly higher to charge/uncharge the quantum dots with just one electron. (b) Schematic picture of the density of states in an ensemble of self-assembled dots and (c) electron tunneling process into different many-particle ground states.

This set of transients is obtained by a pulse scheme that is explained by the schematic representation in Fig. 17. The spectrum starts with an initial gate voltage V^1_{ini} [see Fig. 17(a)], where the quantum dots are uncharged, i.e., the Fermi level in the 2DEG is well below the s-shell of the dots [Figs. 17(b) and 17(c)]. As mentioned, this initial gate voltage sets in the following the initial charge state. Now follows the excitation into a slightly nonequilibrium situation by an applied gate pulse V^1_g. The Fermi level in the 2DEG is now above the s_1-states in the dots, and electrons can tunnel into the s-shells of the quantum dots [Fig. 17(c)], reducing the conductance of the 2DEG.

The pulse amplitude $\Delta V = V^1_g - V^1_{ini}$ should be smaller than the energy spacing between different charge states $n = 1.6$. This ensures that only one electron per QD is charged or discharged, and moreover, the QD itself is not in a nonequilibrium situation where, for instance, an electron is charged into the p-shell without occupation of the s-shell. Decreasing the pulse amplitude ΔV means also for an ensemble of millions of quantum dots that a smaller fraction of dots are charged with an additional electron for a certain gate pulse V^1_g. The next fraction of smaller-sized dots with higher energy of the s_1-state will be charge for the next gate pulse between V^2_{ini} and V^2_g.

Finally, after the pulse at V^1_g and simultaneously recording the charging transient $G(t)$, the gate voltage is set back to V^1_{ini} and the electrons tunnel back into the 2DEG again. The complete set of transients is obtained by setting step-like the next initial gate voltage V^2_{ini} to the previous pulse voltage V^1_g [see Fig. 17(a)], charging the QDs initially from zero up to six electrons [Fig. 17(c)]. The spectrum is obtained by plotting the amplitude in the conductance change (ΔG in Fig. 16) as a function of the gate voltage V_g.

Figure 18 shows such a near-equilibrium spectrum for $\Delta V = 40$ mV. The gate voltage is increased from $V_g = -1$ V (empty quantum dots) up to 0.5 V (completely filled quantum dots). The y-axis shows the transient amplitude $\Delta G(t = 20)$ ms for a situation, where the dot-2DEG system has reached equilibrium (it is the difference in conductance ΔG between t = 0 and 20 ms in Fig. 16). It corresponds directly to the density of states in equilibrium.

The dot density of the sample is about $8.3 \times 10^9\,\mathrm{cm}^{-2}$, determined by atomic force microscopy studies of similarly grown dots on the sample surface. The gated area is $1.3 \times 10^5\ \mu\mathrm{m}^2$, which leads to a large ensemble of 1×10^7 probed dots. The inhomogeneous ensemble broadening is about 10 meV. The direct Coulomb interaction E^C_{ss} between the two electrons in the s-shell can be obtained by the lever-arm $\lambda = 7$ and the voltage separation between the two s-states: $E^C_{ss} = 20$ meV. For the s-states in Fig. 18, this is sufficient to resolve clearly two distinct peaks. However, the repulsive Coulomb interaction

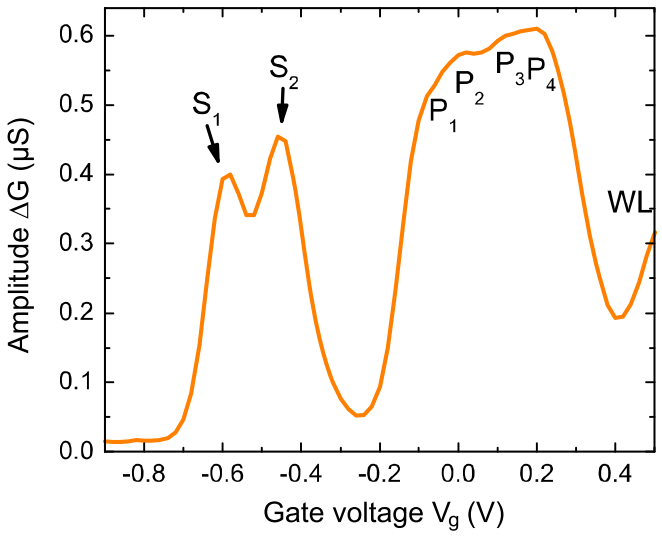

FIG. 18. Near-equilibrium transconductance spectrum. The amplitude of the change in conductance ΔG vs the applied gate voltage V_g. Six individual peaks of the charging of the two-dimensional harmonic oscillator are visible from electron tunneling into the many-particle ground states. Reproduced with permission from Appl. Phys. Lett. **95**, 022113 (2009)]. Copyright 2009 AIP Publishing.[234]

in the p-shell for a two-dimensional harmonic oscillator is smaller $E^C_{p1p2} = E^C_{p3p4} \frac{1}{2} E^C_{ss} = 10\,\text{meV}$ and $E^C_{p3p3} = \frac{7}{8} E^C_{ss} = 17.5\,\text{meV}$ (see Warburton *et al.*[85] for a simple model calculation). Therefore, the ensemble broadening is too large to resolve clearly the p-states separately. Only a small dip can be seen between the p_2 and p_3 states in Fig. 18, due to the larger Coulomb interaction between these two states.

Coming back to the comparison with the capacitance voltage spectroscopy (C-V): As mentioned in the motivation for every time-resolved nonequilibrium dynamics measurement, this near-equilibrium transport measurement acts like "time-resolved capacitance spectroscopy," where the amplitude of the transient corresponds to the absolute value of the current and the time constant is related to the phase shift between the applied voltage and the current in an ac capacitance measurement.[51] A comparison with the capacitance-voltage measurement in Fig. 8 shows these similarities; however, the transport spectroscopy in Fig. 18 has a much higher resolution for a weakly coupled dot-2DEG system, which will be demonstrated in the following.

C. Weakly coupled hole states

Weakly coupled means that the tunneling rate is very small, and the relaxation rate into equilibrium exceed seconds, still giving a high-resolution spectrum of the equilibrium ground states. This will be shown here for hole states in InAs/GaAs quantum dots that exhibit the same level structure with s-, p-, and d-shells.

Figure 19 shows two conductance transients for one fixed offset gate voltage V_g and a pulse height of $\Delta V = 50\,\text{meV}$. At $t = 0$, a positive voltage step with ΔV lifts the Fermi level in the two-dimensional hole gas above the confined hole states. The holes tunnel out of the quantum dot states into the hole gas, schematically displayed in the upper-left inset in Fig. 19. A transient with increasing conductance and amplitude ΔG is visible. Due to a thick tunneling barrier (see Nowozin *et al.*[231,235] for more details on the sample structure), the tunneling time is above 10 s, five orders of magnitude longer than observed before for the electron tunneling in Fig. 16. Vice versa, a more negative voltage is applied at $t = 60$ s, and the holes can tunnel from the hole gas back into the dot states again (lower right inset in Fig. 19). A transient with decreasing conductance is measured between $t = 60$ and 120 s.

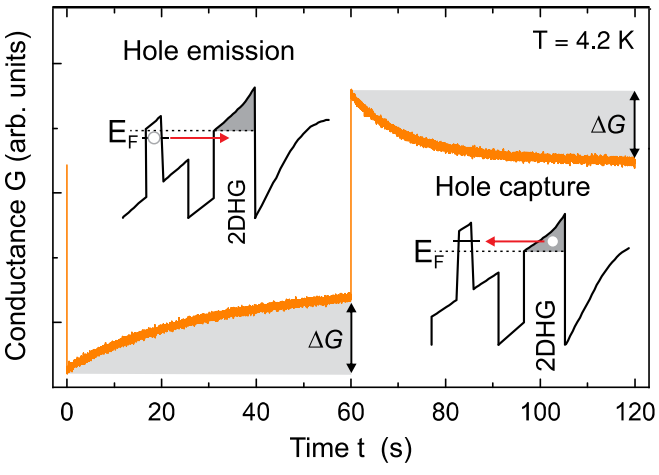

FIG. 19. Time-resolved conductance measurement of hole tunneling into InAs quantum dots. For a positive voltage step of $\Delta V = 50\,\text{meV}$ at $t = 0$, the Fermi level in the two-dimensional hole gas (2DHG) is lifted up and holes can tunnel from the dots into the 2DHG (see the schematic inset in the upper left corner). A transient with increasing conductance and amplitude ΔG is visible. Vice versa, at $t = 60$ s, a more negative voltage is applied and the holes tunnel from the 2DEG into the dot states (lower right inset) while a decreasing conductance transient is measured.

The transients in Fig. 19 display the emission of holes from and the capture into the states of the quantum dot ensemble. The amplitudes of the transients are directly related to the number of holes that are transferred during each voltage pulse. Plotting the amplitudes of the conductance change ΔG vs the gate voltage V_g (it is a DC offset bias) at which the transient was measured, a structure similar to the one observed in the C-V measurements in Fig. 8 is visible in Fig. 20. At a temperature of 4.2 K, the dominant emission and capture process for the holes is pure tunneling through the barrier, and clearly distinct maxima for hole charging into the s_1- to the p_4-state are visible. The better resolution in comparison to the electron spectrum in Fig. 18 has two reasons: (i) the inhomogeneous broadening is slightly reduced to 9 meV in this hole sample (see Nowozin *et al.*[231]). (ii) Measurements and calculations using the 8-band-$k{\cdot}p$-model[231] show a stronger hole repulsion energy in the p-shell due to Coulomb interaction (~15 meV), giving a larger separation energy in the spectrum. Even for a smaller quantization energy of the hole states between the s- and p-shells (about 20 meV), the spectrum shows as a consequence of the stronger Coulomb repulsion clearly visible peaks in Fig. 20.

When the temperature is increased above 4.2 K, the peaks become less distinct, and they vanish completely above 70 K. For increasing temperature, thermally assisted tunneling is the dominating process, where the holes are thermally activated to a higher state and then tunnel through the barrier.[12,236]

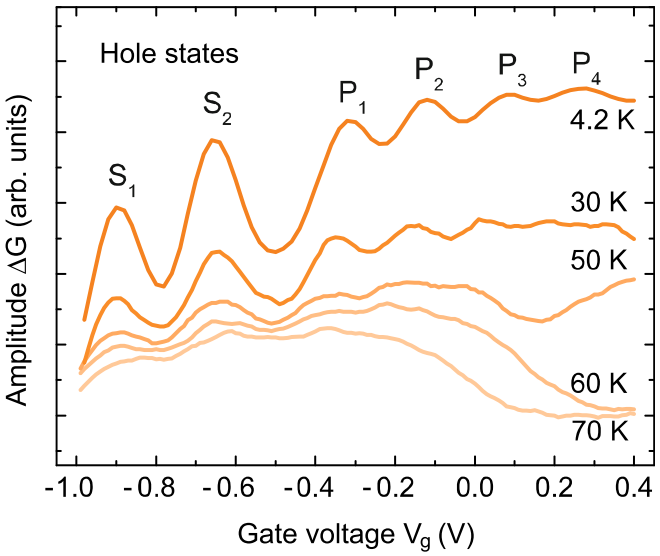

FIG. 20. Near-equilibrium transconductance spectrum of the hole states. The change in conductance ΔG for hole tunneling into the dot states vs the applied offset gate voltage V_g. For increasing temperature, the visibility of the six charging peaks decreases; however, the s-shell is still visible up to 70 K. Adapted with permission from Nowozin *et al.*, Phys. Rev. B **84**, 075309 (2011). Copyright 2011 the American Physical Society.[231]

D. Nonequilibrium quantum dot states

In the previous measurements, the quantum dots themselves were always in an equilibrium situation, and the many-particle ground states for an occupation with 1…6 electrons (or holes) were observed in the transconductance spectrum. However, for the visionary application of quantum computation, accessing the excited states—that form with a ground state a quantum bit (Qubit)—is the first ingredient. Moreover, the coherent superposition of both states and the coupling of different qubits are further challenges. It will be shown in the following Secs. V D and V E that the time-resolved transconductance spectroscopy enables us to access the nonequilibrium excited states in an all-electrical measurement scheme.

All we have to do is to change the pulse sequence slightly to prepare these nonequilibrium states inside the quantum dots and observe their relaxation dynamics into equilibrium. The new pulse sequence for the nonequilibrium measurements is schematically demonstrated in Fig. 21. The initial gate voltage V^n_{ini} controls again the number of electrons loaded initially into the quantum dots (from zero up to six electrons). However, in this nonequilibrium measurement, it is fixed at a constant value for the entire measurement: $V^1_{ini} = V^2_{ini} = \ldots = V^n_{ini}$. It follows again the pulse bias V^n_g, as depicted in Fig. 21(a). As the initial gate voltage is fixed in the nonequilibrium measurement, the pulse amplitude $\Delta V^n = V^n_g - V^n_{ini}$ increases. Note this difference between the near-equilibrium pulse sequence and spectrum in Sec. V B and the nonequilibrium measurements here. In the "nonequilibrium" measurement, the initialization gate voltage V^n_{ini} is fixed, while the gate pulse V^n_g is increased in steps. The pulse amplitude ΔV changes during the measurement. In the near-equilibrium measurement, however, the initial gate voltage is changed, while the pulse amplitude is fixed.

Increasing the amplitude of the pulse ΔV leads to a situation, where more and more QD states are accessible for electron tunneling from the 2DEG. This is schematically demonstrated in Fig. 21, where, for instance, the pulse bias V^n_g in Fig. 21(a) fills all states in the p-shell [shown in Fig. 21(b)]. The overall amplitude of the conductance transient $G(t)$ will increase for increasing pulse amplitude [see Fig. 21(c)], and hence, $\Delta G(t)$ is a step-like function, as schematically illustrated by the black line in Fig. 21(d). Steps in the conductance amplitude $\Delta G(t)$ always appears for pulse voltages V_g, where another dot state is available for electron tunneling. The density of states (the nonequilibrium spectrum) can be obtained by taking the first derivative of the conductance change $\Delta G(t)$ with respect to the gate voltage V_g, as derived in Eq. (14) and schematically depicted by the orange line in Fig. 21(d). Taking the amplitude of the transients $G(t)$ at a time much larger than the electron tunneling time yields the same equilibrium spectrum as before in the near-equilibrium spectrum. This means that the equilibrium spectrum of the quantum dot states is obtained in a nonequilibrium measurement. Much more important is the fact that the reduction of the evaluation time t in $\Delta G(t)$ (using the amplitude of the conductance change $\Delta G(t)$ at shorter time scales) allows us to access spectra of nonequilibrium situations in the quantum dots; this will be discussed later in this section.

I will now come to the measurement: Starting first from an initial gate voltage $V_{ini} = -0.8$ V, where the quantum dot ensemble is empty [see the schematic picture in Fig. 22(a), left]. The conductance change $\Delta G(t)$ reflects again the average electron occupation number $n(t)$ of the quantum dots. Figure 22 shows this change in conductance $\Delta G(t)$ for four different charging times from a nonequilibrium situation at 0.02 ms up to the equilibrium situation at 20 ms as a function of the applied gate pulse V_g. The schematic pictures in Fig. 22(a) display how the average number of electrons in equilibrium n_{eq} increases by increasing the gate pulse voltage V_g up to 0.3 V [upper figure in Fig. 22(c)]. For every gate voltage V_g, the conductance change increases

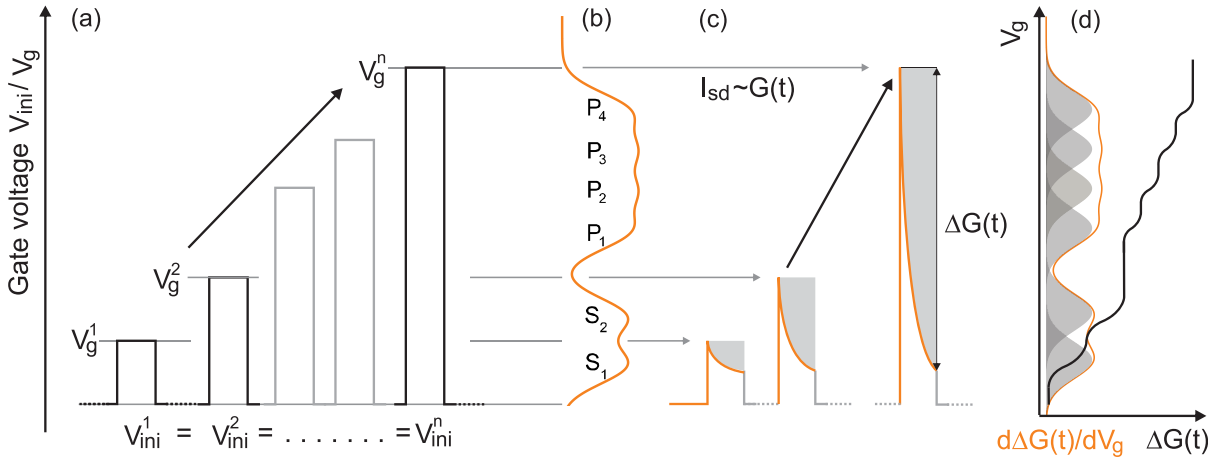

FIG. 21. Schematic illustration of the operation principle for a nonequilibrium transconductance spectrum. (a) The pulse sequence starts with an initialization voltage $V^1_{ini} = V^2_{ini} = \ldots V^n_{ini}$ that is fixed at the same value for the entire spectrum. It controls the initial electron occupation before the gate pulse V^n_g is applied. The pulse voltage V^n_g is then step-like increased, starting from the s_1- up to the p_4-state [as shown in (b)]. (c) Schematic representation of the conductance transients, where the amplitude ΔG increases with the increasing number of electrons that are transferred between the 2DEG and the QDs. (d) The black solid line shows the amplitude of the conductance change vs applied pulse voltage V_g, showing a step-like increase for every additional charged QD state. The first derivative of the conductance vs pulse voltage $d\Delta G(t)/dV_g$ yields the nonequilibrium spectrum.

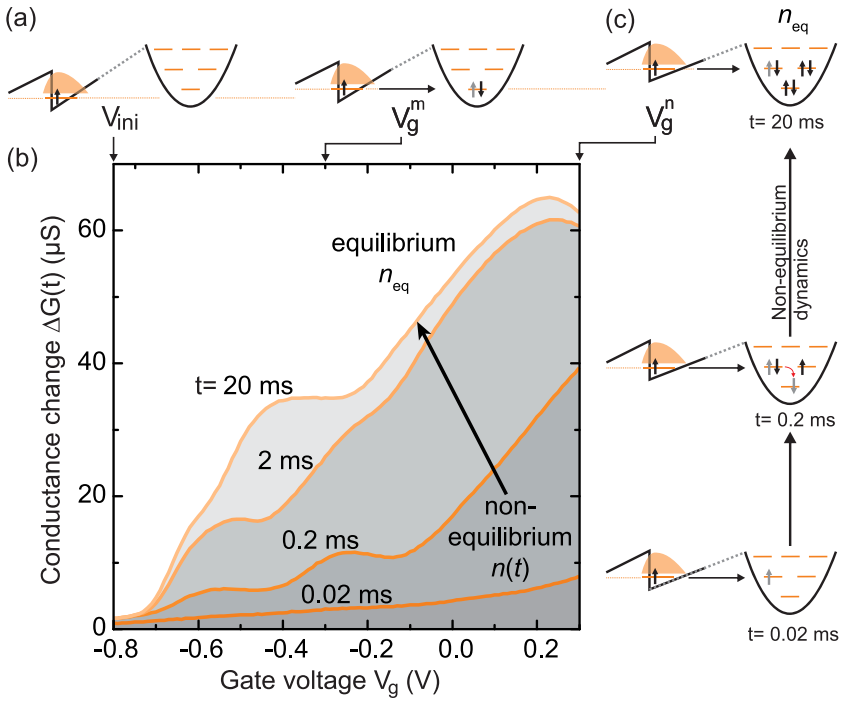

FIG. 22. Time evolution of the change in the conductance $\Delta G(t) \sim n(t)$ as a function of the pulse voltage V_g. (a) Schematic representation of the final equilibrium charge state n_{eq} in the quantum dots for different gate (pulse) voltages. (b) Conductance change $\Delta G(t)$ vs pulse voltage V_g for different charging times t. The equilibrium situation is reached after 20 ms, where pronounced steps in the conductance at different gate voltages are related to the tunneling into different many-particle ground states. (c) Schematic pictures for the charge state $n(t)$ for increasing charging time t from 0.02 ms up to 20 ms, for a fixed gate (pulse) voltage V_g.

with increasing time from $t = 0.02$ ms up to $t = 20$ ms since more and more electrons are transferred.

At $t = 20$ ms, the previously discussed shell structure is already visible in Fig. 22 as pronounced steps in $\Delta G(t)$ vs V_g. At the shortest time of $t = 0.02$ ms, only one electron per dot has tunneled. This gives the possibility to populate an excited state in the p-shell [depicted for $t = 0.02$ ms in Fig. 22(c), bottom] or d-shell, where no electrons have tunneled into the s-shell. For intermediate times as $t = 0.2$ ms, electrons form complex exited state configurations, where relaxation inside the dots and further tunneling drive the system into equilibrium at $t = 20$ ms.

Figure 23(a) shows now this first derivative $d\Delta G/dV_g$ (the density of states) as a function of the gate voltage and the transient time t for a measurement that starts at 0.5 ms after the gate pulse. The initial gate voltage was set to $V_{ini} = -0.9$ V, where the quantum dots were completely empty. The data show the evolution of the density of states, as the dots are subsequently filled with up to six electrons by tunneling from the charge reservoir.

Let us start with the discussion of this spectrum at the short delay time of $t = 0.5$ ms after the gate pulse, displayed in Fig. 23(b). The tunneling time into the s-shell is on the order of $\tau_s = 6$ ms (and $\tau_p = 1.4$ ms into the p-shell), so that in good approximation only tunneling into the empty dots is observed. This nonequilibrium spectrum shows three distinct peaks with an almost equal energy spacing of ~52 meV, where one electron tunnels into the s-, p-, or d-shell [see Fig. 23(b)]. It is a single-particle spectrum of a two-dimensional harmonic oscillator (with the characteristic equidistant level spacing) with the nonequilibrium states p^* and d^* of the p- and d-shells, respectively. It is a "quantum-dot hydrogen spectrum" of an artificial atom in a semiconductor. Note here that the orange solid lines in the nonequilibrium spectra are only connections between the data points (open circles) for different applied gate voltages V_g.

In the opposite limit—long charging time in comparison to the average tunneling time $t > t_s, t_p$—the signal reflects the spectrum under the equilibrium condition in Fig. 23(c). For the delay time shown here ($t = 10$ ms), again two maxima are observed for one and two electrons inside the s-shell around $V_g = -0.6$ V, i.e., the s_1 and s_2 states, respectively. The spectrally broader structure between −0.2 and 0.2 V corresponds to the four charging peaks of the p-shell (cf. Fig. 8). The spectrum in equilibrium in Fig. 23(c) is a result of electron tunneling into the excited states with subsequent relaxation into the ground state and further electron tunneling from the reservoir. A more detailed discussion of the time-resolved evolution of the states from nonequilibrium into equilibrium can be found in Marquardt *et al.*[89] and Beckel *et al.*[237]

Changing the initialization gate voltage to $V_{ini} = -0.6$ V yields a singly charged dot with one electron in the s-shell at the beginning of the pulse sequence (schematically depicted by one electron in the s-shell for the initial state in the upper-left corner of Fig. 24). When already an electron is present, the second electron transferred during the gate pulse V_g will form a two-electron configuration and hence the excitation spectrum of artificial quantum dot helium (shown in Fig. 24). A new clear resonance can be found at $V_g = -0.53$ V, which can be identified as tunneling into the two-electron (singlet) ground state s_2, in agreement with the previous capacitance and near-equilibrium measurements.

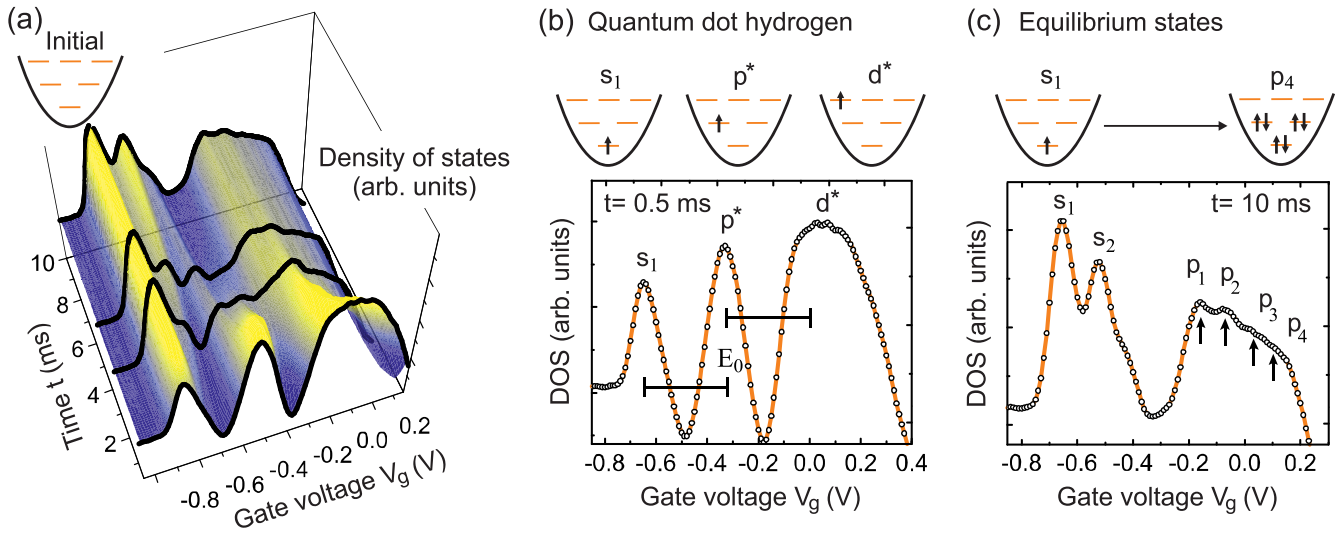

FIG. 23. Evolution of the density of states in a quantum dot ensemble from nonequilibrium to equilibrium. (a) Colored surface plot of the density of states—derived from $d\Delta G/dV_g$—as a function of time t and applied pulse voltage V_g. The initialization voltage at t = 0 was set to −0.9 V, so that the quantum dots are completely empty. (b) The nonequilibrium spectrum at $t = 0.5$ ms after the charging pulse exhibits three pronounced peaks with an almost equidistant energy spacing of ∼52 meV. It is a nonequilibrium quantum dot hydrogen spectrum with the level spacing of a two-dimensional harmonic oscillator and the excited states p^* and d^* of the p- and d-shells, respectively. (c) At $t = 10$ ms, the system is in the equilibrium situation, where the well-known charging peaks of the s- and p-shells for 1…6 electrons are observed. Reproduced with permission from Marquardt *et al.* Nat. Commun. **2**, 209 (2011). Copyright 2011 Springer Nature.

Except from the s_2-state, the spectrum has completely changed in comparison to the QD hydrogen spectrum. A double-peak structure can now be observed (at $V_g = -0.26$ V and -0.2 V) and attributed by comparison with theoretical calculations[89] as tunneling into the nonequilibrium (excited) two-electron singlet s_p^* and triplet t_p^* states. The energy difference of about 10 meV is a direct measurement of the exchange interaction energy in self-assembled quantum dots, which has been studied in complementary experiments using photoluminescence measurements.[83,238] From a deconvolution of the double-peak structure, it can be estimated that on the low-energy side of the resonance $V_g = 0.31$ V, about 99% of those dots will be prepared in the triplet state. The broad resonance above a gate voltage of $V_g = 0$ V can be attributed by comparison with the theory to closely lying states with contributions of single-particle states in the d-shell.

E. Spin-to charge conversion

Unfortunately, the spectral resolution in Fig. 24 is just sufficient to observe the singlet/triplet splitting of the p-shell; however, it is not sufficient to resolve the singlet and triplet states in the d-shell. In order to obtain a better energy resolution, a method in the time-resolved transconductance spectroscopy can be used which is known from transport measurements on lithographically defined dots: The spin-to-charge conversion[36,239] that translates the spin degree of freedom into different tunneling times for singlet and triplet states.

This "conversion principle" uses the fact that the decay times for the internal relaxation mechanism of the spin singlet s_p^* and triplet t_p^* states differ strongly in time. The excited p-state singlet can decay into the s_2 ground state by spin conservation, i.e., without a spin-flip of the electron. Different energy relaxation channels have been identified, and a lot of work has been published in this area to understand the relaxation process in self-assembled quantum dots (see, for instance, Refs. 240 and 241). The main contributions for the energy relaxation are Coulomb interaction (electron-electron scattering in an Auger-type process[242]) and electron-phonon coupling or polarons,[240] i.e., strong carrier-phonon interaction. This energy relaxation from the excited spin singlet state into the singlet ground state is known to be very fast, on the order of picoseconds,[243] faster than the time resolution of the time-resolved transconductance measurements here.

The spin relaxation time T_1 from the excited triplet t_p^* down to the singlet ground state s_2 needs besides the energy relaxation a spin-flip. The spin-flip can be caused by different interactions, such as (i) electron-electron exchange,[23] (ii) electron-hole exchange,[245] (iii) the hyperfine interaction with the spin of the nuclear bath,[246] and (iv) spin–orbit coupling.[247] The spin-flip plus energy relaxation is much slower, with 25 μs in the following experiments even slower than the average tunneling time.[244]

For the experiments of the spin-to charge conversion in Sec. V E and the electron spin relaxation in the following Sec. V F, a sample structure with a thinner tunneling barrier is used.[244] The tunneling time from the reservoir into the QD states is now much faster on the order of a few 10 μs. The experiment itself works in the same manner as the nonequilibrium transconductance spectroscopy (see the operation principle again in Fig. 15) with an important difference: The discharging transients will be measured (in contrast to the charging transients before).

The experimental operation in detail is given as follows: (i) The initial gate voltage is set to $V_{ini} = -0.53$ V, so that the initial charge in the quantum dot layer is one electron per dot. (ii) A short charging pulse with a length of $t_c = 10$ μs is applied. This charging pulse fills a

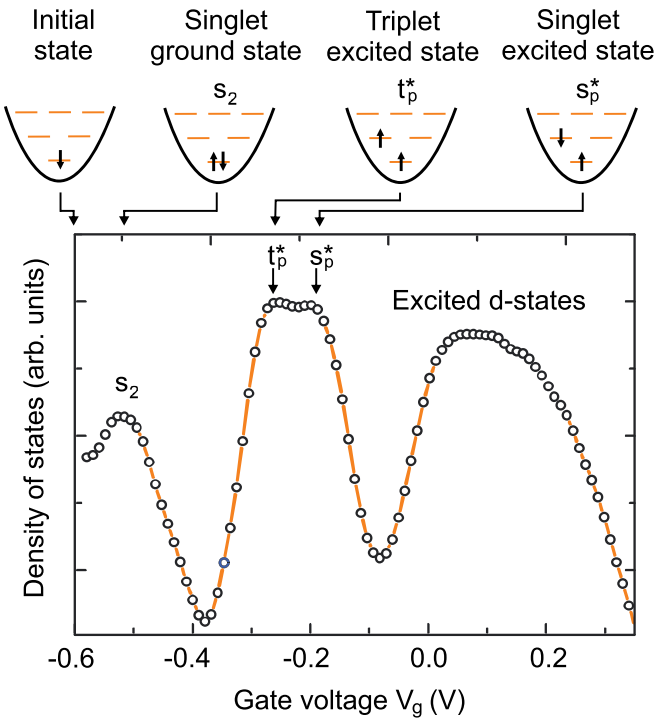

FIG. 24. Spectroscopy of excited states in quantum dot helium. The initial gate voltage V_{ini} is chosen so that already one electron is charged into the s_1-state in equilibrium (initial state in the upper-left corner). The lowest resonance observed at $V_g = -0.53$ V is due to tunneling into the two-electron ground-state s_2. Around -0.25 V, two resonances are visible which correspond to the tunneling of a second electron into the p-shell. The splitting is the exchange energy between the excited p-shell singlet s_p^* and triplet state t_p^*. Reproduced with permission from Marquardt *et al.*, Nat. Commun. **2**, 209 (2011). Copyright 2011 Springer Nature.

second electron into the quantum dots, giving an excited two-electron spin-singlet or -triplet state (depending on the pulse gate voltage). (iii) The gate voltage is set to the initial voltage V_{ini} again, and the discharging transient is recorded. Figure 25 shows a representative discharging transient at a gate voltage of $V_{ini} = -0.53$ V, where the spin-triplet state of the p-shell was initialized by the gate pulse.

As a consequence of different relaxation times of triplet and singlet states, the electrons that were injected into the p-shell exhibit two different time constants in the discharging transient, visible in Fig. 25. As the triplet state t_p^* has a longer relaxation time, the electrons in the p-shell will stay longer in the excited state and tunnel through an energetically smaller tunneling barrier into the 2DEG. The amplitude of the faster part of the transient in Fig. 25 is therefore directly related to the number of electrons in the excited p-shell triplet $n(t_p^*)$. The excited singlet state s_p^* will relax fast into the s_2 ground state, and hence, preparation of an excited singlet state shows a slower transient from the singlet ground state. This is the spin-to-charge conversion: The spin orientation in the excited state can be seen in the time constant of the discharging process, and the amplitude of the slower part of the transient is directly related to the number or electrons in the excited singlet state s_p^* (by the fast relaxation process $s_p^* \rightarrow s_2$).

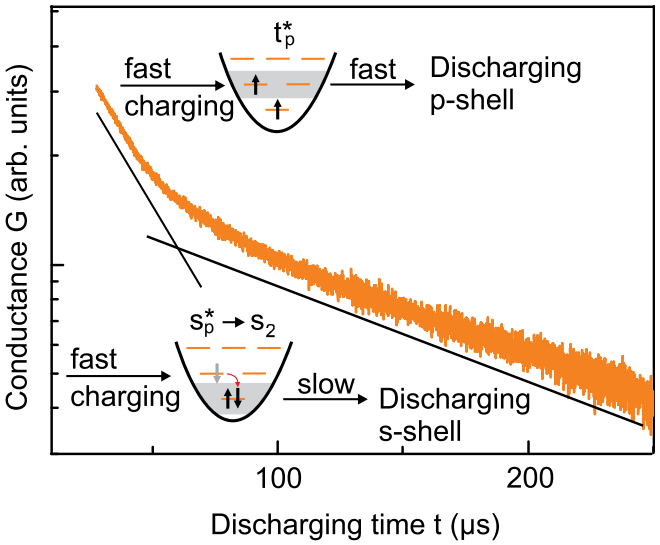

FIG. 25. Transient of the discharging process by tunneling of electrons back into the charge reservoir. The semilogarithmic plot shows a double-exponential decay that originates from electron tunneling from the s_2 ground and the t_p^* excited state. Reproduced with permission from Appl. Phys. Lett. **111**, 092103 (2017)]. Copyright 2017 AIP Publishing.

Fitting the transients for different gate (pulse) voltages V_g leads to these amplitudes for tunneling out of the p-state (fast process) and the s-state (slow process). Both of these amplitudes are plotted in orange (fast) and (slow) blue lines in Fig. 26, respectively. The triplet and singlet states of the p- and the d-shell can be clearly separated by their time constants, and the singlet-triplet spacing of about 13 meV agrees

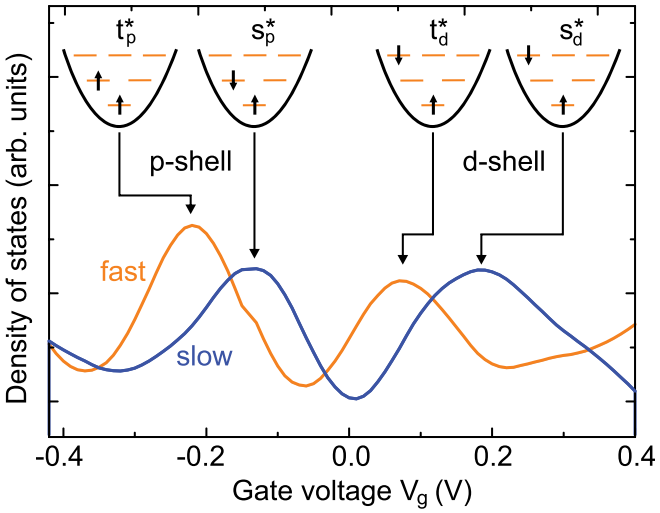

FIG. 26. Spectra for the singlet and triplet states in the p- and d-shells. Discharging amplitudes for the slow (blue) and fast (orange) contributions in Fig. 25 as a function of the pulse voltage V_g. Clearly visible are the singlet and triplet states of the p- and d-shells for slow and fast discharging times, respectively. Reproduced with permission from Appl. Phys. Lett. **111**, 092103 (2017). Copyright 2017 AIP Publishing.

perfectly with the exchange interaction in similar self-assembled quantum dots.[89]

F. Electron spin relaxation

The "spin-to-charge"-conversion technique can be used to determine in an all-electrical measurement scheme the spin-relaxation time of the two-electron excited spin-triplet state (t_p^* and t_d^*) into the singlet ground state s_2. For this, the pulse voltage is set so that the electrons are injected into the triplet state. A certain number of quantum dots are transferred by p-state charging from the s_1 ground state into the t_p^* excited state, cf. Fig. 26(b). The charging time t_c is stepwise increased from 8 μs up to 80 μs. Increasing the charging time increases the number of dots that are charged with electrons in the triplet state. At the same time, the possibility for a spin relaxation process rises, bringing these dots back into the singlet ground state s_2. The fraction of dots in the excited triplet state to the fraction of dots in the singlet ground state can be obtained by analyzing the discharging signal.

The amplitudes of the fast contribution A_{fast} in the discharging signal are given as blue data points in Fig. 27(a), whereas the orange dots depict the amplitude of the slow component A_{slow}. The amplitude of the fast discharging dominates strongly for short charging times t_c, indicating the filling of the excited triplet state t_p^* via tunneling from the back contact. As the charging time increases, the amplitude of the fast discharging component increases, on one hand, as more and more dots are populated with excited triplet states. On the other hand, the slow contribution [orange datapoints in Fig. 27(a)] increases as the electron in the p-shell relaxes down to the ground state s-shell. However, the spin relaxation of the t_p^*-state should lead to a decrease in the amplitude of the fast contribution A_{fast} for long charging times above 30 μs, while a saturation of the amplitude is observed in Fig. 27(a). This behavior can be explained by tunneling of a third electron into the dots after a spin relaxation process has occurred, filling up the p_1-state [see Fig. 27(b)]. The p_1-state filling leads to the same fast discharging signal as the excited spin triplet state.

A more quantitatively analysis can be done by a rate equation model of the population of the involved four states [$n(s_1), n(t_p^*)$, $n(s_2)$, and $n(p_1)$ in Fig. 27(b)]. Taking into account the sequence shown in Fig. 27(b), the following rate equations describe the situation:

$$\frac{dn(s_1)}{dt} = -\frac{n(s_1)}{\tau_p}, \tag{15}$$

$$\frac{dn(t_p^*)}{dt} = \frac{n(s_1)}{\tau_p} - \frac{n(t_p^*)}{\tau_{rel}}, \tag{16}$$

$$\frac{dn(s_2)}{dt} = \frac{n(t_p^*)}{\tau_{rel}} - \frac{n(s_2)}{\tau_p}, \tag{17}$$

$$\frac{dn(p_1)}{dt} = \frac{n(s_2)}{\tau_p}, \tag{18}$$

where τ_p is the characteristic time constant for electrons tunneling into the p-shell and τ_{rel} the spin relaxation time. The amplitudes of the fast and slow discharging components can be determined from $n(s_1)$ and $n(t_p^*) + n(p_1)$, respectively. Note here that only a fraction λ of quantum dots in the inhomogeneous ensemble is charged with a third electron for the applied charging voltage (see Eltrudis *et al.*[244] for more details).

The calculated discharging amplitudes are shown as blue and orange solid lines in Fig. 27(a) for the fitting parameters of $\tau_p = 14\,\mu$s, $\tau_{rel} = 25\,\mu$s, and $\lambda = 0.6$. The spin relaxation time is achieved for InAs quantum dots to the above-mentioned $\tau_{rel} = 25\,\mu$s without an applied external magnetic field at liquid helium temperature. Such spin-relaxation processes in zero-dimensional quantum dots have been intensively studied in a situation, where the energy separation of the two spin states is small (for instance achieved by a magnetic field in a Zeeman-split s-shell),[36,246,248–254] and spin relaxation times of up to 20 ms were found.[247] In lithography-defined dots in a two-dimensional electron gas, the s- to p-shell relaxation was studied, where the energy difference is in the order of 1–6 meV, and relaxation times of 200 μs up to 2.58 ms were found.[36,255]

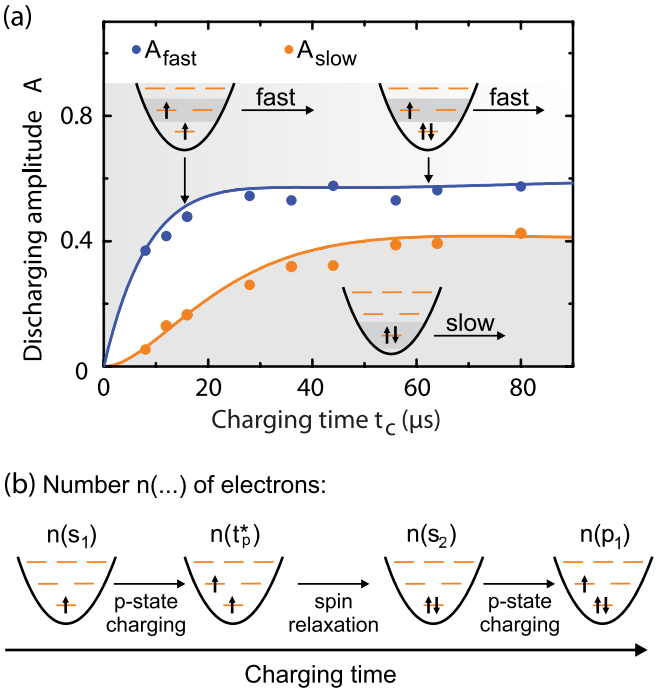

FIG. 27. Triplet-to-singlet spin relaxation. (a) The emission amplitudes are shown as a function of the charging time t_c. The amplitude of the fast component is given by the blue data points, while the slow component is given in orange. The solid blue and orange lines are fits to the data by a simple rate equation model. (b) Schematic illustration of the involved processes. Reproduced with permission from Appl. Phys. Lett. **111**, 092103 (2017). Copyright 2017 AIP Publishing.

G. Influence of the degeneracy on the relaxation times

We have until now neglected any degeneracy of the dot states that will influence the electron dynamics. However, the electron tunneling rate will increase by increasing the degeneracy of the final states, as more possible tunneling paths are available. This is a direct consequence of Fermi's Golden rule[256,257] $\gamma_{i\to f} = \frac{2\pi i}{\hbar}|\langle i|H'|f\rangle\rho_f$ for the transition rate from an initial state i to a final state f with the tunneling Hamiltonian H' and the final density of states ρ_f. The final

density of states (the degeneracy) increases the tunneling rate. I will discuss the influence of the degeneracy (or better: multiplicity as the number of possible transition paths from the initial to the final state) on the electron dynamics. I will show that the time-resolved transconductance measurements allow us to determine the degeneracy of the electronic p-shell by comparison of the experiments with a model based on a rate equation approach.

Moreover, the knowledge of the sequence of the degeneracy for filling the p-shell can answer the question, if this filling sequence of the many-particle ground states in a self-assembled quantum dot (as an "artificial atom") is equal to the orbital filling with electrons in an atom. In an atom, Hund's rules describe this filling sequence. For instance, the first rule states that the total spin quantum number in one shell should be maximized, i.e., all degenerated states in one shell should be populated first with parallel spins before a second antiparallel spin is added. From the observation of different charge relaxation times into equilibrium, a symmetry breaking together with a lifting of the degeneracy is observed and Hund's rule is not valid for a nondegenerated p-shell, as shown in the following (see also Beckel *at al.*[233] for more details).

Before going into the details of the degeneracy of the quantum dot states, I want to start with a very simple picture of the electron dynamics between the 2DEG (as charge reservoir) and the dot states. Figure 28 displays schematically the 2DEG with its average occupation with electrons, given by a Fermi-distribution function $f(E)$. The quantum dot is simplified with three states, having no degeneracy by angular momentum or spin. Assuming that the second state with energy E_2 is somehow aligned with the Fermi energy in the 2DEG, electrons can tunnel into and out of the quantum dot, as the Fermi distribution is not a step-like function for temperatures $T > 0$ K. The average occupation with electrons at the Fermi energy in the 2DEG is $f(E_F) = 0.5$ for $T > 0$ K; hence, after tunneling into the second level of the dot, an electron inside the dot with energy E_2 has again a certain probability to tunneling back into the 2DEG, as unoccupied states are available in the electron reservoir. It is a dynamic equilibrium of charging/uncharging the second dot level by tunneling [The first dot state with energy E_1 is always charged, as the Fermi distribution equals unity,

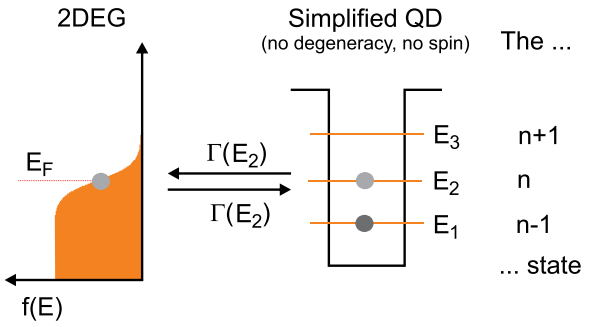

FIG. 28. Electron dynamics between a simplified quantum dot and an electron reservoir. The two-dimensional electron gas (2DEG) is schematically depicted with its average occupation with electrons vs energy, given by the Fermi-distribution $f(E)$. The simplified quantum dot has three electron states without degeneracy due to angular momentum or spin. The intrinsic transition rates $\Gamma(E_n)$ (rates without the influence of degeneracy and Fermi distribution) are equal for tunneling into and out of the dot, respectively.

while the third dot level is always uncharged for a Fermi distribution of $f(E_3) \approx 0$.].

The question is now, what is the average occupation of the second level with electrons, i.e., the probability p_2 of finding the dot in the 2-charge state (charged with two electrons)? The answer is, it is given by the rates of tunneling into and out of the dot, hence, by the following rate equations for p_2 and p_1:

$$\begin{aligned} \frac{dp_2}{dt} &= k_{1\to2}\Gamma(E_2)f(E_2)p_1 \\ &\quad -k_{2\to1}\Gamma(E_2)(1-f(E_2))p_2, \\ \frac{dp_1}{dt} &= -\frac{dp_2}{dt}, \end{aligned} \tag{19}$$

with probability of finding the dot in the 1-electron charge state as p_1. This set of two rate equations describes a simple situation as shown in Fig. 28, where the electron dynamics changes the charge state of the dot between singly and doubly charged (n = 1 and n = 2). Only the charging with one additional electron or discharging process of one electron plays a role. I use now the relations for the tunneling rates into the dot γ_n^+ and out of the dot γ_n^- (for the n-th charge state)

$$\begin{aligned} \gamma_n^+ &= \gamma_{n-1\to n} = k_{n-1\to n}\Gamma(E_n)f(E_n), \\ \gamma_n^- &= \gamma_{n\to n-1} = k_{n\to n-1}\Gamma(E_n)[1-f(E_n)]. \end{aligned} \tag{20}$$

The Fermi-distribution f accounts for the fact that the initial state in the two-dimensional electron gas can be occupied, or the final state in the 2DEG has to be unoccupied $[1-f(E_n)]$. The prefactor k accounts for the number of possible paths from the initial to the final state, in the present example of a simplified quantum dot in Fig. 28 with no (spin-)degeneracy $k_{1\to2} = k_{2\to1} = 1$.

For a more realistic dot with degenerated states, the prefactor k differs for transitions between different charge states. Figure 29 shows the possible configurations for a quantum dot charged with $n = 0\ldots4$ electrons. A configuration is a possible arrangement of electrons in different (degenerated) states. The degeneracy leads to the so-called multiplicity d_n, the number of possible configurations for a given number of electrons n in the dot. Degeneracy is linked to the states itself, and multiplicity (as it is used here) is linked to electrons occupying the states, i.e., the number of configurations in Fig. 29. Multiplicity is the degeneracy of the charge configurations, and the wording "degeneracy" is, hence, often used for charge configurations, too.

For example, one electron ($n = 1$) in the s-shell has two possible configurations, as the spin degeneracy ($d_1 = 2$) allows us to occupy the s-shell with either spin-up or spin-down (see Fig. 29). Two electrons ($n = 2$) in the s-shell have only one possible configuration (you cannot distinguish if the right or left electron has spin-up or spin-down), i.e., $d_2 = 1$. As a consequence, the possible paths k from $n = 1$ to $n = 2$ is $k_{1\to2} = 1$, while it is in the opposite direction: $k_{2\to1} = 1$. You may wonder why we do not have to count also two possibilities for $k_{1\to2}$, as depicted by a second, dotted-slim black arrow from $n = 1$ to $n = 2$. For the $n = 1$-state, the electron has either spin-up or spin-down, not both at the same time, i.e., we have to count from "only one" initial configuration to all possible final configurations, as already seen in Fermi's golden rule before. I have depicted the other possible transitions from other initial configurations with dotted and slim arrows in Fig. 29. The same holds for the transition by electron tunneling between the $n = 0$ and $n = 1$ states, where $k_{1\to0} = 1$ and $k_{0\to1} = 2$,

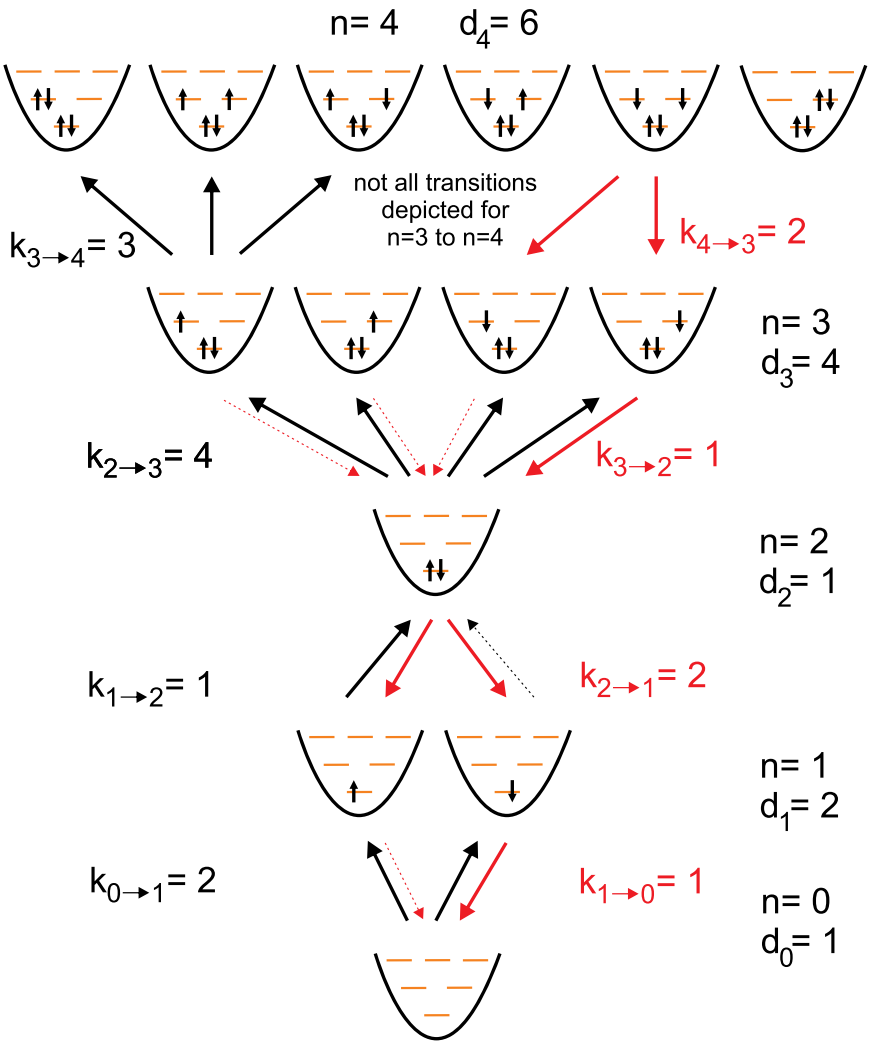

FIG. 29. Possible configurations and transitions in a self-assembled quantum dot with rotational symmetry with no interaction. Different charge configurations for the electron number $n = 0 \ldots 4$ in the dot are depicted with the multiplicity/degeneracy (see the text) d_n and the number of possible transition paths $k_{n\to n+1}$ and $k_{n+1\to n}$. The number of transitions k are given by the number of final accessible configurations for a given initial electron configuration. The thinner dashed arrows in red and black depict possible transitions for different initial electron configurations, giving the same value for k.

respectively. See Fig. 29 for all the other possible configurations and transitions up to $n = 4$.

The number of possible charge configurations (the multiplicity d_n) can be reduced by lifting the degeneracy or by selection rules (Hund's rule). Figure 30 depicts the possible electron configurations for $n = 3$ and 4 in an elongated quantum dot. The elongation will lift the degeneracy of the p-states by ΔE on the order of a few meV, as now the dot has a stronger confinement in the direction of the smaller width and the rotational symmetry is not valid anymore. As a consequence, the energetically favorable p-state will be occupied first with two electrons (see Fig. 30) for $n = 4$, and the multiplicity will be reduced to $d_3 = 2$ and $d_4 = 1$, respectively.

The multiplicity will also be changed, if a dot with rotational symmetry follows Hund's rule for the p-shell. As an example, the fourth electron for $n = 4$ has to have parallel spin, which reduces the multiplicity to $d_4 = 2$ (both spins in the p-shell have parallel up- or down-spin).

However, even if k_n is smaller than d_n, the ratio is constant (check Fig. 29)

$$\zeta_n = \frac{k_{n-1\to n}}{k_{n\to n-1}} = \frac{d_n}{d_{n-1}}. \tag{21}$$

This ratio ζ_n between the possible paths for in- and out tunneling has a strong effect on the transition ("tunneling") rates γ_n^- and γ_n^+. Determining the tunneling rates allows us to trace back to the degeneracy of the states and, hence, obtain information on the (rotational) symmetry and applicability of Hund's rule for self-assembled quantum dots.

For this, we use again the near-equilibrium transconductance measurement,[237] as describe in Sec. V B, where the density of states for

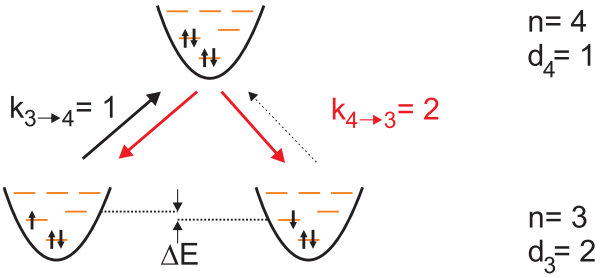

FIG. 30. Possible configurations and transitions for $n = 3$ and 4 in an elongated dot without rotational symmetry. The reduced symmetry reduce the degeneracy and, hence, the number of charge configurations d_n and the number of possible transition paths $k_{n\to n+1}$ and $k_{n\to n-1}$.

the many-particle ground states of the dot ensemble for 1 to 6 electrons is observed, see Fig. 32(b). However, we will now look into the details of the charging/discharging time constants.

Figure 31 shows as an example the dynamics of the tunneling process for charging and discharging the dots with one electron into the s-shell (that means the transition between $n = 0$ and $n = 1$). A significant difference in the time constant (3.2 ms–2.3 ms) can be observed for a small energy shift of $\Delta E \sim 1.4$ meV in the Fermi energy (chemical potential) at a gate voltage $V_g = -0.67$ V. Only a small fraction of about 7% of the quantum dots participates in the charge transfer process, and every dot that participates is charged or discharged with only a single electron, as described before in our simplified model.

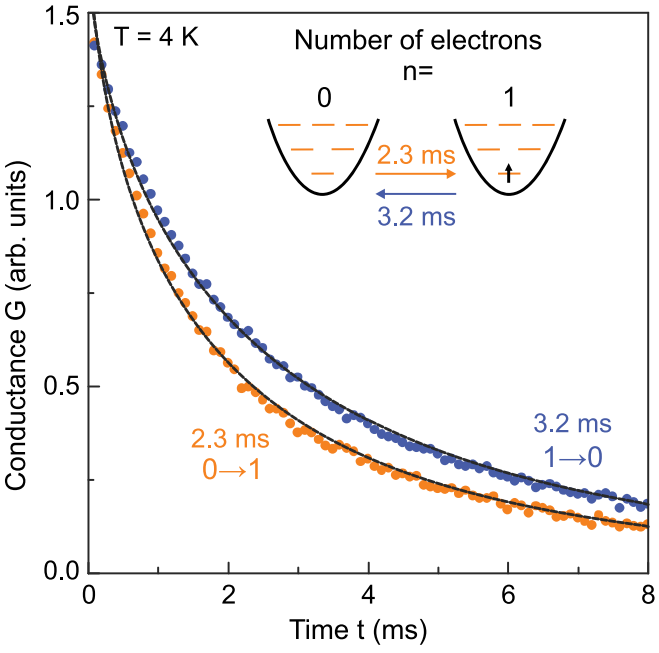

FIG. 31. Conductance transients for charging (0 → 1, orange dots) and discharging (1 → 0, blue dots) with the first electron into the s-shell. The time constants for tunneling in/out differ by a factor of ∼1.4 and are determined by fitting a stretched exponential function (solid lines) to the transients. Adapted with permission from Beckel *et al.*, Europhys. Lett. **106**, 47002 (2014). Copyright 2014 Institute of Physics.[237]

The time constants of $\tau_{0\to1} = 2.3$ ms and $\tau_{1\to0} = 3.2$ ms are obtained by a stretched exponential fit.[258] It accounts best for a quantum dot ensemble, where the time constants differ slightly from dot to dot and are averaged over many dots. It is already clearly visible that the charging time from $n = 0$ to $n = 1$ is faster than the discharging from time from $n = 1$ to $n = 0$.

It is now important to mention that the rates for tunneling into and out of the dot γ_n^+ and γ_n^-, respectively, are not the quantities that are obtained in the time-resolved transconductance. The rate equations (20) contain both tunneling rates (γ_n^+ and γ_n^-), e.g., in the measurement, the overall "relaxation rate" into equilibrium is obtained.

Let us consider again only the n-th transition for an individual quantum dot (the dot is just charged or discharged with one additional electron) and realize that actually the total number of electrons per dot $N(t)$ is measured in the time-resolved transconductance measurement by $G(t)$ (see Sec. V A). We have to solve the rate equations to derive $N(t)$, which is the sum over all charge states n times their probability p_n: $N(t) = \sum_n np_n$. As we only allow charging or discharging with one electron, we get

$$N(t) = np_n + (n-1)p_{n-1} \tag{22}$$

and a rate equation for the n-th charge state

$$\frac{dp_n(t)}{dt} = \gamma_n^+ p_{n-1} - \gamma_n^- p_n. \tag{23}$$

For only two possible charge states, the quantum dot has to be in the state $(n-1)$ or n: $p_{n-1} = 1 - p_n$. We obtain the following rate equation for the total charge:

$$\begin{aligned}\frac{dN(t)}{dt} &= \frac{d}{dt}(np_n(t) - (n-1)(1-p_n)) \\ &= n\frac{p_n(t)}{dt} - (n-1)\frac{p_n(t)}{dt} \\ &= n(\gamma_n^+ p_{n-1} - \gamma_n^- p_n) - (n-1)(\gamma_n^+ p_{n-1} - \gamma_n^- p_n).\end{aligned} \tag{24}$$

Using again the relation $p_{n-1} = 1 - p_n$ and rewriting everything lead to

$$\frac{dN(t)}{dt} = n\gamma_n^+ + (n-1)\gamma_n^- - (\gamma_n^+ + \gamma_n^-)N(t), \tag{25}$$

which is solved by

$$\Delta N = N(t) - N_{eq} = (N_0 - N_{eq})\exp(-t/\tau), \tag{26}$$

with the time constant

$$\frac{1}{\tau} = \gamma_m = k_{n\to n-1}[1 + (\zeta_n - 1)f(E_n)]\Gamma(E_n) \tag{27}$$

and the occupation in equilibrium

$$N_{eq} = n - 1 + \frac{\zeta_n f(E_n)}{1 + (\zeta_n - 1)f(E_n)}. \tag{28}$$

The relaxation γ_m into equilibrium, accordingly the time constant $\tau = 1/\gamma_m$, gives the time evolution in the transient observed in the time-resolved transconductance measurement. We can now see that the relaxation rate depends on the ratio in degeneracies/multiplicity of different charge states n and $n-1$ in ζ_n, cf. Eq. (21).

The previous equations are valid for an individual quantum dot or an ensemble with sharp energy distribution. However, the transconductance measurements are done on an ensemble of dots with an inhomogeneous energy distribution. In such a case, we have to integrate Eq. (26) over all energies of the quantum-dot levels

$$\Delta N(t) \propto \int dE \left[N_{eq}(E \pm \Delta E) - N_{eq}(E)\right] e^{-t/\tau(E)}, \tag{29}$$

where $N_{eq}(E \pm \Delta E)$ and N_{eq} are the equilibrium occupation of the quantum dots before and after the voltage pulse, respectively. The actually measured time constant of the relaxation is a result of an average of energy-dependent time constants $\tau(E)$ within the subensemble which are charged and discharged.

As a consequence of that averaging over many time constants, Eq. (29) has to be solved numerically, and the time constants are extracted by a fit to the simulation data. Putting the asymmetry in the charge relaxation time into the ratio

$$\nu_n = \frac{\tau_{n\to n-1}}{\tau_{n-1\to n}} \tag{30}$$

allows us to compare the experimental data (black data points with error bars) of ν with theoretical simulations for different filling sequences of the s- and p-shells (different lines), shown in Fig. 32(a). Figure 32(b) shows again the density of equilibrium states for sequentially filling of the dot states from n = 1 in the s-shell up to n = 6 of a completely filled p-shell.

Three different models have been calculated, assuming that the dots have (i) rotational symmetry with noninteracting particles, (ii) rotational symmetry with Hund's rule applied, and (iii) a potential that is elongated and the degeneracy of the p-shell is lifted into a p_x- and a p_y-state. The sequence for the multiplicity will be different for the p-shell in each case, where the sequence would be (i) d_3, d_4, d_5, and $d_6 = 4$, 6, 4, and 1 for rotational symmetry with no interaction, (ii) 4, 2, 4, and 1 with Hund's rule, and (iii) 2, 1, 2, and 1 for an elongated dot (see Figs. 29 and 30). The results of the simulations are plotted in Fig. 32(a) and compared with the experiment.

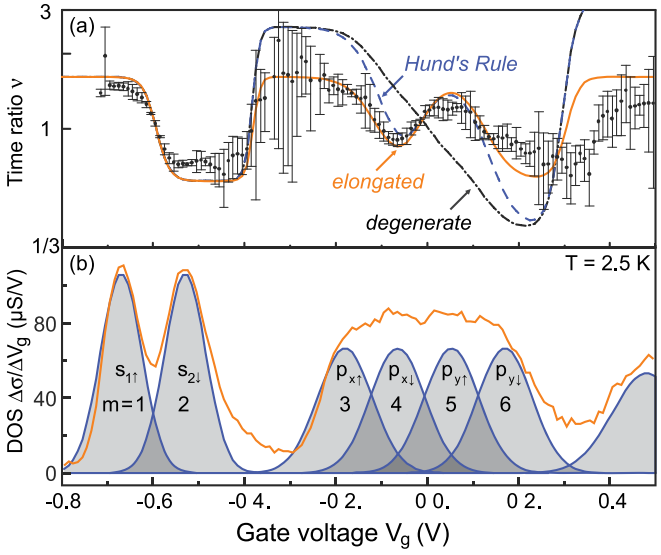

FIG. 32. Asymmetry in the relaxation times. (a) Measured (dots with error bars) and calculated (different lines) ratios ν_n (see the text) for electron tunneling into and out of the quantum dots. Comparison between calculated and measured ratios shows that the quantum dots have no rotational symmetry; instead, they are elongated. (b) The density of states (DOS), measured by the transconductance spectroscopy (orange line). The shaded areas with blue lines show fits to the measured data. Adapted with permission from Beckel *et al.*, Europhys. Lett. **106**, 47002 (2014). Copyright 2014 Institute of Physics.[237]

The model for an asymmetric (elongated) quantum dot with lifted p-shell degeneracy shows the best agreement with the experimental data and is in agreement with other measurement techniques on self-assembled quantum dots, especially with the results from wave-function mapping.[82,84,259–261] It demonstrates that the time-resolved spectroscopy is a very powerful tool to gain insights into the electronic states and their degeneracy.

We have always assumed that maximal one electron per quantum dot is transferred between the 2DEG and the dot states. However, if the pulse amplitude is increased, this assumption is not valid anymore, and during the relaxation process, electrons can tunnel in such a way that any transition between every n and n' charge state is allowed. Then, the charge carrier dynamics can be described by a more general rate equation (also called "master equations")

$$\frac{dp_n}{dt} = \sum_{n' \neq n} \Gamma_{n'\to n}\, p_{n'} - \sum_{n' \neq n} \Gamma_{n\to n'}\, p_n. \tag{31}$$

It describes the probability in general for finding a quantum dot charged with n electrons for a set of transition rates for charging $\Gamma_{n'\to n}$ and discharging $\Gamma_{n\to n'}$, respectively. For more information in master equations, see Beenakker.[262]

VI. SINGLE ELECTRON DYNAMICS IN AN OPTICAL DETECTION SCHEME

Up to now, the charge carrier dynamics of an "ensemble" of self-assembled InAs quantum dots was probed by the time-resolved transconductance measurements. This limitation of probing millions and millions of dots simultaneously can be overcome by using an optical detection scheme: Resonance fluorescence in a confocal microscope.

A. Time-resolved observation of single electron tunneling into a single dot

We come back to the resonance fluorescence signal that depends on laser energy and gate voltage (cf. Fig. 14): Fig. 33(b) shows a zoom-in into such a 2D-scan of the exciton and trion transitions, where three different areas can be identified. For gate voltages below 0.26 V (labeled with 1), the quantum dot is always empty [as schematically depicted in Fig. 33(a), left], and the exciton transition with the two fine-structure lines is visible. For higher gate voltages than $V_g = 0.27$, the Fermi level in the charge reservoir is always above the s-shell in the dot, and hence, the dot is filled [Fig. 33(a), right], and the trion transition is observed in the resonance fluorescence. Between these two configurations in the gray shaded area of Fig. 33(b), the Fermi level is aligned to the s-states in the dot within the energy broadening of the Fermi distribution. Both transitions of exciton and trion are visible simultaneously in such steady-state measurements as the electrons

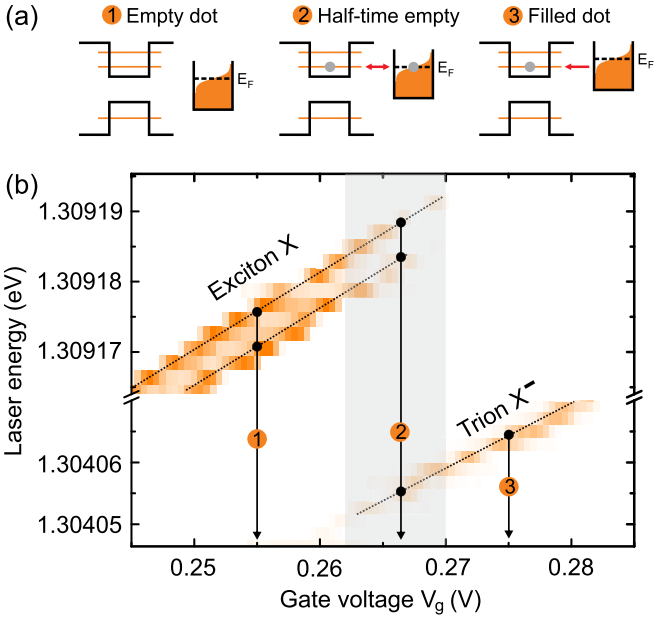

FIG. 33. Resonance fluorescence of a single InAs quantum dot. (a) Schematic pictures of the electron tunneling between the charge reservoir (with Fermi energy E_F) and the quantum dot. (b) Resonance fluorescence measurement for different gate voltages V_g and laser excitation energies at the exciton X to trion X^- transition. At a gate voltage of $V_g = 0.255$ V (labeled with 1), the dot is always empty and the exciton transition X is visible. At a gate voltage of 0.274 V, the quantum dot is always filled with one electron and the trion transition X^- is observed. At position 3, the dot is filled half of the time, as the electron tunnels back and forth into and out-of the dot; both transitions are visible simultaneously.

tunnel back and forth between the dot and the reservoir [as schematically depicted in Fig. 33(a), middle]. The gate voltage controls the average time the dot is occupied with an additional electron, and hence, the intensity ratio between exciton/trion changes in the gray-shaded area.

The resonance fluorescence can be used now to probe the non-equilibrium charge carrier dynamics between the dot and the reservoir in the voltage range of the gray shaded transition area in Fig. 33(b). The measurement principle of this "optical detection scheme for transport measurements" works as follows: To charge and discharge the quantum dot (and observe the charging/discharging time resolved in a tunneling transient), a voltage pulse is applied to the gate contact, while the resonance fluorescence on the exciton or trion transition is measured. The optical excitation of the exciton transition is switched off, if an electron tunnels into the dot. At the same time, the trion transition is switched on for a charged quantum dot. The on-off switching is due to the fact that the energy shift of the excitonic transition (due to the Coulomb interaction) is much larger than the excitonic linewidth (≈ 1 μeV).

In order to measure the electron tunneling between the reservoir and the dot, an electrical pulse sequence is applied to the gate electrode that consists of two voltage settings: (i) An initial voltage V_{ini} is chosen so that the dot is uncharged (or charged) and the exciton transition (or trion transition) is out of resonance with the diode-laser frequency. In this case, no resonance fluorescence signal is observed, as visible for times $t < 0$ in Fig. 34(a). (ii) The second pulse voltage V_g shifts the levels of the quantum dot via the quantum-confined Stark effect in resonance with the laser. This Stark shift is faster than the average tunneling time of the electrons, and the fluorescence signal of the exciton is observed just after the gate pulse [at t = 0 in Fig. 34(a)]. The dot is now in a nonequilibrium situation with the reservoir, and the Fermi level in the contact is energetically higher than the lowest level in the s-shell [cf. Fig. 33(a), inset 3]. Relaxation into equilibrium by electron tunneling is observed by averaging over many voltage pulse cycles in an "n-shot measurement" as an exponential decay in the fluorescence signal in Fig. 34(a) for different pulse voltages. The vanishing exciton signal is due to the additional electron inside the dot, as in equilibrium the trion transition would be in resonance at different laser energies.

Figure 34(a) shows the quenching of the exciton transition for three different voltage pulses, where at point 1 ($V_g = 0.255$ V), the resonance fluorescence signal is nearly constant. At this pulse voltage, the Fermi level in the back contact is below the levels in the s-shell of the dot and no tunneling occurs (in agreement with the observation in the static fluorescence measurement in Fig. 33). The origin of the small decrease in the fluorescence intensity is a second tunneling path into the dot that contains already an additional exciton by the laser excitation, as explained in more detail later.

For a gate voltage of $V_g = 0.267$ V at point 3 in Fig. 34, a stronger exponential decay of the fluorescence signal is visible with a saturation value of about 40% of the maximum amplitude. In such an n-shot measurement, which is an average over the quantum jumps of the electron between the dot and the reservoir, the average normalized amplitude [see also Fig. 34(b)] describes the average time the electron is in the reservoir or in the dot. At $V_g = 0.275$ V, the exciton transition quenches completely and the electron tunnels into the dot with a probability of 100%. The s-shell is now always occupied with one electron in equilibrium, and the fluorescence of the exciton is absent.

The amplitude in equilibrium at $t = 40$ ms (i.e., for a pulse duration much longer than the inverse tunneling rate) for different gate voltages measures the average occupation of the dot and, of course,

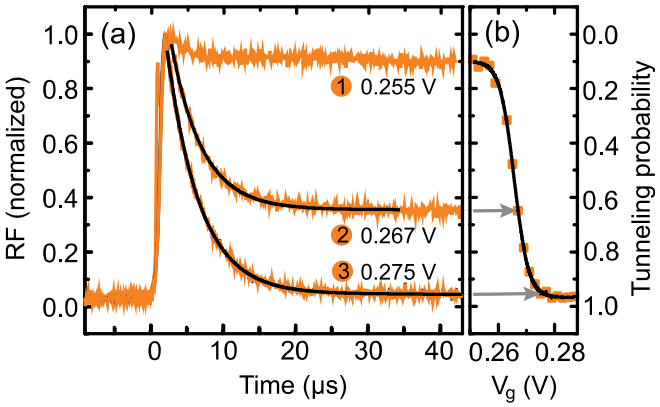

FIG. 34. Transients of single electron tunneling. (a) Time-resolved resonance fluorescence, measured on the exciton transition during an applied gate voltage pulse. The transient displays the tunneling of an electron into the dot, which is detected by a quenching of the intensity in an n-shot measurement. (b) Equilibrium amplitude at different gate voltages, resembling the Fermi-distribution in the charge reservoir. Data are reproduced from Ref. 263.

also the average occupation in the reservoir, which is determined at finite temperature by the Fermi distribution. Figure 34(b) displays a fit to the Fermi distribution, which yields a temperature of 4.2 K, in perfect agreement with the sample temperature in this experiment.

B. Electron-exciton interaction

The important difference between the all-electrical measurements in Sec. V and the optical measurements is the additional influence of the optical generation of excitons. This electron-hole pair generation has important consequences on the tunneling dynamics: The exciton will influence the tunneling rate, and the electron occupation probability can be tuned by the optical excitation, i.e., the laser excitation power.[263] The first phenomenon (the influence of the exciton on the electron tunneling) will be discussed in this subsection, while the tuning of the tunneling rate will be addressed later on.

A model to calculate the electron, hole, and exciton energy depending on the applied gate voltage is described in Seidl *et al.*,[264] where these energies are given by the Coulomb interaction and the electrostatic potential. Taking the resonance fluorescence measurements into account, an electron-electron on-site Coulomb energy of 28 meV, an electron-hole on-site Coulomb energy of 33 meV, and a confinement energy of 172 meV are found for the present dot. As a result of this model, the gate voltages can be derived, where electron/hole tunneling into or out of the dot occurs. The tunneling voltages are given as intersections of the lines in Fig. 35 for the energies of the hole (E(h)), the exciton (E(X)), and the trion (E(X^-)) state and the empty (E(0)), the singly- (E(e)), and the doubly-charged dot (E(2e)).

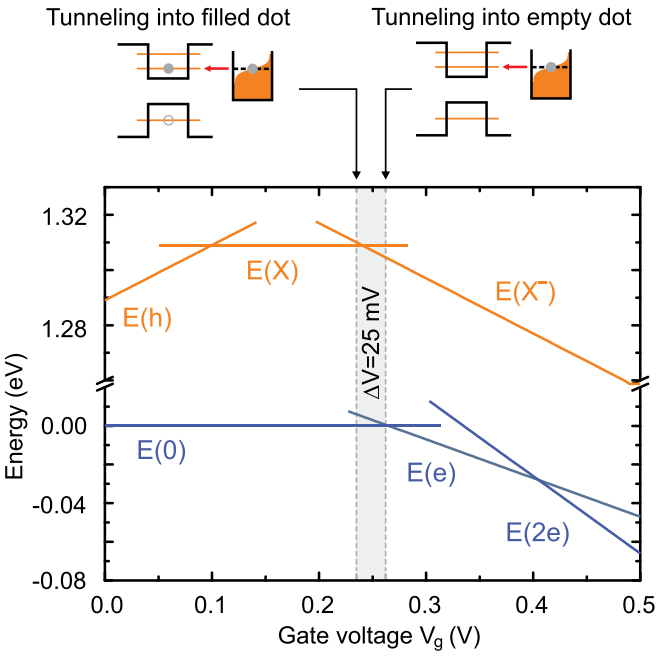

FIG. 35. Energies of different many-particle states in the dot vs gate voltage. The solid orange lines display the calculated energy for a singly-charged dot with an additional hole $E(h)$, the exciton state $E(X)$, and the negatively charged trion $E(X^-)$. The blue lines show the energies of the negatively singly $E(e)$ and doubly charged dots $E(2e)$ in comparison to the empty state $E(0)$. Gate voltages where tunneling into the empty dot and into the excitonic state is possible are marked with gray dashed lines.

The intersection between the energy of the exciton and the trion gives the gate voltage, where an electron tunnels into a dot that is already charged with an exciton. The energy difference to the gate voltage where an electron tunnels into an empty quantum dot is 25 mV (gray shaded area). This smaller gate voltage for tunneling into the charged dot explains the small decrease in the amplitude of the fluorescence signal in Fig. 34(a) at $V_g = 0.255$ V and shows that the optical exciton generation has a strong influence on the electron dynamics. The electron can tunnel already into the exciton state where no tunneling into the empty dot would be possible.

C. Tuning the tunneling rate by the optical excitation

As the optical exciton generation influences the electron dynamics, it can also tune the electron tunneling into the quantum dot and the overall relaxation rate into equilibrium. More precisely, an optically generated exciton as an electron hole-pair will occupy with certain probability p_X the s-shells in the dot. As we have seen in Sec. V G, an electron in the s-shell changes the multiplicity and, hence, the tunneling rate for another electron into the dot. Increasing the incident laser power increases the probability p_X and changes the tunneling and hence the relaxation rate into equilibrium. This will be demonstrated and explained in this section.

At this point, I would like to mention again that there is a strong difference in the "tunneling rate" and the "relaxation rate": In the n-shot time-resolved measurement in Fig. 34, the relaxation rate into equilibrium is observed, which depends on the tunneling rate into the dot and the rate out of the dot, as already explained in Sec. V G. The tunneling rate is the correct wording for one path (into or out of the quantum dot), while the relaxation rate is the overall rate into an equilibrium situation.

With the optical excitation of an exciton, we have now another "tuning knob" (parameter) to change the tunneling rate of electrons from the 2DEG into the s-shell and change, as a consequence, the overall relaxation rate γ_m into equilibrium. How this optical tuning knob influences the relaxation dynamics should be described again by a rate equation model,[237,262] in which the exciton generation has to be added.

Before starting with the equations, we have to do some more wording and introduce a fluorescent and a nonfluorescent state, see Fig. 36. Both states consist of two substates again. The two substates of the fluorescent state are the empty quantum dot ($|0\rangle$) and the dot filled with a single exciton ($|X\rangle$). The wording fluorescent comes from the fact that the laser should now excite the exciton transition, i.e., it drives the system between these two substates. The nonfluorescent state includes also two substates, where the dot is occupied with one electron ($|e\rangle$) and the negatively charged trion ($|X^-\rangle$), both not optically active (as the chosen laser frequency will only drive the exciton transition).

One more sentence for explanation: The reason for introducing a fluorescent and nonfluorescent state is that we acutely measure the fluorescent state in the resonance fluorescence, i.e., this state is observable in the same manner as we introduced the total number of electrons $N(t)$ in the electrical measurement in Sec. V G before.

The excitation of the exciton (the transition $|0\rangle \rightarrow |X\rangle$) is possible with an absorption rate γ_{abs}. The exciton $|X\rangle$ can recombine with

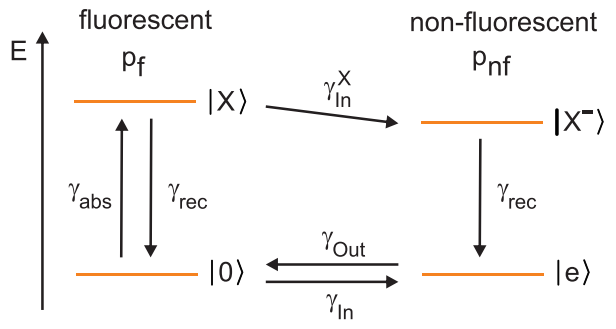

FIG. 36. Energy scheme of the fluorescent and nonfluorescent states. For a gate voltage of about $V_g = 0.265$ V, the energy of the $|0\rangle$ state is aligned with the energy of the $|e\rangle$ state. Arrows indicate optical and transport transitions with their respective rates γ.

the recombination rate γ_{rec} (the transition $|X\rangle \rightarrow |0\rangle$), and p_X is the probability for finding an exciton in the dot (the average occupation)

$$p_X = \frac{\gamma_{abs}}{\gamma_{abs} + \gamma_{rec}}. \tag{32}$$

It can be derived from the differential equation in the steady state $dp_X/dt = 0$

$$\frac{dp_X}{dt} = \gamma_{abs}(1 - p_X) - \gamma_{rec}\, p_X. \tag{33}$$

Keep in mind that for the equations that follow, "p_X" is the average exciton occupation in the dot which is directly related to the laser power.

An electron can also tunnel into an empty quantum dot with a tunneling rate defined as γ_{In} and tunnel out of the dot with a rate γ_{Out}, where the in- and out-tunneling rates can be expressed by[256,257]

$$\gamma_{In} = k_{In}\Gamma f(E), \tag{34}$$

$$\gamma_{Out} = k_{Out}\Gamma(1 - f(E)), \tag{35}$$

where Γ is the intrinsic tunneling rate (just given by the tunneling barrier) and $f(E)$ the Fermi distribution. The prefactors k_{In} and k_{Out} describe the number of possible paths for tunneling in and out of the dot [see Eq. (21)]. Two spin directions are possible for tunneling one electron into an s-shell of an empty dot, i.e., $k_{In} = 2$, while for tunneling one electron out of the dot, $k_{Out} = 1$. As the quantum dot can be optically excited with an exciton in the resonance fluorescence, an electron can also tunnel into an excitonic state with the tunneling rate γ^X_{In}. The gate voltage is set in the experiment to a situation, where for the electron tunneling into an exciton the Fermi distribution in the reservoir equals always unity, so that Eq. (35) simplifies to $\gamma^X_{In} = k_X \cdot \Gamma^X_{In}$.

The degeneracy of the s-shell and, hence, the number of possible paths for tunneling into the s-shell under optical excitation change with laser power. At low power, the dot is most of the time empty, and the degeneracy for tunneling into the dot is $k_X = 2$. At high excitation power, the average exciton occupation saturates at one half since the dot is half of the time filled with an exciton. The average degeneracy/multiplicity for tunneling into an exciton is lowered to $k_X = 1.5$, i.e., tunneling into the dot is optically blocked for high laser power.

Coming back to the rate equations: With different discussed rates and the assumption that the recombination rate γ_{rec} is much higher than the tunneling rates, rate equations for the fluorescent and nonfluorescent states can be written as follows (cf. Fig. 36), where the probability for the exciton occupation p_X is given by Eq. (33):

$$\frac{p_f(t)}{dt} = -(1 - p_X)\,\gamma_{In}\,p_f(t) + \gamma_{Out}\,p_{nf}(t) - \gamma^X_{In}\,p_f(t)\,p_X, \tag{36}$$

$$\frac{p_{nf}(t)}{dt} = -\frac{p_f(t)}{dt}. \tag{37}$$

The first summand in Eq. 37 describes the reduction (the minus sign) of the fluorescent state p_f by electron tunneling (with rate γ_{In}) into the empty dot $|0\rangle$, where the probability of having an empty QD in the fluorescent state is given by $1 - p_X$ (no exciton means empty dot). Analogously, the second summand describes the increase in the fluorescent state by electron tunneling out of a charged dot in the nonfluorescent state, and the third summand is for tunneling into the exciton state with rate γ^X_{In}. The average exciton occupation can be tuned here by the laser power from $p_X = 0$ up to saturation at $p_X = 0.5$ (see upper insets in Fig. 37 as a schematic representation).

Using the boundary conditions $p_f(0) = 1$ and $p_f + p_{nf} = 1$ yields

$$p_f(t) = \frac{(\gamma_m - \gamma_{Out})e^{-\gamma_m t} + \gamma_{Out}}{\gamma_m}, \tag{38}$$

with the relaxation rate

$$\gamma_m = \gamma_{Out} + (1 - p_X)\,\gamma_{In} + \gamma^X_{In}\,p_X. \tag{39}$$

The time-resolved measurements in Fig. 34 show directly the occupation probability of the dot with an electron. The decrease in the

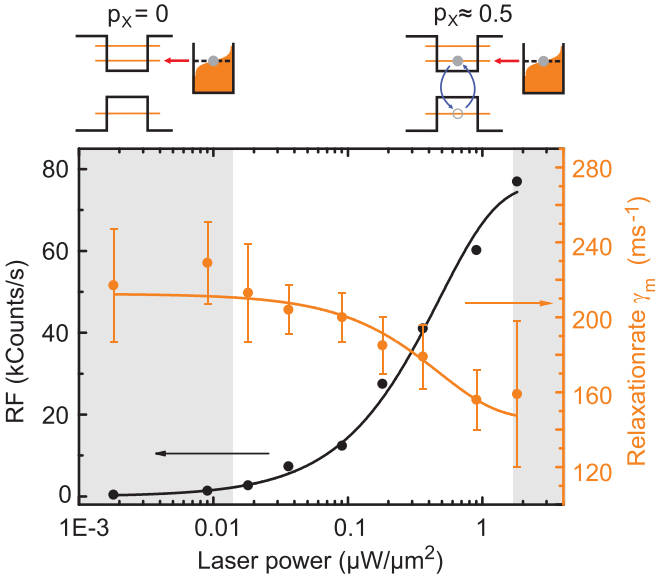

FIG. 37. Optical tuning of the transport relaxation rate. The relaxation rate γ_m for the electron tunneling into equilibrium (orange dots) and the intensity of the fluorescence signal (black dots) as functions of the laser excitation power. The relaxation rate γ_m is reduced by optical blocking of the electron tunneling from the reservoir into the dot. Reprinted with permission from Kurzmann *et al.*, Phys. Rev. Lett. **117**, 017401 (2016)]. Copyright 2016 the American Physical Society.

resonance fluorescence signal is related to electron tunneling into the dot (transition from the fluorescent to the nonfluorescent state in Fig. 36), quenching the probability $p_f(t)$ of finding an optically excited exciton. $p_f(t)$ reflects the measured transients with a decay constant γ_m given by Eq. (39).

The transients in Fig. 34 were measured in saturation of the exciton transition. Saturation means here that the laser drives constantly the transition from $|0\rangle \rightarrow |X\rangle$ (absorption) and back $|X\rangle \rightarrow |0\rangle$ (stimulated emission). The quantum dot undergoes Rabi oscillations, where the absorption rate is at least as high as the recombination rate $\gamma_{abs} \geq \gamma_{rec}$. Saturation is achieved here for laser excitation powers larger than 1 μW/cm^2 in Fig. 37. In this situation, the quantum dot is half of the time filled with on exciton, which means $p_X = 0.5$. This leads interestingly to a constant relaxation rate γ_m in Eq. (39)

$$\begin{aligned}\gamma_m &= \Gamma(1 - f(E)) + 0.5 \cdot 2f(E)\Gamma + 0.5\gamma_{In}^X \\ &= \Gamma + 0.5 \cdot \gamma_{In}^X, \end{aligned} \tag{40}$$

independent of the Fermi distribution and in very good agreement with the measure transients in Fig. 34. This is very counter-intuitive, as from pure transport experiments, we would expect that the relaxation transients should depend on gate voltage, as it changes the tunneling rates γ_{In} and γ_{Out} by the alignment of the Fermi energy and, hence, the relaxation rate γ_m into equilibrium.

As shown in Eq. (39), the overall relaxation rate γ_m depends on the tunneling rate for electrons into the dot γ_{In}, which again depends on the number of possible paths k_{In} in Eq. (34). Tuning the average occupation with an exciton by the laser excitation from $p_x = 0$ to $p_x = 0.5$ decreases k_{In} from 2 down to 1.5. This optical tuning of the relaxation rate γ_m by changing the average occupation of the dot with an exciton p_n (an optical blocking effect) can be seen in these time-resolved measurements too. Increasing the laser power (black dots and line in Fig. 37) decreases the relaxation rate γ_m from 220 ms^{-1} by the predicted factor of 1.5 down to $\approx$150 ms^{-1} (orange dots in Fig. 37). This optical blocking could be used to control tunneling rates by optical means, where the switching speed is only limited by the Rabi frequency of the optical transition. It is important to note here that the definition of "saturation" is normally slightly different in quantum optics experiments. I have used saturation here for a situation that the QD is half-time filled with an exciton. In the quantum optics literature,[194] saturation is defined for a situation, where the resonance fluorescence signal equals half its maximum value. As an example, saturation would be in the literature in Fig. 37 for a RF intensity of about 40 kCounts/s at a laser power of $\sim$0.4 μW/cm^2.

D. Nonequilibrium measurements on the trion transition

The nonequilibrium measurements of the relaxation process were measured until now by resonant excitation on the exciton transition. However, in principle, every optical transition of the dot can be used. This section shows results, where the trion transition has been used as an optical nanodetector. The trion transition is quenched in the case of an electron that tunnels *out* of the dot, and the optical detection leads to more interesting nonequilibrium effects: The observation of an Auger recombination within a single self-assembled quantum dot.

For a time-resolved measurement on the trion transition, the dot is at the beginning already charged with an electron for times $t < 0$ μs in Fig. 38. At $t = 0$, a gate voltage pulse V_g shifts the Fermi energy slightly down in energy and the electron can tunnel out of the dot with a certain probability. Again, the overall relaxation rate γ_m is measured in Fig. 38. The gate voltage pulse changes slightly the rates between tunneling into the dot γ_{In} and tunneling out of the dot γ_{Out} and, hence, the overall relaxation rate. Figure 38 shows transients for different gate voltages. For $V_g = 0.252$ V, the intensity of the resonance fluorescence of the trion decreases to almost zero at $t = 40$ ms. In this situation, the dot is always uncharged in equilibrium, and the exciton transition is out of resonance with the excitation laser (no resonance fluorescence counts).

An increasing equilibrium amplitude of the resonance fluorescence signal is observed for increasing gate voltage, a similar behavior to the measurements before, as the Fermi distribution in the charge reservoir determines this amplitude. However, a very interesting observation can be made in the transient for a gate voltage of $V_g = 0.276$ V: The Fermi function equals unity for this gate voltage, i.e., the electron charged into the dot before $t = 0$ should have no tunneling path back into the reservoir (as all states are occupied) and the fluorescence intensity should stay constant at its maximum value for $t = 0$. The origin of this transient is the nonradiative Auger recombination.

E. Auger recombination

The atomic Auger process is a many-particle scattering process, where in an atom the transition energy of an electron between two states is transferred to another electron. The Auger electron leaves the atom with a well-defined kinetic energy, a fact that is used for an element specific analysis by Auger-spectroscopy.[265] In a semiconductor nanostructure, such as a self-assembled or colloidal quantum dot,[20]

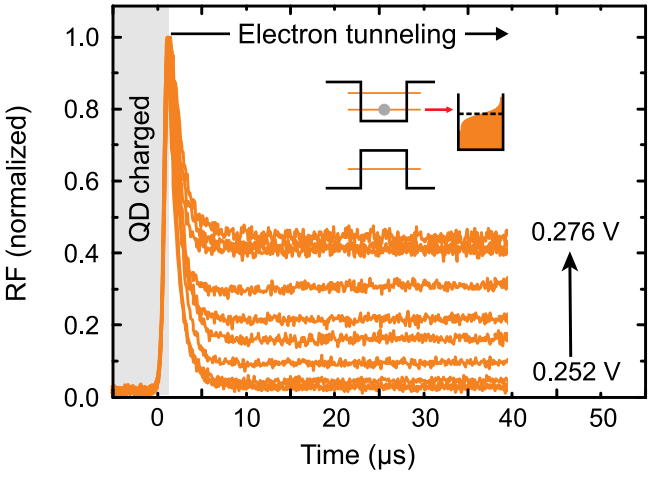

FIG. 38. Time-resolved resonance fluorescence on the trion transition. At $t = 0$, the electrical pulse shifts the Fermi energy in the reservoir below the s-shell of the quantum dot, and tunneling of an electron from the dot into the reservoir takes place (see the inset), quenching the fluorescence of the trion transition. Reprinted with permission from Kurzmann *et al.*, Phys. Rev. Lett. **117**, 017401 (2016). Copyright 2016 the American Physical Society.

the electronic transition occurs between the conduction and the valence band. The electron-hole recombination energy can be transferred to another charge carrier within the dot that is scattered into the environment. This effect has been studied very intensively in colloidal quantum dots,[266–268] where a fast Auger recombination time in the range of picoseconds[267,269] quenches the optical transition lines, a negative influence that limits the efficiency of colloidal dots in optical devices.[270–272]

The Auger scattering time is orders of magnitude longer in self-assembled quantum dots (due to the larger lateral size of these dots) on the order of nano- to microseconds, if extrapolated from the size dependence of the Auger process.[273] However, it has still an negative influence on the optical transitions, shown in this section about the Auger recombination of the trion transition in a self-assembled quantum dot.[274] For the negatively charged exciton (the negative trion), the Auger effect removes the additional electron from the dot, leaving it in its empty ground state [see the inset in Fig. 39(b)].

The Auger recombination can be studied first in a two-color laser excitation experiment. The first laser is set in resonance with the energy of the trion transition and the second with the energy of the exciton transition (at the same gate voltage). The observation of the trion and exciton transitions at the same gate voltage [see spectra in Fig. 39(b)] works here as follows: The Auger recombination discharges the quantum dot completely under resonant excitation on the trion transition, leaving the dot empty as long as no electron tunneling with rate $\gamma_{In} = 0.18\,\mu s^{-1}$ from the charge reservoir has occurred. The uncharged dot can be excited on the exciton transition as long as it is empty, observed at the same gate voltage in Fig. 39(b).

The resonance fluorescence intensity of the trion and exciton has been measured for a wide range of laser powers, shown in Fig. 39(a). The exciton intensity is by more than an order of magnitude larger than the trion intensity. This observation can be easily explained by the fact that as long as no electron has tunneled back into the dot from the reservoir, the trion transition is quenched. This reduces the integrated intensity of the trion, where the reduction is directly related to the tunneling rate γ_{In}. The lower intensity of the trion compared to the exciton indicates an Auger recombination rate γ_a higher than the tunneling rate γ_{In}. The quantum dot is most of the time empty in this nonequilibrium situation.

The Auger recombination rate can be determined by an n-shot time-resolved resonance fluorescence measurement, see Fig. 40(b). This measures the relaxation rate from a nonequilibrium into a steady-state situation, where the Auger rate γ_a (trion → empty dot) competes with the tunneling rate γ_{In} (empty dot → trion), cf. Fig. 40(a). Resonant excitation of the trion transition by only "one laser" is used in the following experiment. At $t = 0$, the laser is switched on, and the dot that contains an electron is excited into the trion state with an absorption rate γ_{abs}, see Fig. 40(a). When the dot is charged with a trion, Auger recombination can occur with rate γ_a, switching the trion transition off until an electron tunnels into the dot again (with rate γ_{In}). The evolution from a dot that is charged with a probability of 100% with a trion to the steady-state situation is observed as exponential decay with the relaxation rate γ_m in Fig. 40(b).

For low laser excitation power, where the average trion occupation is $p_{X^-} = 0.003$, the time evolution of the normalized fluorescence signal is nearly constant, as the dot is most of the time in the singly charged state [left picture in Fig. 40(a)] and the Auger recombination

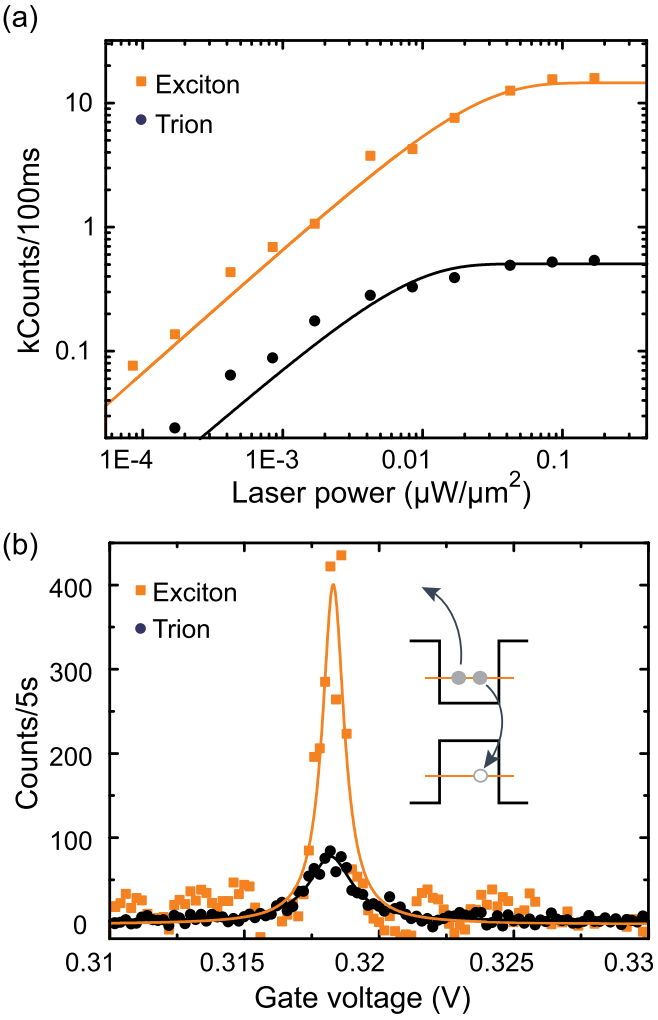

FIG. 39. Auger recombination of the trion transition. (a) Intensity of the resonance fluorescence signal of the trion (black) and exciton (orange) transitions at a gate voltage of $V_g = 0.318$ V for different laser excitation powers. (b) Simultaneously measured resonance fluorescence spectra of the trion (black dots) and the exciton (orange dots).

is negligible. Increasing the laser excitation increases the probability of the dot to be in the excited trion state p_{X^-} [middle picture in Fig. 40(a)] and hence the probability for an Auger recombination process. With increasing p_{X^-}, the decrease in the steady-state value in the normalized fluorescence becomes more pronounced and increases to 80% for saturated excitation ($p_{X^-} = 0.5$). The reduction of the fluorescence signal in the steady-state depends on the ratio between Auger recombination γ_a and tunneling rate γ_{In}, which are effected by the size of the dot (Auger rate)[273] and the tunneling barrier (tunneling rate).

The time evolution of the fluorescence signal (here of the trion transition with probability p_{X^-} for an occupation with a trion) is given by the differential equation

$$\frac{dp_f}{dt} = \gamma_{In}\, p_{nf}(t) - \gamma_a\, p_f(t)\, p_{X^-}, \tag{41}$$

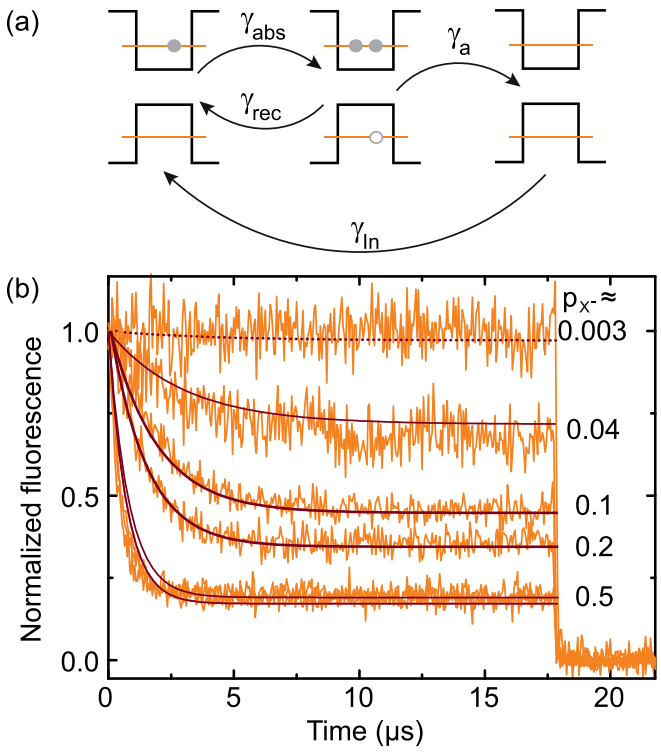

FIG. 40. Time-resolved measurement of the Auger recombination. (a) Schematic illustration of different processes that are involved in the relaxation process into equilibrium (tunneling rate γ_{In}, Auger recombination rate γ_a, absorption γ_{abs}, and recombination rate γ_{rec}). (b) Time-resolved measurement on the trion transition. The laser is switched on at $t = 0$ for different laser excitation powers. The laser power changes the average occupation of the dot with a trion from $p_{X^-} = 0.003$ up to saturation $p_{X^-} = 0.5$. The lines are calculations of the decay rate using a rate equation model. Adapted with permission from Kurzmann *et al.*, Nano Lett. **16**, 3367 (2016). Copyright 2016 American Chemical Society.

where p_{nf} and p_f are the occupation probabilities of the trion transition p_f (fluorescent state) and the empty dot p_{nf} (nonfluorescent state). The average occupation of the trion state is given by p_{X^-}, where the saturation curve in Eq. (12) describes its dependence on the excitation power, detuning, and dephasing time.

The initial condition $p_f(0) = 1$ is used to obtain

$$p_f(t) = \frac{\gamma_{In} + \gamma_a p_{X^-} e^{-\gamma_m t}}{\gamma_{In} + \gamma_a p_{X^-}}, \tag{42}$$

with the relaxation rate

$$\gamma_m = \gamma_{In} + \gamma_a p_{X^-}, \tag{43}$$

where $p_f(t)$ directly reflects the measured transients in Fig. 40 with the relaxation rate γ_m. To determine the Auger recombination rate, the tunneling rate γ_{In} has been obtained from the time-resolved measurements of the excitonic resonance fluorescence.[263]

Fitting one transient in Fig. 40(b) with a given value of p_{X^-} [obtained by the saturation curve of the trion transition vs laser power, shown in Fig. 39(a)] yields an Auger rate of $\gamma_a = 2.3\mu s^{-1}$. Using this Auger rate with the fixed value for the tunneling rate γ_{In} and the appropriate value for the trion population p_{X^-} gives a perfect agreement for each transient in Fig. 40(b).

Interesting is a comparison with the Auger rate in colloidal quantum dots. For instance, CdSe dots with a radius of $r = 2$ nm exhibit an Auger rate of $\gamma_a = 0.1$ ps^{-1},[267] orders of magnitude faster than the rate in self-assembled quantum dots here. The reason for this strong difference can be found in the size-dependence of the Auger rate, which scales with $r^{-6.5}$;[273] other effects, as the bandgap or the electronic structure play only a minor role.[275,276] Using this size dependence, an Auger rate of 2.8 μs^{-1} is estimated for a self-assembled dot with a lateral size of 20 nm (radius of $r = 10$ nm), in very good agreement with the measurement.

It is worth noticing that the relaxation rate and, hence, the intensity of the excitonic transition depend on both the tunneling rate and the Auger rate in Eq. (43). A strong suppression of the fluorescence intensity can only be observed if the Auger rate is similar or even larger than the tunneling rate. Otherwise, if an Auger process empties the dot (transition from the fluorescent to the nonfluorescent state), it will be replaced immediately by electron tunneling from the reservoir (transition back from the nonfluorescent to the fluorescent state). This dependence can be seen in the intensity of the trion transition as the ratio between the tunneling and Auger rate, given for $t \to \infty$ in Eq. (42)

$$p_f(\infty) = \frac{\gamma_{In}}{\gamma_{In} + \gamma_a p_{X^-}} = \frac{\gamma_{In}}{\gamma_m}. \tag{44}$$

This equilibrium amplitude of the trion as the probability of the fluorescent state p_f is shown in Fig. 41 for two different laser excitation powers, where the average occupation with a trion in nonequilibrium

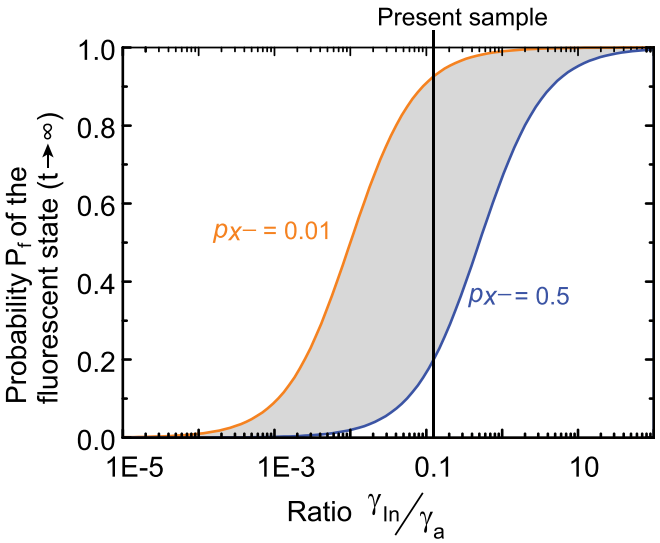

FIG. 41. The influence of the Auger recombination on the fluorescence intensity P_f. Calculations of the normalized steady-state trion intensity (which is directly given by the occupation probability p_f of the fluorescent state) as a function of the ratio between tunneling and Auger rate, γ_{In} and γ_a, respectively. The calculations are shown for two different laser excitations, leading to small $p_{X^-} = 0.01$ (orange line) and high average occupations $p_{X^-} = 0.5$ (blue line) with a trion in nonequilibrium. Adapted with permission from Kurzmann *et al.*, Nano Lett. **16**, 3367 (2016). Copyright 2016 American Chemical Society.

is $p_{X^-} = 0.01$ (orange line) and $p_{X^-} = 0.5$ (blue line), respectively. The average population with a trion p_{X^-} [that follows the saturation curve in Eq. (12)] is the population "before" Auger recombination can take place (in this sense, the occupation with a trion in nonequilibrium at the beginning of the transients in Fig. 40). The probability of the fluorescent state in Fig. 41 is the average occupation with a trion in equilibrium, "after" an equilibrium condition has been established between Auger and tunneling events.

Clearly visible in Fig. 41 is that the ratio between tunneling and Auger rates determines strongly the intensity of this trion transition. For large tunneling rates in comparison to the Auger rate $\gamma_{In} > 10\,\gamma_a$, the trion transition is always "on," a situation that has been observed for most samples with self-assembled quantum dots, where the electron tunneling time from a nearby charge reservoir is below nanoseconds.[83] After Auger recombination, the electron tunnels "immediately" into the dot and the excitation of the trion transition is possible again. On the other side, for a small tunneling rate ($\gamma_{in} < 10^{-4}\,\gamma_a$), the trion fluorescence is completely quenched for any laser excitation power, a situation that is often observed for colloidal dots.[277] The dot is empty after an Auger recombination process, and it takes a long time to return back to the fluorescent state. The thick tunneling barrier yields the low tunneling rate that is only a factor of 10 smaller than the Auger rate in the present sample. The resonance fluorescence intensity of the trion in equilibrium can be tuned by the excitation laser power, as calculated in Fig. 41 (black vertical line) and measured in Fig. 40.

The interplay of the Auger recombination and the electron tunneling not only has a strong influence on the intensity of the trion transition but also affects strongly the linewidth. Figure 42(a) shows time-dependent measurements on the trion transition. It covers times ranging from t = 0, where the dot is singly charged in a nonequilibrium situation, to $t = 3\,\mu$s, where in a steady-state situation, the charge state depends on the interplay of tunneling and Auger processes. An increasing linewidth from 1.3 μeV up to 2.1 μeV is observed in Fig. 42, demonstrated for $t = 0$ and $t = 10\,\mu$s, respectively. This line broadening can be explained by the influence of the detuning $\Delta\omega$ on the relaxation rate γ_m [see Eqs. (43) and (12)]. The relaxation rate depends on the trion population p_{X^-}, which again depends strongly on the detuning again, visible in Eq. (12). More detuning from the maximum of the resonance leads to a smaller Auger recombination effect, increasing the amplitude of the resonance at the edges in comparison to the center, effectively increasing the linewidth.

The linewidth w of any excitonic transition already depends on the laser excitation power, via the so-called "power broadening,"[194] which is the linewidth at $t = 0$

$$w(t=0) = \frac{2}{T_2}\sqrt{1 + \Omega^2 T_1 T_2}, \tag{45}$$

where the Rabi frequency Ω is determined by the laser excitation. The linewidth with Auger recombination at $t = 10\,\mu$s can be calculated by using Eqs. (12), (44), and (56) (without any adjustable parameter)

$$w(t\to\infty) = \frac{1}{T_2}\sqrt{\frac{T_2^2\, w(t\to 0)^2\,(\gamma_a + 2\gamma_{In}) - 4\gamma_a}{2\gamma_{In}}}. \tag{46}$$

The linewidth (the full width half maximum—FWHM) vs the laser power at $t = 0$ and $t = 10\,\mu$s is plotted together with the calculations from Eqs. (45) and (46) in Fig. 42(c), demonstrating a very good agreement between the experiment and calculations. Moreover, the T_2-time can be estimated from the width at $t = 0$ for very low laser excitation to be $T_2 = 975$ ps, which agrees with previous measurements in the literature.[58]

This last section has shown that the Auger recombination leads to a decrease in intensity and an increase in the linewidth. Therefore, it has a twofold negative influence on the optical properties of the quantum dots, in general on all semiconductor nanostructures, especially colloidal dots. However, an electron reservoir in the vicinity of the nanostructure which replenishes the ejected carrier with an injection time faster than the Auger recombination could improve the optical

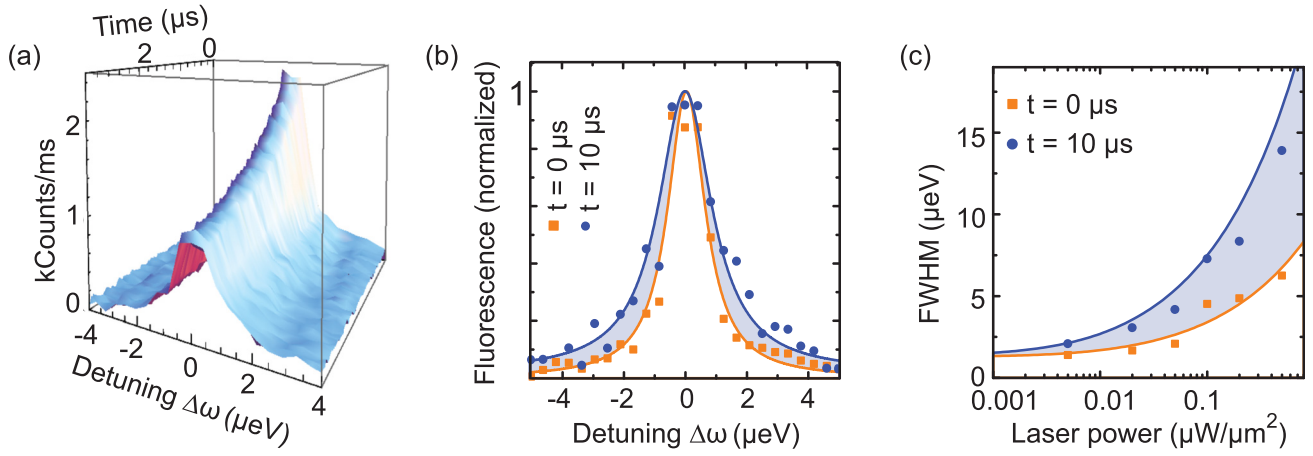

FIG. 42. Time-resolved measurements on the trion transition line. (a) Evolution of the trion transition line after switching on the excitation laser at $t = 0$, where a strong decrease in the amplitude is observed. (b) The normalized trion resonance at $t = 0$ and $t = 10\,\mu$s shows the broadening of the transition line due to the Auger recombination. (c) Linewidth of the trion at $t = 0$ and $t = 10\,\mu$s for different laser excitation powers. The lines are fits to the data. Adapted with permission from Kurzmann *et al.*, Nano Lett. **16**, 3367 (2016). Copyright 2016 American Chemical Society.

properties, where the influence of the electron tunneling on the coherence needs further investigations.

VII. CONCLUSION AND OUTLOOK

This work has summarized the latest results of electrical and optical measurements on the nonequilibrium charge carrier dynamics in self-assembled InAs/GaAs quantum dots. All-electrical transconductance spectroscopy was used, where a two-dimensional electron gas serves as a fast and sensitive detector for the electron dynamics in an ensemble of quantum dots. Electron tunneling and Auger recombination in a single dot were observed in time-resolved resonance fluorescence.

The self-assembled quantum dots are embedded in a high-electron mobility transistor (HEMT) structure for the electrical measurements in the first part. The electron gas in the transistor serves as both an electron reservoir for charging and discharging the quantum dots and an all-electrical detector. If an electron tunnels into the dot, the charge carrier density in the electron gas is reduced, and hence, the conductance change is measured with a high bandwidth (up to 1 MHz) in a current measurement. Even more, in contrast to static capacitance-voltage measurements, this transient measurement technique can measure the charge carrier dynamics and density of states for very weak coupling between dots and the charge reservoir. This was demonstrated for hole tunneling, where transient times into equilibrium of the order of 60 s were observed. The time evolution of the density of states in an ensemble of quantum dots can be measured from nonequilibrium to equilibrium. In the nonequilibrium situation, the spectral resolution is even at liquid helium temperature high enough to resolve the excited spin and charge configurations of quantum-dot hydrogen and helium artificial atoms. A long spin-relaxation time of $\tau_{rel} = 25\ \mu s$ of the excited two-electron spin triplet state was determined. Moreover, the influence of the shape of the dots on the degeneracy of the p-states and, as a consequence, the electron charging sequence has been verified by observing an asymmetry in the charge relaxation times for charging/discharging the dots.

The simple experimental technique allows many further experiments toward an electrical control and detection of many-particle states for quantum information processing, for instance, quantum states in laterally or vertically coupled dots and preparation of more complex excited many-particle configurations. The spin-relaxation for three- or four-electron configurations and the influence of few-particle interactions on the spin-lifetime could be studied. It is also well known from flash memories that a conductive channel can be very fast (in a quantum dot device, a readout time of 3 ns has been demonstrated in Nowozin *et al.*[13]) and scaled down to feature sizes below 20 nm. In this sense, the electrical measurement technique could be used in the future to measure the time-resolved nonequilibrium transport on a single self-assembled quantum dot. High-temperature (more than 10 K) electrical quantum operations and high-resolution spectroscopy would be possible, providing more insights into few-electron systems with their interactions.

In the second part, single dot resolution has been achieved in a resonance fluorescence measurement, where also the interaction between optical excitation and the single electron dynamics has been studied. In contrast to transport measurements, a relaxation rate is found which can be tuned by the resonant excitation as a consequence of optical blocking, i.e., a reduced tunneling rate when the dot is already occupied with an electron-hole pair. These findings open up a new route to optically tune the tunneling rate between a dot and the charge reservoir, with a time-resolution, which is only limited by the Rabi frequency of the optical transition. The relaxation transients in the optical measurements were achieved by an "n-shot"-integration of many pulse sequences. With a maximum count rate in the resonance fluorescence of more than 10^7/s, fast real-time measurements (bandwidth of more than 100 kHz) of single electron tunneling between the reservoir and the dot (measurements of "quantum jumps" as telegraph noise) are possible in the future. This telegraph noise of quantum jumps in real-time measurement into the s- and p-shells can be analyzed with full-counting statistics, revealing interactions and correlations between the tunneling electrons.[278,279] The time-resolved resonance fluorescence measurements also revealed the Auger-recombination rate in self-assembled quantum dots. An Auger-rate of the order of per microsecond—orders of magnitude smaller than for colloidal dots—has been determined, leading also to a spectral broadening by a factor of two of the trion transition. Self-assembled quantum dots can be used now as a perfect model system to understand the Auger process in a semiconductor nanostructure in more detail, like the size dependence and the influence of the environment (band structure, electron reservoir, and nearby quantum dots).

Finally, as an overall outlook, the combination of both techniques—the electrical transconductance spectroscopy and the time-resolved fluorescence—would lead to a highly versatile experimental tool to study and control quantum states in the solid state. An electrical preparation of nonequilibrium states in combination with an optical manipulation and readout could be used to control quantum bits locally by electrical means and switch-on nonlocal interaction by single photon channels, a step forward to a quantum network.[16]

ACKNOWLEDGMENTS

I would like to thank all those who have contributed to this work. Axel Lorke is gratefully acknowledged for his continuous support and for his inspiring manner in many fruitful discussions. I want to thank all co-workers and collaborators, a large number, where especially the Ph.D. students Annika Kurzmann, Bastian Marquardt, Andreas Beckel, and Kevin Eltrudis did a fabulous job, supported by many master and bachelor students. I like to thank also Jürgen König for his theoretical support, understanding the dynamics in the time-resolved relaxation measurements. Parts of the results here are the outcome of a perfect collaboration with the Technical University of Berlin, where I especially thank Dieter Bimberg and Tobias Nowozin. I want to thank also Mete Atatüre at the University of Cambridge and his group, teaching me the resonance fluorescence; especially Clemens Matthiesen, Claire LeGall, and Carsten Schulte. And, last but not least, I have to thank my colleagues Andreas Wieck and Arne Ludwig at the Ruhr-University of Bochum, for fruitful discussions and a continuous support with perfect quantum dot samples.

I would like to thank also the funding agencies for the financial support: The German Research Foundation in the framework of the NanoSci-E+ Project QD2D, Grant No. GE2141/1-1, as well as within the SFB 1242, Project No. 278162697 (TP A01), the research fellowship No. GE2141/2-1, and the individual research Grant No. GE2141/5-1. I also acknowledge the financial

support through the Project HOFUS (16V0196) within the VIP program of the German Federal Ministry of Education and Research (BMBF).

REFERENCES

[1]M. Grundmann, O. Stier, and D. Bimberg, Phys. Rev. B **52**, 11969 (1995).
[2]D. Bimberg, N. Kirstaedter, N. N. Ledentsov, Z. Alferov, P. S. Kop'ev, and V. M. Ustinov, IEEE J. Sel. Top. Quantum Electron. **3**, 196 (1997).
[3]R. L. Sellin, C. Ribbat, M. Grundmann, N. N. Ledentsov, and D. Bimberg, Appl. Phys. Lett. **78**, 1207 (2001).
[4]C. Ribbat, R. L. Sellin, I. Kaiander, F. Hopfer, N. N. Ledentsov, D. Bimberg, A. R. Kovsh, V. M. Ustinov, A. E. Zhukov, and M. V. Maximov, Appl. Phys. Lett. **82**, 952 (2003).
[5]D. Bimberg and N. Ledentsov, J. Phys.: Condens. Matter **15**, R1063 (2003).
[6]A. J. Zilkie, J. Meier, P. W. E. Smith, M. Mojahedi, J. S. Aitchison, P. J. Poole, C. N. Allen, P. Barrios, and D. Poitras, Opt. Express **14**, 11453 (2006).
[7]J. Park, N. J. Kim, Y. D. Jang, E. G. Lee, J. M. Lee, J. S. Baek, J. H. Kim, H. S. Lee, K. J. Yee, D. Lee, S. H. Pyun, W. G. Jeong, and J. Kim, Appl. Phys. Lett. **98**, 011107 (2011).
[8]S. H. Hwang, J. C. Shin, J. D. Song, W. J. Choi, J. I. Lee, and H. Han, Microelectron. J. **36**, 203 (2005).
[9]P. Martyniuk and A. Rogalski, Prog. Quantum Electron. **32**, 89 (2008).
[10]M. Geller, C. Kapteyn, L. Müller-Kirsch, R. Heitz, and D. Bimberg, Appl. Phys. Lett. **82**, 2706 (2003).
[11]M. Geller, A. Marent, T. Nowozin, D. Bimberg, N. Akçay, and N. Öncan, Appl. Phys. Lett. **92**, 092108 (2008).
[12]T. Nowozin, A. Marent, M. Geller, D. Bimberg, N. Akçay, and N. Öncan, Appl. Phys. Lett. **94**, 042108 (2009).
[13]T. Nowozin, A. Beckel, D. Bimberg, A. Lorke, and M. Geller, Appl. Phys. Lett. **104**, 053111 (2014).
[14]T. D. Ladd, F. Jelezko, R. Laflamme, Y. Nakamura, C. Monroe, and J. L. O'Brien, Nature **464**, 45 (2010).
[15]C. H. Bennett and D. P. DiVincenzo, Nature **404**, 247 (2000).
[16]H. J. Kimble, Nature **453**, 1023 (2008).
[17]D. Kim, A. A. Kiselev, R. S. Ross, M. T. Rakher, C. Jones, and T. D. Ladd, Phys. Rev. Appl. **5**, 024014 (2016).
[18]N. Akopian, N. H. Lindner, E. Poem, Y. Berlatzky, J. Avron, D. Gershoni, B. D. Gerardot, and P. M. Petroff, Phys. Rev. Lett. **96**, 130501 (2006).
[19]R. M. Stevenson, R. J. Young, P. Atkinson, K. Cooper, D. A. Ritchie, and A. J. Shields, Nature **439**, 179 (2006).
[20]V. I. Klimov, *Nanocrystal Quantum Dots*, 2nd ed. (CRC Press, Boca Raton, 2010).
[21]J. M. Pietryga, Y.-S. Park, J. Lim, A. F. Fidler, W. K. Bae, S. Brovelli, and V. I. Klimov, Chem. Rev. **116**, 10513 (2016).
[22]A. T. Johnson, L. P. Kouwenhoven, W. de Jong, N. C. van der Vaart, C. J. P. M. Harmans, and C. T. Foxon, Phys. Rev. Lett. **69**, 1592 (1992).
[23]R. Hanson, L. P. Kouwenhoven, J. R. Petta, S. Tarucha, and L. M. K. Vandersypen, Rev. Mod. Phys. **79**, 1217 (2007).
[24]D. Bimberg, M. Grundmann, and N. N. Ledentsov, *Quantum Dot Heterostructures* (Wiley, Chichester, 2001).
[25]Y. Masumoto, ed., *Semiconductor Quantum Dots: Physics, Spectroscopy and Applications*, Nanoscience and Technology (Springer, Berlin, 2002).
[26]N. G. Semaltianos, S. Logothetidis, W. Perrie, S. Romani, R. J. Potter, M. Sharp, P. French, G. Dearden, and K. G. Watkins, Appl. Phys. A **94**, 641 (2009).
[27]H. Zeng, X.-W. Du, S. C. Singh, S. A. Kulinich, S. Yang, J. He, and W. Cai, Adv. Funct. Mater. **22**, 1333 (2012).
[28]F. Kruis, H. Fissan, and A. Peled, J. Aerosol Sci. **29**, 511 (1998).
[29]A. Lorke, M. Winterer, R. Schmechel, and C. Schulz, *Nanoparticles from the Gasphase: Formation, Structure, Properties*, Nanoscience and Technology (Springer, Berlin, 2012).
[30]B. L. Cushing, V. L. Kolesnichenko, and C. J. O'Connor, Chem. Rev. **104**, 3893 (2004).
[31]W. Lu, Z. Ji, L. Pfeiffer, K. W. West, and A. J. Rimberg, Nature **423**, 422 (2003).
[32]S. Gustavsson, R. Leturcq, M. Studer, I. Shorubalko, T. Ihn, K. Ensslin, D. C. Driscoll, and A. C. Gossard, Surf. Sci. Rep. **64**, 191 (2009).
[33]J. R. Petta, A. C. Johnson, J. M. Taylor, E. A. Laird, A. Yacoby, M. D. Lukin, C. M. Marcus, M. P. Hanson, and A. C. Gossard, Science **309**, 2180 (2005).
[34]F. H. L. Koppens, C. Buizert, K. J. Tielrooij, I. T. Vink, K. C. Nowack, T. Meunier, L. P. Kouwenhoven, and L. M. K. Vandersypen, Nature **442**, 766 (2006).
[35]J. M. Elzerman, R. Hanson, L. H. van Willems Beveren, B. Witkamp, L. M. K. Vandersypen, and L. P. Kouwenhoven, Nature **430**, 431 (2004).
[36]R. Hanson, L. H. W. van Beveren, I. T. Vink, J. M. Elzerman, W. J. M. Naber, F. H. L. Koppens, L. P. Kouwenhoven, and L. M. K. Vandersypen, Phys. Rev. Lett. **94**, 196802 (2005).
[37]R. Held, S. Lüscher, T. Heinzel, K. Ensslin, and W. Wegscheider, Appl. Phys. Lett. **75**, 1134 (1999).
[38]A. Fuhrer, A. Dorn, S. Lüscher, T. Heinzel, K. Ensslin, W. Wegscheider, and M. Bichler, Superlattices Microstruct. **31**, 19 (2002).
[39]S. Gustavsson, R. Leturcq, B. Simovič, R. Schleser, T. Ihn, P. Studerus, K. Ensslin, D. C. Driscoll, and A. C. Gossard, Phys. Rev. Lett. **96**, 076605 (2006).
[40]R. C. Ashoori, Nature **379**, 413 (1996).
[41]L. P. Kouwenhoven, C. M. Marcus, P. L. McEuen, S. Tarucha, R. M. Westervelt, and N. S. Wingreen, *Electron Transport in Quantum Dots*, NATO ASI Series, Series E, Vol. 345 (Springer, Dordrecht, 1997).
[42]M. S. Skolnick and D. J. Mowbray, Annu. Rev. Mater. Res. **34**, 181 (2004).
[43]A. Imamoğlu and Y. Yamamoto, Phys. Rev. Lett. **72**, 210 (1994).
[44]P. P. Paskov, P. O. Holtz, B. Monemar, J. M. Garcia, W. V. Schoenfeld, and P. M. Petroff, Phys. Rev. B **62**, 7344 (2000).
[45]P. Michler, A. Kiraz, L. Zhang, C. Becher, E. Hu, and A. Imamoglu, Appl. Phys. Lett. **77**, 184 (2000).
[46]R. Rinaldi, P. V. Giugno, R. Cingolani, H. Lipsanen, M. Sopanen, J. Tulkki, and J. Ahopelto, Phys. Rev. Lett. **77**, 342 (1996).
[47]M. Bayer, A. Schmidt, A. Forchel, F. Faller, T. L. Reinecke, P. A. Knipp, A. A. Dremin, and V. D. Kulakovskii, Phys. Rev. Lett. **74**, 3439 (1995).
[48]M. Bayer, O. Stern, P. Hawrylak, S. Fafard, and A. Forchel, Nature **405**, 923 (2000).
[49]A. N. Vamivakas, Y. Zhao, C.-Y. Lu, and M. Atatüre, Nat. Phys. **5**, 198 (2009).
[50]C. Matthiesen, M. Geller, C. H. H. Schulte, C. Le Gall, J. Hansom, Z. Li, M. Hugues, E. Clarke, and M. Atatüre, Nat. Commun. **4**, 1600 (2013).
[51]H. Drexler, D. Leonard, W. Hansen, J. P. Kotthaus, and P. M. Petroff, Phys. Rev. Lett. **73**, 2252 (1994).
[52]A. Lorke, R. J. Luyken, A. O. Govorov, J. P. Kotthaus, J. M. Garcia, and P. M. Petroff, Phys. Rev. Lett. **84**, 2223 (2000).
[53]D. Reuter, P. Kailuweit, A. D. Wieck, U. Zeitler, O. Wibbelhoff, C. Meier, A. Lorke, and J. C. Maan, Phys. Rev. Lett. **94**, 026808 (2005).
[54]P. A. Labud, A. Ludwig, A. D. Wieck, G. Bester, and D. Reuter, Phys. Rev. Lett. **112**, 046803 (2014).
[55]R. Bratschitsch and A. Leitenstorfer, Nat. Mater. **5**, 855 (2006).
[56]A. J. Ramsay, Semicond. Sci. Technol. **25**, 103001 (2010).
[57]A. Beveratos, I. Abram, J.-M. Gérard, and I. Robert-Philip, Eur. Phys. J. D **68**, 377 (2014).
[58]A. Muller, E. B. Flagg, P. Bianucci, X. Y. Wang, D. G. Deppe, W. Ma, J. Zhang, G. J. Salamo, M. Xiao, and C. K. Shih, Phys. Rev. Lett. **99**, 187402 (2007).
[59]R. Melet, V. Voliotis, A. Enderlin, D. Roditchev, X. L. Wang, T. Guillet, and R. Grousson, Phys. Rev. B **78**, 073301 (2008).
[60]C. Matthiesen, A. N. Vamivakas, and M. Atatüre, Phys. Rev. Lett. **108**, 093602 (2012).
[61]A. V. Kuhlmann, J. Houel, A. Ludwig, L. Greuter, D. Reuter, A. D. Wieck, M. Poggio, and R. J. Warburton, Nat. Phys. **9**, 570 (2013).
[62]M. Grundmann, *The Physics of Semiconductors: An Introduction Including Nanophysics and Applications*, 3rd ed. (Springer, 2016).
[63]J. H. Davies, *The Physics of Low-Dimensional Semiconductors: An Introduction* (Cambridge University Press, 2009).
[64]T. Heinzel and I. Zozoulenko, *Mesoscopic Electronics in Solid State Nanostructures*, 3rd ed. (Wiley-VCH Verlag, Weinheim, 2010).
[65]T. Ihn, *Semiconductor Nanostructures: Quantum States and Electronic Transport*, 1st ed. (Oxford University Press, 2013).

[66]U. Woggon, *Optical Properties of Semiconductor Quantum Dots*, Springer Tracts in Modern Physics, Vol. 136 (Springer, Berlin, 1997).
[67]P. M. Petroff, A. Lorke, and A. Imamoglu, Phys. Today **54**(5), 46 (2001).
[68]I. Vurgaftman, J. R. Meyer, and L. R. Ram-Mohan, J. Appl. Phys. **89**, 5815 (2001).
[69]M. A. Herman, W. Richter, and H. Sitter, *Epitaxy: Physical Principles and Technical Implementation*, Springer Series in Material Science Vol. 62 (Springer, Berlin and Heidelberg, 2004).
[70]P. D. Dapkus, Annu. Rev. Mater. Sci. **12**, 243 (1982).
[71]B. A. Joyce, Rep. Prog. Phys. **48**, 1637 (1985).
[72]M. J. Kelly, *Low-Dimensional Semiconductors: Materials, Physics, Technology, Devices*, Series on Semiconductor Science and Technology Vol. 3 (Clarendon Press, Oxford, 1995).
[73]T. Ando, A. B. Fowler, and F. Stern, Rev. Mod. Phys. **54**, 437 (1982).
[74]H. L. Störmer and W.-T. Tsang, Appl. Phys. Lett. **36**, 685 (1980).
[75]K. v Klitzing, G. Dorda, and M. Pepper, Phys. Rev. Lett. **45**, 494 (1980).
[76]A. K. Geim and K. S. Novoselov, Nat. Mater. **6**, 183 (2007).
[77]A. Kumar, G. A. Csathy, M. J. Manfra, L. N. Pfeiffer, and K. W. West, Phys. Rev. Lett. **105**, 246808 (2010).
[78]A. Pinczuk, J. M. Worlock, H. L. Störmer, R. Dingle, W. Wiegmann, and A. C. Gossard, Solid State Commun. **36**, 43 (1980).
[79]J. R. Arthur, Surf. Sci. **500**, 189 (2002).
[80]G. B. Stringfellow, *Organometallic Vapor-Phase Epitaxy: Theory and Practice*, 2nd ed. (Academic Press, San Diego, CA, 1999).
[81]I. N. Stranski and L. Krastanow, "Abhandlungen der Mathematisch-Naturwissenschaftlichen Klasse IIb," Akad. Wiss. Wien **146**, 797 (1938).
[82]O. Wibbelhoff, "Ladungsträgerquantisierung in selbstorganisierten Nanostrukturen," Ph.D. thesis (University of Duisburg-Essen, 2006).
[83]R. J. Warburton, C. Schäflein, D. Haft, F. Bickel, A. Lorke, K. Karrai, J. M. M. Garcia, W. Schoenfeld, and P. M. Petroff, Nature **405**, 926 (2000).
[84]M. Fricke, A. Lorke, J. P. Kotthaus, G. Medeiros-Ribeiro, and P. M. Petroff, Europhys. Lett. **36**, 197 (1996).
[85]R. J. Warburton, B. T. Miller, C. S. Dürr, C. Bödefeld, K. Karrai, J. P. Kotthaus, G. Medeiros-Ribeiro, P. M. Petroff, and S. Huant, Phys. Rev. B **58**, 16221 (1998).
[86]B. T. Miller, W. Hansen, S. Manus, R. J. Luyken, A. Lorke, J. P. Kotthaus, S. Huant, G. Medeiros-Ribeiro, and P. M. Petroff, Phys. Rev. B **56**, 6764 (1997).
[87]M. Russ, C. Meier, A. Lorke, D. Reuter, and A. D. Wieck, Phys. Rev. B **73**, 115334 (2006).
[88]B. Marquardt, M. Russ, A. Lorke, C. Meier, D. Reuter, and A. D. Wieck, Physica E **40**, 2075 (2008).
[89]B. Marquardt, M. Geller, B. Baxevanis, D. Pfannkuche, A. D. Wieck, D. Reuter, and A. Lorke, Nat. Commun. **2**, 209 (2011).
[90]A. Kurzmann, A. Beckel, A. Ludwig, A. D. Wieck, A. Lorke, and M. Geller, J. Appl. Phys. **117**, 054305 (2015).
[91]E. Ribeiro, E. Müller, T. Heinzel, H. Auderset, K. Ensslin, G. Medeiros-Ribeiro, and P. M. Petroff, Phys. Rev. B **58**, 1506 (1998).
[92]H.-Z. Song, S. Lan, K. Akahane, K.-Y. Jang, Y. Okada, and M. Kawabe, Jpn. J. Appl. Phys. **39**, 5746 (2000).
[93]G. Li, H. Yin, Q. Zhu, H. Sakaki, and C. Jiang, J. Appl. Phys. **108**, 043702 (2010).
[94]G. Medeiros-Ribeiro, F. G. Pikus, P. M. Petroff, and A. L. Efros, Phys. Rev. B **55**, 1568 (1997).
[95]R. J. Luyken, A. Lorke, A. O. Govorov, J. P. Kotthaus, G. Medeiros-Ribeiro, and P. M. Petroff, Appl. Phys. Lett. **74**, 2486 (1999).
[96]M. Russ, C. Meier, B. Marquardt, A. Lorke, D. Reuter, and A. D. Wieck, Phase Transitions **79**, 765 (2006).
[97]C. Kittel, *Introduction to Solid State Physics*, 8th ed. (Wiley, Hoboken, NJ, 2005).
[98]N. W. Ashcroft and N. D. Mermin, *Solid State Physics*, 33rd ed. (Thomson Brooks/Cole, Singapore, 2006).
[99]O. Stier, M. Grundmann, and D. Bimberg, Phys. Rev. B **59**, 5688 (1999).
[100]A. Schliwa, M. Winkelnkemper, and D. Bimberg, Phys. Rev. B **76**, 205324 (2007).
[101]A. Franceschetti and A. Zunger, Phys. Rev. Lett. **78**, 915 (1997).
[102]G. Bester, S. Nair, and A. Zunger, Phys. Rev. B **67**, 161306 (2003).
[103]J.-Y. Marzin and G. Bastard, Solid State Commun. **92**, 437 (1994).
[104]P. Hawrylak, Phys. Rev. Lett. **71**, 3347 (1993).
[105]A. Wojs, P. Hawrylak, S. Fafard, and L. Jacak, Phys. Rev. B **54**, 5604 (1996).
[106]K. Teichmann, M. Wenderoth, H. Pruser, K. Pierz, H. W. Schumacher, and R. G. Ulbrich, Nano Lett. **13**, 3571 (2013).
[107]A. Lenz, R. Timm, H. Eisele, C. Hennig, S. K. Becker, R. L. Sellin, U. W. Pohl, D. Bimberg, and M. Dähne, Appl. Phys. Lett. **81**, 5150 (2002).
[108]H. Eisele, A. Lenz, C. Hennig, R. Timm, M. Ternes, and M. Dähne, J. Cryst. Growth **248**, 322 (2003).
[109]B. J. Riel, Am. J. Phys. **76**, 750 (2008).
[110]C. Cohen-Tannoudji, B. Diu, and F. Laloë, *Quantum Mechanics*, Textbook Physics (Wiley, New York, NY, 2005).
[111]D. Zhou and A. Lorke, Am. J. Phys. **83**, 205 (2015).
[112]V. Fock, Z. Phys. **47**, 446 (1928).
[113]C. G. Darwin, Math. Proc. Cambridge Philos. Soc. **27**, 86 (1931).
[114]A. Wojs and P. Hawrylak, Phys. Rev. B **55**, 13066 (1997).
[115]S. M. Sze and K. K. Ng, *Physics of Semiconductor Devices*, 3rd ed. (Wiley, 2007).
[116]D. V. Lang, J. Appl. Phys. **45**, 3023 (1974).
[117]J. J. Orton and P. Blood, *The Electrical Characterization of Semiconductors: Measurement of Minority Carrier Properties*, Techniques of Physics, Vol. 13 (Academy PR, London, 1990).
[118]C. M. A. Kapteyn, F. Heinrichsdorff, O. Stier, R. Heitz, M. Grundmann, N. D. Zakharov, D. Bimberg, and P. Werner, Phys. Rev. B **60**, 14265 (1999).
[119]M. Geller, E. Stock, C. Kapteyn, R. Sellin, and D. Bimberg, Phys. Rev. B **73**, 205331 (2006).
[120]M. Geller, A. Marent, E. Stock, D. Bimberg, V. I. Zubkov, I. S. Shulgunova, and A. V. Solomonov, Appl. Phys. Lett. **89**, 232105 (2006).
[121]O. Engström, M. Kaniewska, M. Kaczmarczyk, and W. Jung, Appl. Phys. Lett. **91**, 133117 (2007).
[122]B. Miller, W. Hansen, S. Manus, R. Luyken, A. Lorke, J. Kotthaus, G. Medeiros-Ribeiro, and P. Petroff, Phys. B: Condens. Matter **249**, 257 (1998).
[123]H. Lipsanen, M. Sopanen, and J. Ahopelto, Phys. Rev. B **51**, 13868 (1995).
[124]R. Heitz, O. Stier, I. Mukhametzhanov, A. Madhukar, and D. Bimberg, Phys. Rev. B **62**, 11017 (2000).
[125]R. Heitz, M. Grundmann, N. N. Ledentsov, L. Eckey, M. Veit, D. Bimberg, V. M. Ustinov, A. Y. Egorov, A. E. Zhukov, P. S. Kop'ev, and Z. I. Alferov, Appl. Phys. Lett. **68**, 361 (1996).
[126]K. H. Schmidt, G. Medeiros-Ribeiro, M. Oestreich, P. M. Petroff, and G. H. Döhler, Phys. Rev. B **54**, 11346 (1996).
[127]M. J. Steer, D. J. Mowbray, W. R. Tribe, M. S. Skolnick, M. D. Sturge, M. Hopkinson, A. G. Cullis, C. R. Whitehouse, and R. Murray, Phys. Rev. B **54**, 17738 (1996).
[128]H. Kurtze, J. Seebeck, P. Gartner, D. R. Yakovlev, D. Reuter, A. D. Wieck, M. Bayer, and F. Jahnke, Phys. Rev. B **80**, 235319 (2009).
[129]K. Brunner, U. Bockelmann, G. Abstreiter, M. Walther, G. Böhm, G. Tränkle, and G. Weimann, Phys. Rev. Lett. **69**, 3216 (1992).
[130]E. Dekel, D. Gershoni, E. Ehrenfreund, D. Spektor, J. M. Garcia, and P. M. Petroff, Phys. Rev. Lett. **80**, 4991 (1998).
[131]M. Bayer, G. Ortner, O. Stern, A. Kuther, A. A. Gorbunov, A. Forchel, P. Hawrylak, S. Fafard, K. Hinzer, T. L. Reinecke, S. N. Walck, J. P. Reithmaier, F. Klopf, and F. Schäfer, Phys. Rev. B **65**, 195315 (2002).
[132]G. Chen, N. H. Bonadeo, D. G. Steel, D. Gammon, D. S. Katzer, D. Park, and L. J. Sham, Science **289**, 1906 (2000).
[133]N. H. Bonadeo, G. Chen, D. Gammon, D. S. Katzer, D. Park, and D. G. Steel, Phys. Rev. Lett. **81**, 2759 (1998).
[134]M. Borgstrom, T. Bryllert, B. Gustafson, J. Johansson, T. Sass, L. E. Wernersson, W. Seifert, and L. Samuelson, J. Electron. Mater. **30**, 482 (2001).
[135]R. Songmuang, S. Kiravittaya, and O. G. Schmidt, Appl. Phys. Lett. **82**, 2892 (2003).
[136]M. Mehta, D. Reuter, A. Melnikov, A. D. Wieck, and A. Remhof, Appl. Phys. Lett. **91**, 123108 (2007).
[137]J. Tommila, A. Tukiainen, J. Viheriälä, A. Schramm, T. Hakkarainen, A. Aho, P. Stenberg, M. Dumitrescu, and M. Guina, J. Cryst. Growth **323**, 183 (2011).
[138]S. Kiravittaya, A. Rastelli, and O. G. Schmidt, Rep. Prog. Phys. **72**, 046502 (2009).
[139]O. G. Schmidt, *Lateral Alignment of Epitaxial Quantum Dots*, Nanoscience and Technology (Springer-Verlag, Berlin, Heidelberg, 2007).

[140]A. Strittmatter, A. Holzbecher, A. Schliwa, J.-H. Schulze, D. Quandt, T. D. Germann, A. Dreismann, O. Hitzemann, E. Stock, I. A. Ostapenko, S. Rodt, W. Unrau, U. W. Pohl, A. Hoffmann, D. Bimberg, and V. Haisler, Phys. Status Solidi **209**, 2411 (2012).
[141]A. Strittmatter, A. Schliwa, J. H. Schulze, T. D. Germann, A. Dreismann, O. Hitzemann, E. Stock, I. A. Ostapenko, S. Rodt, W. Unrau, U. W. Pohl, A. Hoffmann, D. Bimberg, and V. Haisler, Appl. Phys. Lett. **100**, 093111 (2012).
[142]C. Schneider, A. Huggenberger, T. Sunner, T. Heindel, M. Strauss, S. Gopfert, P. Weinmann, S. Reitzenstein, L. Worschech, M. Kamp, S. Hofling, and A. Forchel, Nanotechnology **20**, 434012 (2009).
[143]L. H. Li, N. Chauvin, G. Patriarche, B. Alloing, and A. Fiore, J. Appl. Phys. **104**, 083508 (2008).
[144]S. J. Xu, X. C. Wang, S. J. Chua, C. H. Wang, W. J. Fan, J. Jiang, and X. G. Xie, Appl. Phys. Lett. **72**, 3335 (1998).
[145]A. Babiński, J. Jasiński, R. Bożek, A. Szepielow, and J. M. Baranowski, Appl. Phys. Lett. **79**, 2576 (2001).
[146]W. Langbein, P. Borri, U. Woggon, V. Stavarache, D. Reuter, and A. D. Wieck, Phys. Rev. B **69**, 161301(R) (2004).
[147]H. Sasakura, S. Kayamori, S. Adachi, and S. Muto, J. Appl. Phys. **102**, 013515 (2007).
[148]N. Kumagai, S. Ohkouchi, M. Shirane, Y. Igarashi, M. Nomura, Y. Ota, S. Yorozu, S. Iwamoto, and Y. Arakawa, Phys. Status Solidi C **8**, 248 (2011).
[149]D. Pfannkuche, V. Gudmundsson, and P. A. Maksym, Phys. Rev. B **47**, 2244 (1993).
[150]R. J. Young, R. M. Stevenson, A. J. Shields, P. Atkinson, K. Cooper, D. A. Ritchie, K. M. Groom, A. I. Tartakovskii, and M. S. Skolnick, Phys. Rev. B **72**, 113305 (2005).
[151]J. J. Finley, A. d Ashmore, A. Lemaître, D. J. Mowbray, M. S. Skolnick, I. E. Itskevich, P. A. Maksym, M. Hopkinson, and T. F. Krauss, Phys. Rev. B **63**, 073307 (2001).
[152]V. Jovanov, S. Kapfinger, M. Bichler, G. Abstreiter, and J. J. Finley, Phys. Rev. B **84**, 235321 (2011).
[153]S.-S. Li and J.-B. Xia, J. Appl. Phys. **88**, 7171 (2000).
[154]P. W. Fry, I. E. Itskevich, D. J. Mowbray, M. S. Skolnick, J. J. Finley, J. A. Barker, E. P. O'Reilly, L. R. Wilson, I. A. Larkin, P. A. Maksym, M. Hopkinson, M. Al-Khafaji, J. P. David, A. G. Cullis, G. Hill, and J. C. Clark, Phys. Rev. Lett. **84**, 733 (2000).
[155]J. J. Finley, M. Sabathil, P. Vogl, G. Abstreiter, R. Oulton, A. I. Tartakovskii, D. J. Mowbray, M. S. Skolnick, S. L. Liew, A. G. Cullis, and M. Hopkinson, Phys. Rev. B **70**, 201308(R) (2004).
[156]P. Michler, *Quantum Dots for Quantum Information Technologies* (Springer International Publishing, Cham, 2017).
[157]O. Gazzano and G. S. Solomon, J. Opt. Soc. Am. B **33**, C160 (2016).
[158]D. D. Awschalom, R. Hanson, J. Wrachtrup, and B. B. Zhou, Nat. Photonics **12**, 516 (2018).
[159]P. Michler, A. Kiraz, C. Becher, W. V. Schoenfeld, P. M. Petroff, L. Zhang, E. Hu, and A. Imamoğlu, Science **290**, 2282 (2000).
[160]E. B. Flagg, S. V. Polyakov, T. Thomay, and G. S. Solomon, Phys. Rev. Lett. **109**, 163601 (2012).
[161]V. Giesz, O. Gazzano, A. K. Nowak, S. L. Portalupi, A. Lemaître, I. Sagnes, L. Lanco, and P. Senellart, Appl. Phys. Lett. **103**, 033113 (2013).
[162]P. Senellart, G. Solomon, and A. White, Nat. Nanotechnol. **12**, 1026 (2017).
[163]C. Santori, D. Fattal, J. Vucković, G. S. Solomon, and Y. Yamamoto, Nature **419**, 594 (2002).
[164]S. Laurent, S. Varoutsis, L. Le Gratiet, A. Lemaître, I. Sagnes, F. Raineri, A. Levenson, I. Robert-Philip, and I. Abram, Appl. Phys. Lett. **87**, 163107 (2005).
[165]K. D. Jöns, P. Atkinson, M. Müller, M. Heldmaier, S. M. Ulrich, O. G. Schmidt, and P. Michler, Nano Lett. **13**, 126 (2013).
[166]N. Somaschi, V. Giesz, L. de Santis, J. C. Loredo, M. P. Almeida, G. Hornecker, S. L. Portalupi, T. Grange, C. Antón, J. Demory, C. Gómez, I. Sagnes, N. D. Lanzillotti-Kimura, A. Lemaître, A. Auffeves, A. G. White, L. Lanco, and P. Senellart, Nat. Photonics **10**, 340 (2016).
[167]D. Huber, M. Reindl, Y. Huo, H. Huang, J. S. Wildmann, O. G. Schmidt, A. Rastelli, and R. Trotta, Nat. Commun. **8**, 15506 (2017).
[168]J. Berezovsky, M. H. Mikkelsen, O. Gywat, N. G. Stoltz, L. A. Coldren, and D. D. Awschalom, Science **314**, 1916 (2006).
[169]M. H. Mikkelsen, J. Berezovsky, N. G. Stoltz, L. A. Coldren, and D. D. Awschalom, Nat. Phys. **3**, 770 (2007).
[170]X. Xu, Y. Wu, B. Sun, Q. Huang, J. Cheng, D. G. Steel, A. S. Bracker, D. Gammon, C. Emary, and L. J. Sham, Phys. Rev. Lett. **99**, 097401 (2007).
[171]X. Xu, B. Sun, P. R. Berman, D. G. Steel, A. S. Bracker, D. Gammon, and L. J. Sham, Nat. Phys. **4**, 692 (2008).
[172]J. Berezovsky, M. H. Mikkelsen, N. G. Stoltz, L. A. Coldren, and D. D. Awschalom, Science **320**, 349 (2008).
[173]E. D. Kim, K. Truex, X. Xu, B. Sun, D. G. Steel, A. S. Bracker, D. Gammon, and L. J. Sham, Phys. Rev. Lett. **104**, 167401 (2010).
[174]D. Kim, S. G. Carter, A. Greilich, A. S. Bracker, and D. Gammon, Nat. Phys. **7**, 223 (2011).
[175]W. B. Gao, P. Fallahi, E. Togan, J. Miguel-Sanchez, and A. Imamoğlu, Nature **491**, 426 (2012).
[176]I. J. Luxmoore, N. A. Wasley, A. J. Ramsay, A. C. T. Thijssen, R. Oulton, M. Hugues, S. Kasture, V. G. Achanta, A. M. Fox, and M. S. Skolnick, Phys. Rev. Lett. **110**, 037402 (2013).
[177]A. Delteil, Z. Sun, W.-B. Gao, E. Togan, S. Faelt, and A. Imamoğlu, Nat. Phys. **12**, 218 (2016).
[178]A. Javadi, D. Ding, M. H. Appel, S. Mahmoodian, M. C. Löbl, I. Söllner, R. Schott, C. Papon, T. Pregnolato, S. Stobbe, L. Midolo, T. Schröder, A. D. Wieck, A. Ludwig, R. J. Warburton, and P. Lodahl, Nat. Nanotechnol. **13**, 398 (2018).
[179]A. Laucht, S. Pütz, T. Günthner, N. Hauke, R. Saive, S. Frédérick, M. Bichler, M.-C. Amann, A. W. Holleitner, M. Kaniber, and J. J. Finley, Phys. Rev. X **2**, 011014 (2012).
[180]A. Kress, F. Hofbauer, N. Reinelt, M. Kaniber, H. J. Krenner, R. Meyer, G. Böhm, and J. J. Finley, Phys. Rev. B **71**, 241304 (2005).
[181]U. Hohenester, A. Laucht, M. Kaniber, N. Hauke, A. Neumann, A. Mohtashami, M. Seliger, M. Bichler, and J. J. Finley, Phys. Rev. B **80**, 201311 (2009).
[182]E. M. Purcell, H. C. Torrey, and R. V. Pound, Phys. Rev. **69**, 37 (1946).
[183]A. Kiraz, P. Michler, C. Becher, B. Gayral, A. Imamoğlu, L. Zhang, E. Hu, W. V. Schoenfeld, and P. M. Petroff, Appl. Phys. Lett. **78**, 3932 (2001).
[184]S. Ates, S. M. Ulrich, S. Reitzenstein, A. Löffler, A. Forchel, and P. Michler, Phys. Rev. Lett. **103**, 167402 (2009).
[185]A. Dousse, L. Lanco, J. Suffczyński, E. Semenova, A. Miard, A. Lemaître, I. Sagnes, C. Roblin, J. Bloch, and P. Senellart, Phys. Rev. Lett. **101**, 267404 (2008).
[186]A. Dousse, J. Suffczyński, A. Beveratos, O. Krebs, A. Lemaître, I. Sagnes, J. Bloch, P. Voisin, and P. Senellart, Nature **466**, 217 (2010).
[187]J. P. Reithmaier, G. Sek, A. Löffler, C. Hofmann, S. Kuhn, S. Reitzenstein, L. V. Keldysh, V. D. Kulakovskii, T. L. Reinecke, and A. Forchel, Nature **432**, 197 (2004).
[188]E. Peter, P. Senellart, D. Martrou, A. Lemaitre, J. Hours, J. M. Gérard, and J. Bloch, Phys. Rev. Lett. **95**, 067401 (2005).
[189]D. Press, S. Götzinger, S. Reitzenstein, C. Hofmann, A. Löffler, M. Kamp, A. Forchel, and Y. Yamamoto, Phys. Rev. Lett. **98**, 117402 (2007).
[190]S. Ates, S. M. Ulrich, A. Ulhaq, S. Reitzenstein, A. Löffler, S. Höfling, A. Forchel, and P. Michler, Nat. Photonics **3**, 724 (2009).
[191]A. Högele, S. Seidl, M. Kroner, K. Karrai, R. J. Warburton, B. D. Gerardot, and P. M. Petroff, Phys. Rev. Lett. **93**, 217401 (2004).
[192]M. O. Scully and M. S. Zubairy, *Quantum Optics* (Cambridge University Press, Cambridge, 1997).
[193]M. Fox, *Quantum Optics: An Introduction*, reprint ed., Oxford Master Series in Physics Vol. 15 (Oxford University Press, Oxford, 2010).
[194]R. Loudon, *The Quantum Theory of Light*, 3rd ed., Oxford Science Publications (Oxford University Press, Oxford, 2010).
[195]K. Karrai and R. J. Warburton, Superlattices Microstruct. **33**, 311 (2003).
[196]B. Alen, F. Bickel, K. Karrai, R. J. Warburton, and P. M. Petroff, Appl. Phys. Lett. **83**, 2235 (2003).
[197]B. Alen, A. Högele, M. Kroner, S. Seidl, K. Karrai, R. J. Warburton, A. Badolato, G. Medeiros-Ribeiro, and P. M. Petroff, Appl. Phys. Lett. **89**, 123124 (2006).
[198]A. N. Vamivakas, M. Atatüre, J. Dreiser, S. T. Yilmaz, A. Badolato, A. K. Swan, B. B. Goldberg, A. Imamoğlu, and M. S. Unlu, Nano Lett. **7**, 2892 (2007).
[199]C. M. Chow, A. M. Ross, D. Kim, D. Gammon, A. S. Bracker, L. J. Sham, and D. G. Steel, Phys. Rev. Lett. **117**, 077403 (2016).

[200]M. L. Citron, H. R. Gray, C. W. Gabel, and C. R. Stroud, Phys. Rev. A **16**, 1507 (1977).
[201]K. Kuroda, T. Kuroda, K. Watanabe, T. Mano, K. Sakoda, G. Kido, and N. Koguchi, Appl. Phys. Lett. **90**, 051909 (2007).
[202]E. B. Flagg, A. Muller, J. W. Robertson, S. Founta, D. G. Deppe, M. Xiao, W. Ma, G. J. Salamo, and C. K. Shih, Nat. Phys. **5**, 203 (2009).
[203]S. T. Y. ilmaz, P. Fallahi, and A. Imamoğlu, Phys. Rev. Lett. **105**, 033601 (2010).
[204]P. Fallahi, S. T. Yilmaz, and A. Imamoğlu, Phys. Rev. Lett. **105**, 257402 (2010).
[205]A. V. Kuhlmann, J. Houel, D. Brunner, A. Ludwig, D. Reuter, A. D. Wieck, and R. J. Warburton, Rev. Sci. Instrum. **84**, 073905 (2013).
[206]L. Allen and J. H. Eberly, *Optical Resonance and Two-Level Atoms*, Dover Books on Physics (Dover Publications, Newburyport, 2012).
[207]P. K. Pathak and S. Hughes, Phys. Rev. B **82**, 045308 (2010).
[208]T. H. Stievater, X. Li, D. G. Steel, D. Gammon, D. S. Katzer, D. Park, C. Piermarocchi, and L. J. Sham, Phys. Rev. Lett. **87**, 133603 (2001).
[209]J. R. Schaibley, A. P. Burgers, G. A. McCracken, D. G. Steel, A. S. Bracker, D. Gammon, and L. J. Sham, Phys. Rev. B **87**, 115311 (2013).
[210]A. Ulhaq, S. Weiler, S. M. Ulrich, R. Roßbach, M. Jetter, and P. Michler, Nat. Photonics **6**, 238 (2012).
[211]W. B. Gao, P. Fallahi, E. Togan, A. Delteil, Y. S. Chin, J. Miguel-Sanchez, and A. Imamoğlu, Nat. Commun. **4**, 2744 (2013).
[212]M. Prilmüller, T. Huber, M. Müller, P. Michler, G. Weihs, and A. Predojević, Phys. Rev. Lett. **121**, 110503 (2018).
[213]C. H. H. Schulte, J. Hansom, A. E. Jones, C. Matthiesen, C. Le Gall, and M. Atatüre, Nature **525**, 222 (2015).
[214]A. Zrenner, E. Beham, S. Stufler, F. Findeis, M. Bichler, and G. Abstreiter, Nature **418**, 612 (2002).
[215]F. Bloch, W. W. Hansen, and M. Packard, Phys. Rev. **70**, 474 (1946).
[216]J. Houel, A. V. Kuhlmann, L. Greuter, F. Xue, M. Poggio, B. D. Gerardot, P. A. Dalgarno, A. Badolato, P. M. Petroff, A. Ludwig, D. Reuter, A. D. Wieck, and R. J. Warburton, Phys. Rev. Lett. **108**, 107401 (2012).
[217]A. V. Kuhlmann, J. H. Prechtel, J. Houel, A. Ludwig, D. Reuter, A. D. Wieck, and R. J. Warburton, Nat. Commun. **6**, 8204 (2015).
[218]C. Latta, A. Högele, Y. Zhao, A. N. Vamivakas, P. Maletinsky, M. Kroner, J. Dreiser, I. Carusotto, A. Badolato, D. Schuh, W. Wegscheider, M. Atatüre, and A. Imamoğlu, Nat. Phys. **5**, 758 (2009).
[219]M. Munsch, G. Wüst, A. V. Kuhlmann, F. Xue, A. Ludwig, D. Reuter, A. D. Wieck, M. Poggio, and R. J. Warburton, Nat. Nanotechnol. **9**, 671 (2014).
[220]G. Wüst, M. Munsch, F. Maier, A. V. Kuhlmann, A. Ludwig, A. D. Wieck, D. Loss, M. Poggio, and R. J. Warburton, Nat. Nanotechnol. **11**, 885 (2016).
[221]J. Hansom, C. H. H. Schulte, C. Matthiesen, M. J. Stanley, and M. Atatüre, Appl. Phys. Lett. **105**, 172107 (2014).
[222]D. Gammon, E. S. Snow, B. V. Shanabrook, D. S. Katzer, and D. Park, Phys. Rev. Lett. **76**, 3005 (1996).
[223]R. Seguin, A. Schliwa, S. Rodt, K. Pötschke, U. W. Pohl, and D. Bimberg, Phys. Rev. Lett. **95**, 257402 (2005).
[224]M. E. Ware, E. A. Stinaff, D. Gammon, M. F. Doty, A. S. Bracker, D. Gershoni, V. L. Korenev, S. C. Bdescu, Y. Lyanda-Geller, and T. L. Reinecke, Phys. Rev. Lett. **95**, 177403 (2005).
[225]F. Ding, R. Singh, J. D. Plumhof, T. Zander, V. Křápek, Y. H. Chen, M. Benyoucef, V. Zwiller, K. Dörr, G. Bester, A. Rastelli, and O. G. Schmidt, Phys. Rev. Lett. **104**, 067405 (2010).
[226]R. Trotta, E. Zallo, C. Ortix, P. Atkinson, J. D. Plumhof, J. van den Brink, A. Rastelli, and O. G. Schmidt, Phys. Rev. Lett. **109**, 147401 (2012).
[227]S. Wehner, D. Elkouss, and R. Hanson, Science **362**, 9288 (2018).
[228]P. Pavan, R. Bez, P. Olivo, and E. Zanoni, Proc. IEEE **85**, 1248 (1997).
[229]A. Marent, M. Geller, A. Schliwa, D. Feise, K. Pötschke, D. Bimberg, N. Akçay, and N. Öncan, Appl. Phys. Lett. **91**, 242109 (2007).
[230]A. Marent, M. Geller, and D. Bimberg, Microelectron. J. **40**, 492 (2009).
[231]T. Nowozin, A. Marent, G. Hönig, A. Schliwa, D. Bimberg, A. Beckel, B. Marquardt, A. Lorke, and M. Geller, Phys. Rev. B **84**, 075309 (2011).
[232]B. Marquardt, A. Beckel, A. Lorke, A. D. Wieck, D. Reuter, and M. Geller, Appl. Phys. Lett. **99**, 223510 (2011).
[233]A. Beckel, A. Ludwig, A. D. Wieck, A. Lorke, and M. Geller, Phys. Rev. B **89**, 155430 (2014).
[234]B. Marquardt, M. Geller, A. Lorke, D. Reuter, and A. D. Wieck, Appl. Phys. Lett. **95**, 022113 (2009).
[235]T. Nowozin, A. Marent, D. Bimberg, A. Beckel, B. Marquardt, A. Lorke, and M. Geller, Phys. Status Solidi C **9**, 243 (2012).
[236]G. Vincent, A. Chantre, and D. Bois, J. Appl. Phys. **50**, 5484 (1979).
[237]A. Beckel, A. Kurzmann, M. Geller, A. Ludwig, A. D. Wieck, J. König, and A. Lorke, Europhys. Lett. **106**, 47002 (2014).
[238]T. Koppen, D. Franz, A. Schramm, C. Heyn, D. Heitmann, and T. Kipp, Phys. Rev. Lett. **103**, 037402 (2009).
[239]J. R. Prance, Z. Shi, C. B. Simmons, D. E. Savage, M. G. Lagally, L. R. Schreiber, L. M. K. Vandersypen, M. Friesen, R. Joynt, S. N. Coppersmith, and M. A. Eriksson, Phys. Rev. Lett. **108**, 046808 (2012).
[240]A. Steinhoff, H. Kurtze, P. Gartner, M. Florian, D. Reuter, A. D. Wieck, M. Bayer, and F. Jahnke, Phys. Rev. B **88**, 205309 (2013).
[241]H. Kurtze and M. Bayer, Appl. Phys. Lett. **109**, 012103 (2016).
[242]G. A. Narvaez, G. Bester, and A. Zunger, Phys. Rev. B **74**, 075403 (2006).
[243]T. Müller, F. F. Schrey, G. Strasser, and K. Unterrainer, Appl. Phys. Lett. **83**, 3572 (2003).
[244]K. Eltrudis, A. Al-Ashouri, A. Beckel, A. Ludwig, A. D. Wieck, M. Geller, and A. Lorke, Appl. Phys. Lett. **111**, 092103 (2017).
[245]Y. Benny, R. Presman, Y. Kodriano, E. Poem, D. Gershoni, T. A. Truong, and P. M. Petroff, Phys. Rev. B **89**, 035316 (2014).
[246]A. C. Johnson, J. R. Petta, J. M. Taylor, A. Yacoby, M. D. Lukin, C. M. Marcus, M. P. Hanson, and A. C. Gossard, Nature **435**, 925 (2005).
[247]M. Kroutvar, Y. Ducommun, D. Heiss, M. Bichler, D. Schuh, G. Abstreiter, and J. J. Finley, Nature **432**, 81 (2004).
[248]S. Amasha, K. Maclean, I. P. Radu, D. M. Zumbuhl, M. A. Kastner, M. P. Hanson, and A. C. Gossard, Phys. Rev. Lett. **100**, 046803 (2008).
[249]H. Wei, M. Gong, G.-C. Guo, and L. He, Phys. Rev. B **85**, 045317 (2012).
[250]H. Wei, G.-C. Guo, and L. He, Phys. Rev. B **89**, 245305 (2014).
[251]R. Dahbashi, J. Hubner, F. Berski, K. Pierz, and M. Oestreich, Phys. Rev. Lett. **112**, 156601 (2014).
[252]C.-Y. Lu, Y. Zhao, A. N. Vamivakas, C. Matthiesen, S. Fält, A. Badolato, and M. Atatüre, Phys. Rev. B **81**, 035332 (2010).
[253]F. Fras, B. Eble, P. Desfonds, F. Bernardot, C. Testelin, M. Chamarro, A. Miard, and A. Lemaître, Phys. Rev. B **86**, 045306 (2012).
[254]F. Sotier, T. Thomay, T. Hanke, J. Korger, S. Mahapatra, A. Frey, K. Brunner, R. Bratschitsch, and A. Leitenstorfer, Nat. Phys. **5**, 352 (2009).
[255]T. Fujisawa, D. G. Austing, Y. Tokura, Y. Hirayama, and S. Tarucha, Nature **419**, 278 (2002).
[256]P. A. M. Dirac, Proc. R. Soc. A: Math., Phys. Eng. Sci. **114**, 243 (1927).
[257]E. Fermi, *Nuclear Physics* (University of Chicago Press, Chicago, 1974).
[258]M. N. Berberan-Santos, E. N. Bodunov, and B. Valeur, Chem. Phys. **315**, 171 (2005).
[259]E. E. Vdovin, Y. N. Khanin, A. V. Veretennikov, A. Levin, A. Patane, Y. V. Dubrovskii, L. Eaves, P. C. Main, M. Henini, and G. Hill, Nanotechnology **14**, 16 (2003).
[260]O. S. Wibbelhoff, A. Lorke, D. Reuter, and A. D. Wieck, Appl. Phys. Lett. **86**, 092104 (2005).
[261]A. Beckel, D. Zhou, B. Marquardt, D. Reuter, A. D. Wieck, M. Geller, and A. Lorke, Appl. Phys. Lett. **100**, 232110 (2012).
[262]C. W. J. Beenakker, Phys. Rev. B **44**, 1646 (1991).
[263]A. Kurzmann, B. Merkel, P. A. Labud, A. Ludwig, A. D. Wieck, A. Lorke, and M. Geller, Phys. Rev. Lett. **117**, 017401 (2016).
[264]S. Seidl, M. Kroner, P. Dalgarno, A. Högele, J. Smith, M. Ediger, B. Gerardot, J. Garcia, P. Petroff, K. Karrai, and R. Warburton, Phys. Rev. B **72**, 195339 (2005).
[265]T. Gallon and J. Matthew, Rev. Phys. Technol. **3**, 31 (1972).
[266]A. L. Efros and M. Rosen, Phys. Rev. Lett. **78**, 1110 (1997).
[267]V. I. Klimov, Science **290**, 314 (2000).
[268]A. W. Cohn, J. D. Rinehart, A. M. Schimpf, A. L. Weaver, and D. R. Gamelin, Nano Lett. **14**, 353 (2014).
[269]P. P. Jha and P. Guyot-Sionnest, ACS Nano **3**, 1011 (2009).
[270]B. Lounis, H. A. Bechtel, D. Gerion, P. Alivisatos, and W. E. Moerner, Chem. Phys. Lett. **329**, 399 (2000).
[271]J. M. Caruge, J. E. Halpert, V. Wood, V. Bulović, and M. G. Bawendi, Nat. Photonics **2**, 247 (2008).

[272]K.-S. Cho, E. K. Lee, W.-J. Joo, E. Jang, T.-H. Kim, S. J. Lee, S.-J. Kwon, J. Y. Han, B.-K. Kim, B. L. Choi, and J. M. Kim, Nat. Photonics **3**, 341 (2009).
[273]R. Vaxenburg, A. Rodina, A. Shabaev, E. Lifshitz, and A. L. Efros, Nano Lett. **15**, 2092 (2015).
[274]A. Kurzmann, A. Ludwig, A. D. Wieck, A. Lorke, and M. Geller, Nano Lett. **16**, 3367 (2016).
[275]J. M. Pietryga, K. K. Zhuravlev, M. Whitehead, V. I. Klimov, and R. D. Schaller, Phys. Rev. Lett. **101**, 217401 (2008).
[276]I. Robel, R. Gresback, U. Kortshagen, R. D. Schaller, and V. I. Klimov, Phys. Rev. Lett. **102**, 177404 (2009).
[277]W. K. Bae, Y.-S. Park, J. Lim, D. Lee, L. A. Padilha, H. McDaniel, I. Robel, C. Lee, J. M. Pietryga, and V. I. Klimov, Nat. Commun. **4**, 2661 (2013).
[278]P. Stegmann, B. Sothmann, A. Hucht, and J. König, Phys. Rev. B **92**, 155413 (2015).
[279]P. Stegmann and J. König, New J. Phys. **19**, 023018 (2017).